5-14-2021

Steady-State Transmembrane Water Exchange in Proliferating Cultures of *Saccharomyces cerevisiae*

Joseph O'Malley Armstrong
Portland State University

Steady-State Transmembrane Water Exchange in Proliferating Cultures of *Saccharomyces cerevisiae*

by

Joseph O'Malley Armstrong

A dissertation submitted in partial fulfillment of the
requirements for the degree of

Doctor of Philosophy
in
Chemistry

Dissertation Committee:
Mark Woods, Chair
Steve Reichow
Jason Podrabsky Sarah
Eppley

Portland State University
2021

ABSTRACT

Cellular water exchange is often considered in terms of a change in volume, where a net flux of water moves across the cell membrane due to a change in osmotic pressure. Osmotic pressure can cause a cell to shrink or swell, however, rapid water exchange persists across the membrane even when the volume of the cell is constant. Steady-state transmembrane water exchange describes the exchange of water across the cell membranes which results in no net change in cell volume. This exchange is astonishingly rapid; the entire pool of intracellular water of a *Saccharomyces cerevisiae* cell may exchange 2-5 times per second.

Steady-state water exchange can occur through two major routes. The first of these routes is through passive, osmotically driven processes. Passive water exchange occurs through simple diffusion through the membrane and facilitated diffusion through aquaporin water channels. The second route of steady-state water exchange is through energetically driven active processes. Water chaperones many ions and molecules as they cross the membrane in energetically associated processes. "Active water cycling" was coined by Springer and coworkers to describe the potential for these energetically driven processes to provide diagnostically useful information in an MRI scan. MRI measurements of water exchange has been demonstrated to relate to the activity of ATP driven ion pumps located in the membrane specifically, the Na^+/K^+ ATP*ase* in mammalian cells and the H^+ATP*ase* in yeast cells.

The dynamics of the relationships between growth, glucose metabolism and steady state water exchange regulation are still poorly understood. In this work, *Saccharomyces cerevisiae* was used as a model organism to study water exchange kinetics in contexts that are metabolically relevant as well as potentially diagnostically significant. Using a combination of batch cultures, continuous culture systems, and the *Yeast Knockout Library*, we explore the effects of cell growth, glucose metabolism and the expression of various membrane transporter genes on the rate constant for steady-state water exchange.

In addition, we also demonstrate how commercially available baking yeast can be used as a reliable to model a change in water exchange rate. Using this model, we show how water exchange rates can affect the observed relaxivity of two MRI contrast agents.

"When you're chewing on life's gristle,

Don't grumble, have a whistle,

And this'll help things turn out for the best…

Always look on the bright side of life."

Eric Idle

To my friends, family and to my love, Emily.

ACKNOWLEDGEMENTS

This work would not be possible without the support and encouragement from my colleagues within the Woods research group, both past and present. I must thank my colleagues in the chemistry stockroom, who never hesitated to help me track down a chemical or the odd bit of tubing for a culture chamber. I must also thank the caretakers of the NMR facility, Drs. Peyton and Duell, who were generous with their time and were never put off by my requests to put strange little tubes of yeast into the spectrometer at all hours of the night. Finally, I would like to thank my colleagues and professors of the Biology department, particularly Drs. Podrabsky and Thompson for entertaining all the silly questions a chemist must ask about cells.

TABLE OF CONTENTS

LIST OF TABLES

CHAPTER 2. STEADY-STATE TRANSMEMBRANE WATER EXCHANGE IN BATCH CULTURES OF *S. CEREVISIAE*

CHAPTER 3. THE EFFECTS OF TRANSMEMBRANE WATER EXCHANGE ON THE RELAXIVITY OF RESPONSIVE CONTRAST AGENTS

CHAPTER 4. STEADY-STATE TRANSMEMBRANE WATER EXCHANGE IN GLUCOSE LIMITED CHEMOSTAT CULTURES OF *S. CEREVISIAE*

LIST OF FIGURES

CHAPTER 1. INTRODUCTION

CHAPTER 2. STEADY-STATE TRANSMEMBRANE WATER EXCHANGE IN BATCH CULTURES OF *S. CEREVISIAE*

CHAPTER 3. THE EFFECTS OF TRANSMEMBRANE WATER EXCHANGE ON THE RELAXIVITY OF RESPONSIVE CONTRAST AGENTS

CHAPTER 4. STEADY-STATE TRANSMEMBRANE WATER EXCHANGE IN GLUCOSE LIMITED CHEMOSTAT CULTURES OF *S. CEREVISIAE*

LIST OF EQUATIONS

CHAPTER 1. INTRODUCTION

CHAPTER 2. STEADY-STATE TRANSMEMBRANE WATER EXCHANGE IN BATCH CULTURES OF *S. CEREVISIAE*

LIST OF ABBREVIATIONS

R_1	-	Longitudinal relaxation rate constant
R_2	-	Transverse relaxation rate constant
T_1	-	Longitudinal relaxation time constant ($1/R_1$)
T_2	-	Transverse relaxation time constant ($1/R_2$)
R_1^w	-	R_1 of pure water
R_{1i}	-	R_1 of intracellular water
R_{1e}	-	R_1 of extracellular water
[GBCA]		Gadolinium based contrast agent concentration
R_{1eo}	-	R_1 of extracellular water in the absence of GBCA
r_1	-	Relaxivity of a contrast agent
r_{mm}	-	Relaxivity of a macromolecules
a_i	-	Apparent intracellular water population
a_e	-	Apparent extracellular water population
p_i	-	Intracellular water mol fraction
k_{io}	-	Rate constant for water efflux
k_{oi}	-	Rate constant for water influx
2SX	-	Two-site exchange model
FXL	-	Fast Exchange Limit
FXR	-	Fast Exchange Regime
SXR	-	Slow Exchange Regime
[MM]	-	Concentration of macromolecules
r_{MM}	-	Relaxivity of intracellular macromolecules
T_d	-	Doubling time
D	-	Dilution rate
u	-	Culture growth rate

CHAPTER 1. INTRODUCTION

1.1 MRI: Discovery and Diagnostic Utility

Magnetic resonance (MR) can be used to make exquisite images of the human anatomy. Scans are used to monitor and to diagnose a wide number of conditions.[1] Today, MRI scanners are indispensable to any modern clinic. Each year, it is estimated that over 8% of the population in the United States receives a diagnostic scan.[2] Unlike other anatomical imaging techniques such as computed tomography (CT) or positron emission tomography (PET), MRI is largely non-invasive and does expose the patient ionizing radiation. MRI scans are tolerable for most patients with a few exceptions, most notably, among patients with an implanted medical device, and those with claustrophobia.[3,4] MRI is frequently used to provide images containing structural information such as the extent of damage to tendon, ligament, and muscle.

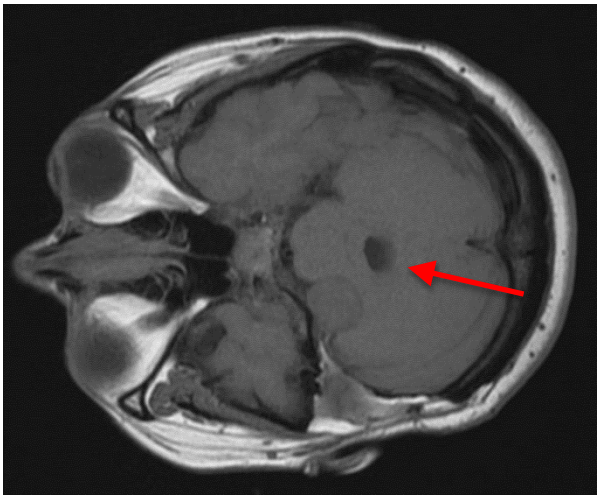

Figure 1.1 T_1 weighted axial image of an acoustic schwannoma. The red arrow is directed toward the cancerous lesion. Case courtesy of Assoc Prof Frank Gaillard, Radiopaedia.org.[5]

In addition to structural damage, MRI scans can also reveal other irregularities, as one would expect to find in hemorrhage, stroke, or lesions.[6] Two-dimensional images, such as the portion of a brain scan presented in Fig. 1.1, are a single slice of a more impressive and diagnostically useful three-dimensional image. These images can also have temporal resolution, allowing dynamic processes, such as the intricate valve movement of a beating heart, to be observed.[7] Diagnosticians can use software to reconstruct and navigate through the three dimensional images in order to understand the nature of a disease in extraordinary detail. The advent of novel imaging methods is an area of considerable ongoing research.[8–11]

The origins of MRI can be traced back to Felix Bloch and Edward Purcell for their work in the development of NMR spectroscopy.[12] Although NMR and MRI utilize the same fundamental principles, it was not until the late 1960's that imaging was seriously explored, and not until the 1980's that it became available in clinics. Like any technique developed over the course of multiple decades, there are far more contributors than awards given. MRI proves to be no exception, however the distribution of the Nobel Prize for the discovery of MRI is particularly controversial.

The first patent detailing an MRI scanner was filed by Raymond Damadian in 1968. The imaging methods and scanners used in the clinic today differ significantly from those detailed on the original patent. A drawing of the original MRI scanner by Damadian can be seen in Fig. 1.2. Although some of Damadian's predictions concerning MRI were correct, such as his prediction that cancerous tissue would be distinguishable from normal tissues on an image, it was not until the work of Paul Lauterber in the 1970's that images

could be reliably generated using MR.[13,14] Lauterber experimented with magnetic gradients using the shim coils of an NMR spectrometer to develop a technique known as frequency encoding, which is used to generate spatial resolution. Peter Mansfield is lauded as a co-founder of MRI.[15] Mansfield's development of the spin echo dramatically cut down on imaging time, and turned MRI from a curiosity in the lab into a useful diagnostic technique.[16]

Although the rules for the Nobel Prize committee stipulate that any award may be shared between up to three winners each year, the Nobel Prize in medicine in 2003 was only awarded to Lauterbur and Mansfield for the discovery of MRI.[17] Damadian felt like his contribution to the field was overlooked and issued a letter of protest to the Nobel Prize committee. Upon his petition, the committee ruled that, although Damadian was the first to patent the technique, the method he outlined in the patents was not feasible for producing images.[18] Damadian responded by taking out a full-page ad in the New York Times titled "*The Shameful Wrong That Must Be Righted* !"[19] Damadian's appeal to be included on the award was unsuccessful.

At its inception, MRI was referred to as NMRI, or "Nuclear Magnetic Resonance Imaging" because the technique originated from NMR spectroscopy.[14] The term "MRI" was not widely adopted until an editorial published in the American Journal of Roentgenology in 1984, suggested that nuclear be left off of the name in part because of the poor public perception of the word at the time. Although it was less technically descriptive, both the American Journal of Roentgenology and also Radiology edited

nuclear from their published manuscripts effectively forcing a rebrand for the technique as it became widely clinically available.[20]

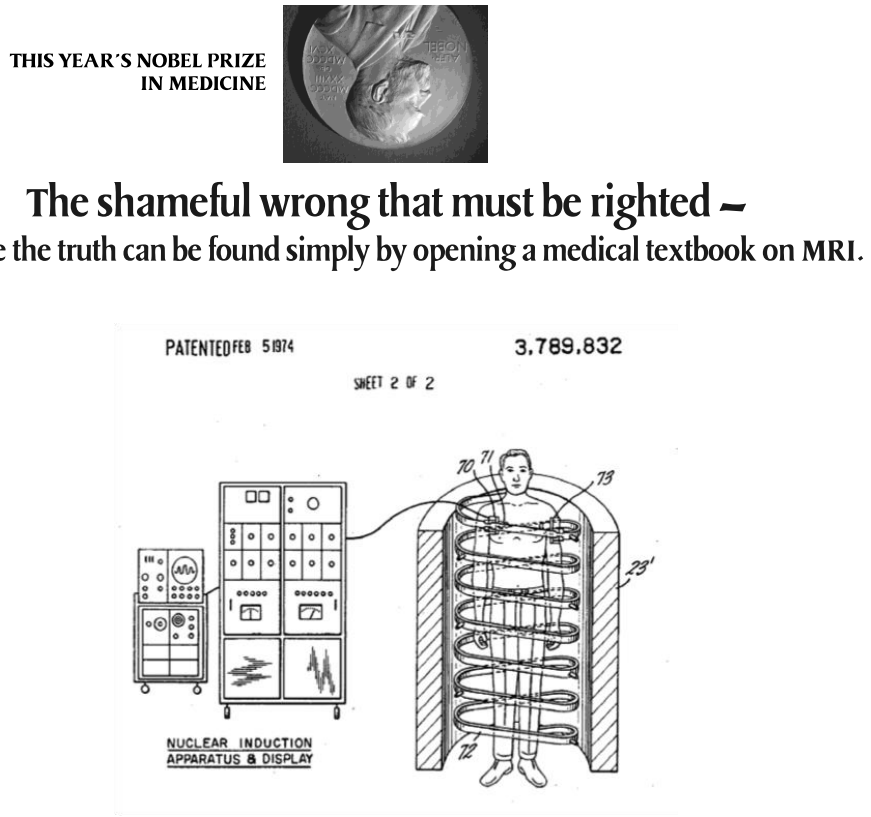

Figure 1.2 Raymond Damadian's appeal for the Nobel Prize appeared in the October 11th, 2003 edition of the *New York Times.* The full-page advertisement was headed by an inverted Nobel prize. Also included in the advertisement was an image of "NMRI" scanner from the original patent and a call for supporters to contact the Nobel committee on behalf of Damadian.

1.2 Basic Anatomy of an MRI

The technical design of a modern MRI scanner is a marvel of modern engineering and a complete description is beyond the scope of this document, however, it is useful to have a

simplified schematic of a scanner in order to understand the basic principles of image acquisition. An MRI scanner is composed of four principal components: the magnet, the gradient coils, the radiofrequency probe, and the spectrometer. Fig. 1.3 is a depiction of these core components. The main magnetic field of a typical MRI scanner (B_0) ranges from 1.5 – 7 T. The magnetic coils are insulated using a combination of liquid helium, liquid nitrogen and vacuum to maintain their superconductivity. Gradient coils are positioned geometrically around the bore of the main magnetic coil to allow manipulation of the field. The radiofrequency coils are used to excite and receive the signal from nuclei, while the spectrometer controls the excitation pulse and records the signal.

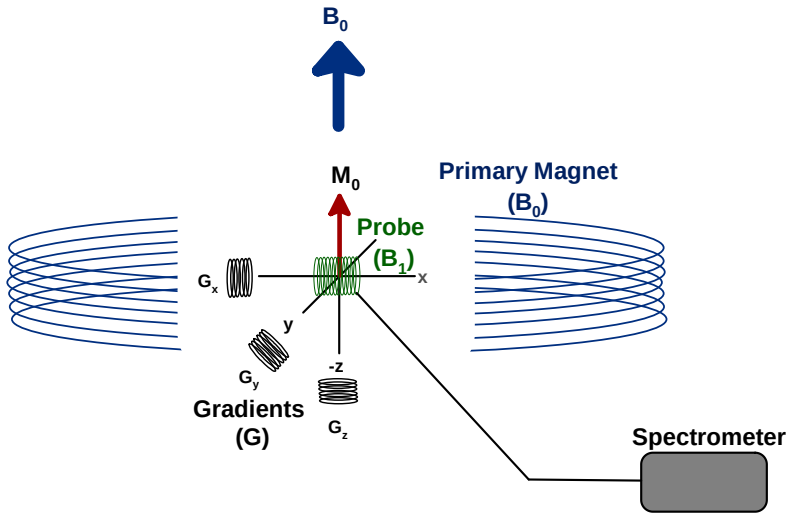

Figure 1.3 This schematic represents the core components of an MRI scanner. The bore of the scanner is denoted as the z-axis in line with B_0. In an MRI scanner the patient will typically rest on their back for the duration of the scan. There are also a number of additional gradients which are orientated in a myriad of other geometrical positions along with the ones listed in the figure. The loud banging that is associated with MRI, is due to these gradient coils.

1.3 The Excitation and Relaxation of Nuclear Spins

Generating images with MR is conducted through the measurement of a quantum mechanical phenomenon known as nuclear spin. When the nucleus of an atom contains an odd number of either (or both) protons or neutrons, the nucleus exhibits a small magnetic moment as a result of the conservation of angular momentum.[21] This small magnetic moment is often referred to as nuclear spin. Although there are a number of possible spin configurations, spin ½ nuclei are the primary source of signal in MR. The nuclei for atoms such as ^{1}H, ^{19}F, and ^{31}P are spin ½ (I = ½) in their most naturally occurring isotope.

When atoms with non-zero nuclear spin are placed into a magnetic field, their individual nuclear magnetic moments align with (N+) or against (N-) the magnetic field. [22]

$$\frac{N+}{N-} = e^{-\Delta E/kT} \qquad \Delta E = \gamma \hbar B_0 \tag{1.1}$$

The Boltzmann equation describes the energy distribution of spins between the two energy states. The variable k is Boltzmann's constant, γ is the gyromagnetic ratio of the nucleus, B_0 is the strength of the magnetic field and $\hbar$ is Plank's constant.[23] The energy gap (ΔE) between the low energy state (N+) and high energy state (N-) of a given nucleus increases with magnetic field strength and changes inversely to temperature. The sum of all the individual magnetic spins in a sample combine to make up the net magnetic vector (M_0). The magnitude of M_0 is proportional to the magnetic field strength, however, even the extraordinarily high fields of research magnets (~12T), only a few spins per million

contribute to the signal. Because of this lack of sensitivity, MRI scans primarily utilize the ^{1}H nucleus of water as the source of signal.

At equilibrium, the magnetic moments of the nuclei that make up M_0 are aligned with a slight bias toward the magnetic field of the scanner (B_0) and do not afford a measurable signal. M_0 must first be excited away from the equilibrium alignment using a radiofrequency pulse generated by the probe. The appropriate frequency of the applied pulse is a function of the nucleus as well as the strength of B_0. For ^{1}H nuclei, the excitation and precessional frequency (also known as the Larmor frequency) is 42.58 MHz/T.[24] When a radiofrequency pulse is applied, a secondary oscillating magnetic field, B_1, is established perpendicular to B_0. Although the strength of B_1 is many orders of magnitude less than B_0, M_0 is still excited away from equilibrium due the strong resonance interaction. A basic pulse experiment is shown in Fig. 1.4. Here, M_0 is excited away from its equilibrium alignment with B_0 to a desired angle. When the pulse stops, the excited magnetic vector, which is described as M(t), precesses around B_0 at the Larmor frequency. This precession of the magnetic vector induces a current in the receiver coil, which generates signal in an MRI. The precessional frequency is directly related to the local magnetic field experienced by the components that make up M(t).

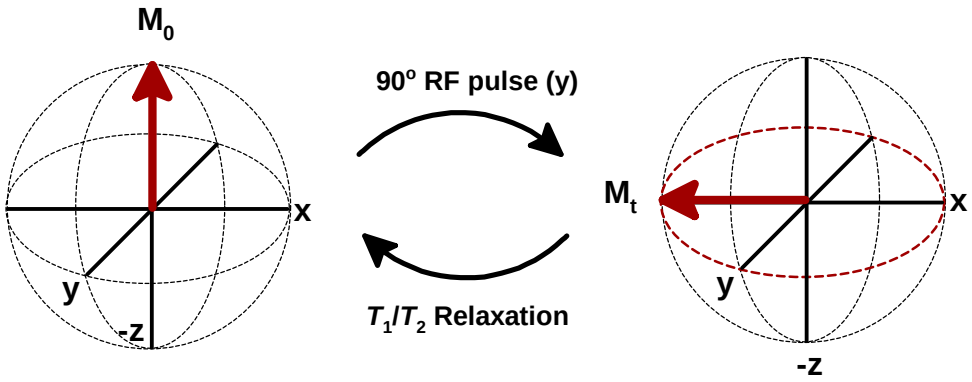

Figure 1.4 The net magnetic vector, M_0 (shown in red), at equilibrium can be excited by an oscillating magnetic field B_1. The excited vector, M(t), relaxes through T_1 and T_2 mechanisms to return to equilibrium.

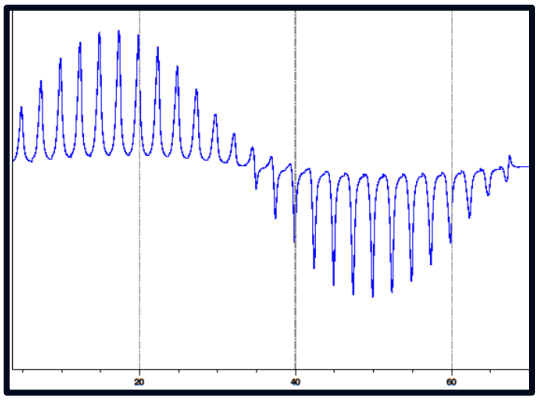

Figure 1.5 The effect of a RF pulse on the magnetic vector is best visualized by a nutation curve. The null points on the graph correspond to 180° and 360° while the maxima represent 90° and 270° (where the majority of the vector is in the x-y plane).

Once the radio frequency pulse is halted, the magnetization vector eventually returns to equilibrium. In 1946, Felix Bloch published a description of the precession and relaxation of an excited magnetic vector, M(t), over time in a magnetic field.[25] The description can be summarized as the following set of equations:

$$M(t) = (M_x(t), M_y(t), M_z(t))$$

$$B(t) = (B_x(t), B_y(t), B_0 + \Delta B_z(t))$$

$$\frac{\partial M_x(t)}{\partial t} = \gamma(M(t) \times B(t))_x - \frac{M_x(t)}{T_2}$$

$$\frac{\partial M_y(t)}{\partial t} = \gamma(M(t) \times B(t))_y - \frac{M_y(t)}{T_2}$$

$$\frac{\partial M_z(t)}{\partial t} = \gamma(M(t) \times B(t))_z - \frac{M_z(t) - M_0}{T_1} \quad \textbf{(1.2)}$$

The Bloch equations describe both precession and relaxation of the excited magnetic vector, M(t). M(t) and the magnetic field, B(t), are described in three dimensions. The gyromagnetic ratio of the excited nucleus, γ represents the field-dependent precessional rate of the vector. T_1 and T_2 are the longitudinal and transverse relaxation time constants, which describe how rapidly M(t) returns to the equilibrium alignment with the main magnetic field.

1.4 Modes of Relaxation

The excited magnetic vector, M(t), returns to the equilibrium environment through two modes characterized by the T_1 ($1/R_1$) and T_2 ($1/R_2$) relaxation time constants. Longitudinal relaxation, described by T_1, is an enthalpic process, which describes the return of magnetization to the equilibrium alignment oriented with B_0. Each consecutive passage of T_1 results in the return of 63% of the remaining magnetic vector to equilibrium. Temperature, solutes and magnetic field strength all affect the longitudinal

relaxation rate of water, however, at a given temperature, solute concentration, and magnetic field strength, the relaxation rate constant is an intrinsic value. The T_1 value for pure water at 600MHz and 25°C is around 3.2 seconds.

Transverse relaxation or T_2 relaxation ($1/R_2$) is an entropic process. T_2 relaxation describes the loss of coherence of the magnetization in the x-y plane.[26] Upon excitation, the individual vectors that make up the net magnetic vector are synchronous, however, M(t) quickly loses coherence due to slight differences in precessional frequency of the individual vectors. A more rapid loss of coherence has the effect of more uncertainty in the frequency of the individual components of the sample and broad lines on an NMR spectrum.

The contrast between tissues in an MR image is derived from the fundamental differences in relaxation between tissue types, which occurs as a result of differences in macromolecular content. Relaxation weighted imaging is a technique that takes advantage of the differences in relaxation between tissue types to generate an image. A clinical scan will typically acquire both T_1 and T_2 weighted images using a variety of pulse sequences to highlight anomalies that may be relevant. These weighted images are not quantifications of T_1 or T_2 relaxation constants. The quantification of relaxation rate constants requires specific pulse sequences. The longitudinal relaxation rate constant, R_1 ($1/T_1$), can be quantified using the inversion recovery pulse sequence. A schematic of the inversion recovery pulse sequence is shown in Fig. 1.6.

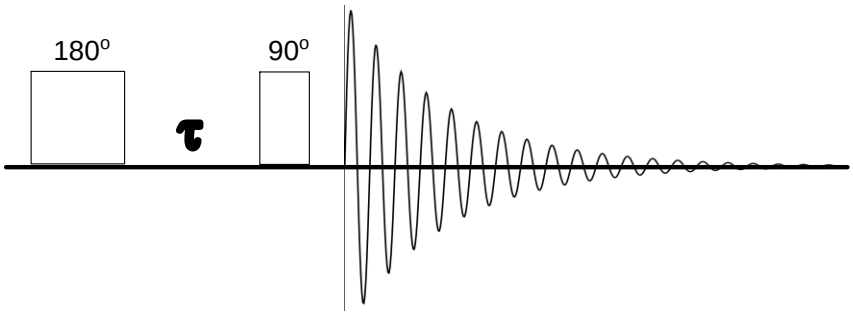

Figure 1.6 The inversion recovery pulse sequence is a two-pulse measurement used to quantify longitudinal relaxation. The 180° pulse inverts the nuclear magnetic vector. During the variable delay time, τ, a portion the magnetization vector recovers back to its equilibrium position. The 90° pulse flips the magnetization vector into the x-y plane where it precesses and induces a current in the receiver coil (denoted by the FID) where the magnitude of the vector is measured. This pulse sequence is repeated with a different values of τ until the complete recovery of the magnetized vector ($5 - 10 \times T_1$). After the collection of each FID, a delay equaling $5 - 10 \times T_1$ is used to ensure the magnetization vector has returned to equilibrium before the next measurement.

A rough estimate of T_2 can be made by inspecting the duration of the FID, however it can be precisely measured using a variation of a spin echo pulse sequence, such as the CPMG pulse sequence.[27] It is worth noting that the T_2 measured in any experiment is more precisely characterized as T_2^* because it is not only a measure of the inherent loss of coherence that would exist among the nuclear spins of the sample, but it is also subject to inhomogeneity of the magnetic field.[26,28]

1.5 MRI Contrast Agents and the Relaxometric "Shutter-Speed"

Gadolinium based contrast agents (GBCAs) are often administered to improve the diagnostic capability of an MRI scan. GBCAs have been clinically available since the late 1980's and nearly one third of all MRI scans today include the intravenous injection of a

GBCA.[29] Each dose contains between 0.5 – 1.0 grams of Gd^{3+} leading to around 50 tons of the rare earth to be administered each year [29,30] Fig. 1.7 shows a selection of a few clinically available contrast agents. Currently, clinically approved contrast agents vary only slightly in their effectiveness and are largely non-specific. The coordination number of Gd^{3+} is 9, while the ligands encasing the Gd^{3+} ion are typically octadentate. The remaining open coordination site allows for labile bonds with the surrounding water. Water molecules exchange rapidly on and off the chelate at rates greater than 10^{-7} s^{-1}.[30] GBCAs operate by affecting the T_1 relaxation rate constant of proximate water through a dipole-dipole interaction between the ^1H nuclei and the unpaired electrons of central Gd^{3+} ion. The Brownian motion of the complex generates a fluctuating magnetic field that catalyzes relaxation of the ^1H nuclei of proximate water molecules.[30]

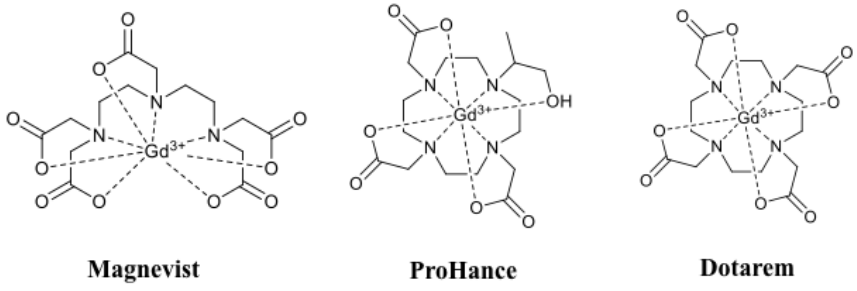

Figure 1.7 Three commonly available contrast agents. These agents represent both linear and macrocyclic structures and range of ionic charges.

The effectiveness, or relaxivity (r_1), of a GBCA is characterized by the effect of the agent on the relaxation rate of water R_1^{water} per mM GBCA and is given in Eqn. 1.3.

$$R_1 = r_1 [\text{GBCA}] + R_1^{water} \quad \textbf{(1.3)}$$

It is important to note that the presence of a GBCA is not detected directly. Instead, these agents are detected through their effect on the relaxation rate of the surrounding water. The indirect detection of the contrast agent carries significant consequences when attempting to quantify contrast agents in cell systems due to their exclusion to the extracellular space.[31] The extracellular restriction of contrast agents can create situations where intracellular water is distinct from extracellular water.

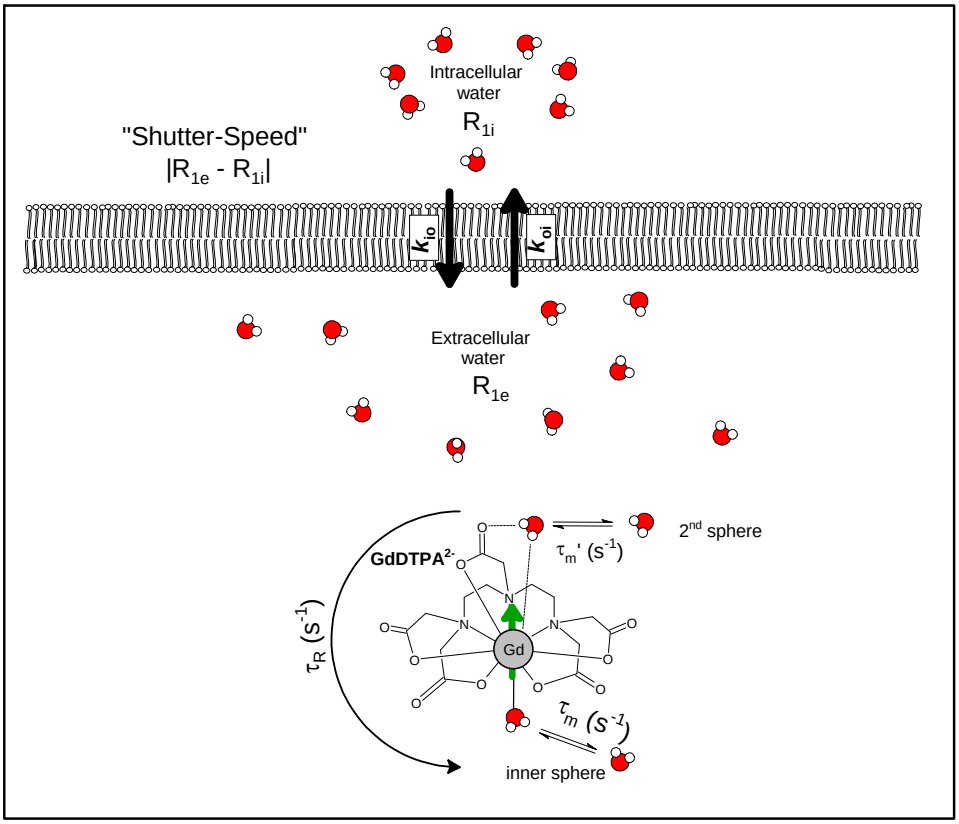

Figure 1.8 The intracellular and extracellular water pools can be distinguished relaxometrically after the addition of extracellular GBCA. The GBCA only affects intracellular water through the exchange of relaxed water molecules across the membrane. The relaxometric shutter speed is the absolute difference between the R_1 of the intracellular and extracellular water given by R_{1i} and R_{1e}, respectively.

If the R_1 values of intracellular and extracellular water are sufficiently different, the two water populations can be distinguished relaxometrically. The NMR shutter-speed is defined as the absolute value of the difference in the relaxation rate constants of a two-compartment system. The NMR shutter-speed is analogous to the shutter-speed of a camera. Just as increasing the shutter-speed of a camera allows a photographer to capture objects moving rapidly, increasing the NMR shutter-speed allows a relaxometrist to observe two compartments of water in rapid exchange. The shutter-speed of a system can be altered by increasing the GBCA concentration. The effect of the titration of $GdDTPA^{2-}$ into a cell pellet containing about ~50% intracellular water is shown in Fig. 1.9. As the concentration of $GdDTPA^{2-}$ is increased, the R_1 of extracellular water (R_{1e}) also increases. At concentrations of 1 mM $GdDTPA^{2-}$ the relaxation curve appears mono-exponential. As the concentration of contrast agent is increased, the two relaxing pools become more distinct.

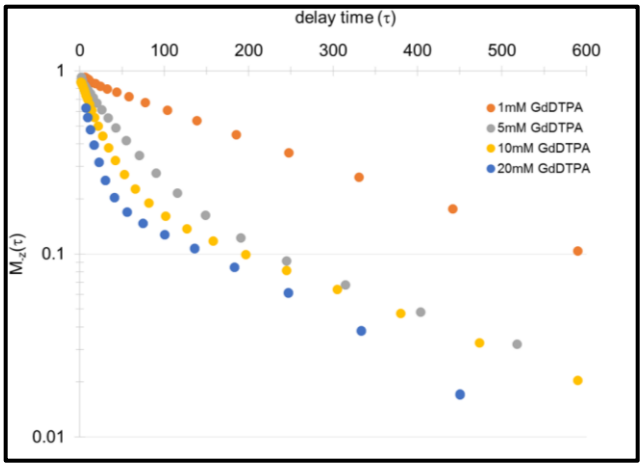

Figure 1.9 As the contrast agent concentration is increased, the absolute value of the difference between the relaxation rate constants, $|R_{1i} - R_{1e}|$ also increases. The SXR is defined when the biexponential break occurs around p_i (~0.5). In this experiment the SXR begins between 1 mM and 5mM GdDTPA. The 1mM GdDTPA measurement appears monoexponential and is either in the FXL or FXR.

The shutter-speed analogy is quite appropriate, however, some of the nomenclature that is used to describe the effect can be slightly misleading. Increasing the extracellular R_{1e} with a paramagnetic contrast agent can alter the shutter-speed from the "fast" to the "slow" regime. These terms are potentially misleading because changing shutter-speed regimes does not affect the rate of exchange between the two compartments, only the ability to observe them.

The shutter-speed regimes affect how relaxation is observed. The fast exchange limit shutter-speed condition is shown in Eqn. 1.4.

$$|R_{1e}\text{-}R_{1i}| << k_{ex} \qquad \textbf{(1.4)}$$

Where the transmembrane exchange rate constant, k_{ex}, in the cell system is much greater than the shutter-speed. In such conditions, the observed R_1, (R_1^{obs}) is defined by Eqn. 1.5.

$$R_1^{obs} = p_i R_{1i} + p_e R_{1e} \qquad \textbf{(1.5)}$$

Where p_i and p_e are the intracellular and extracellular water mol fractions and R_{1i} and R_{1e} are the intracellular and extracellular relaxation rate constants, respectively. Compartmentalized systems in the FXL behave like a diffuse, homogeneous solution. R_1^{obs} is therefore, the mass balanced sum of the relaxation rate constants of the two compartments.

The fast exchange regime (FXR) occurs when the relaxation rate constant of a sample is mono-exponential, but the sample does not behave like a well-mixed solution. The FXR

often occurs when the concentration of contrast agent is low (typically less than 1 mM). In the FXR, both compartmentalization and exchange affect the observed relaxation of a system even in conditions where mono-exponential relaxation is observed. The effect of a compartmentalized system in the FXR on R_1^{obs} can be described by Eqn. 1.6. The observed relaxation rate constant of the intracellular compartment (R_{1i}^{obs}) can be defined by the intrinsic relaxation rate constants (R_{1i}) and exchange between the two compartments.

$$R_1^{obs} = \frac{1}{2}\left[R_{1i} + R_{1e} + k_{io} + k_{oi}\right] - \frac{1}{2}\{[(R_{1i} - R_{1e}) + (k_{io} - k_{oi})]^2 + 4k_{io}k_{oi}\}^{1/2}$$

(1.6)

Where the intracellular and extracellular relaxation rate constants (R_{1i} and R_{1e}) impact R_1^{obs} as a function of the transmembrane efflux (k_{io}) and transmembrane influx (k_{oi}) unidirectional rate constants. The intrinsic intracellular relaxation rate constant is given by R_{1i} and the intrinsic extracellular relaxation rate constant is given by R_{1e}. The rate constant for steady-state water efflux, k_{io}, is an intrinsic cellular property that describes the unidirectional efflux of water.

The slow exchange regime (SXR) occurs when the values of R_{1i} and R_{1e} are distinct enough that the relaxation rate constant of a sample appears biexponential. This typically occurs at an extracellular GBCA concentration of 5-10mM. When a sample is in the SXR there is a break in the relaxation data approximately equal to the intracellular water mol fraction, p_i. When a sample is in the SXR, the relaxation data can be fit to a model

known as the two-site exchange (2SX) system of equations to quantify the exchange between the two water pools.[32,33]

To calculate the rate of transmembrane water efflux, k_{io}, the relaxation data is first fit to the biexponential equation shown in Eqn. 1.7.

$$M_z(t) = M_z(\infty)\left[1 - 2\left[a_i e^{-tR_{1i}^{obs}} + a_e e^{-tR_{1e}^{obs}}\right]\right] \quad \textbf{(1.7)}$$

Where R_{1i}^{obs} and R_{1e}^{obs} are the observed intracellular and extracellular relaxation rate constants, respectively. These observed values differ from their intrinsic values due to exchange between the two compartments. These observed values can be further reduced into the parameters found in Eqns. 1.8-1.10, which make up the two-site exchange model (2SX). The rate constant for steady state transmembrane water efflux, k_{io}, can be measured using the 2SX model. The observed R_1 of the intracellular component is then broken down into the components of Eqn. 1.8, and the observed R_1 of the extracellular component is broken down into the components of Eqn. 1.9.

$$R_{1i}{}^{obs} = 0.5\left[R_{1i} + r[GBCA] + R_{1eo} + k_{io} + \frac{k_{io}p_i}{(1-p_i)}\right] - 0.5\left\{\left[R_{1i} + r[GBCA] + R_{1eo} + k_{io} + \frac{k_{io}p_i}{(1-p_i)}\right]^2 + \frac{{k_{io}}^2 4p_i}{(1-p_i)}\right\}^{0.5} \quad \textbf{(1.8)}$$

$$R_{1e}{}^{obs} = 0.5\left[R_{1i} + r[GBCA] + R_{1eo} + k_{io} + \frac{k_{io}p_i}{(1-p_i)}\right] + 0.5\left\{\left[R_{1i} + r[GBCA] + R_{1eo} + k_{io} + \frac{k_{io}p_i}{(1-p_i)}\right]^2 + \frac{{k_{io}}^2 4p_i}{(1-p_i)}\right\}^{0.5} \quad \textbf{(1.9)}$$

The term [GBCA] reflects the extracellular concentration of contrast agent and p_i reflects the intracellular water mol fraction. The term R_{1i} reflects the intrinsic rate constant for

intracellular relaxation and is often set to a fixed value. R_{1eo} represents the relaxation rate constant of the extracellular water in the absence of GBCA. The apparent population coefficient for the extracellular and intracellular cellular compartment, a_e and a_i respectively, can also be also defined by the intrinsic the intracellular relaxation rate constant, R_{1i}, the rate constant for water efflux, (k_{io}) (Eqn. 1.10).

$$\frac{a_e}{a_e - a_i} = \left[\frac{(R_{1i} - r[GBCA] - R_{1eo})(1-2p_i) + k_{io} + \frac{k_{io}p_i}{(1-p_i)}}{\left\{ \left[R_{1i} - r[GBCA] - R_{1eo} + k_{io} + \frac{k_{io}p_i}{(1-p_i)} \right]^2 + \frac{4p_i}{k_{io}{}^2(1-p_i)} \right\}^{0.5}} \right] \quad \textbf{(1.10)}$$

Although relaxation-based methods present a convenient method of measuring steady-state water exchange, there are other methods, such as diffusion weighted imaging that are also capable of accurate measurements membrane exchange.

1.6 Mechanisms of Membrane Water Exchange

The first measurements of steady state water exchange were taken just after the second world war using isotopically labelled water to quantify exchange in cells.[34] The transport of water across the cell membrane was assumed to occur through simple passive diffusion up until the late 1950's, when the work of Paganelli and Solomon revealed that the exchange of water across erythrocyte membranes occurred at rates that exceeded what would be possible if the mechanism was strictly limited to passive diffusion.[34]

In the 1990's, Peter Agre and coworkers discovered the aquaporin family of water channels, which are integral to the rapid transport of water observed in erythrocytes.[35,36] Since their initial discovery, aquaporins or aquaporin like channels have been identified

in many organisms from bacteria to yeast and humans alike.[37] Although aquaporin provide a route for water exchange, it became clear early on that the aquaporin are not the only mechanism of water transport. In fact, individuals with Coulton-null syndrome who lack the major aquaporin gene in humans *aqp1* are able to function normally except in the case of extreme dehydration.[38]

In addition to the facilitated diffusion of water through the aquaporin membrane channels, water is also coupled to ion and nutrient transport.[39] Coupled transport provides a mechanism by which the cell can move water in the absence, or in some cases, against an osmotic gradient.[38] One instance of the uphill transport of water occurs in the small intestine just after a meal. In this scenario, the osmolarity of the luminal solution increases due to the presence of glucose and other nutrients.[38] Water is cotransported together with Na^+ and glucose through the sodium glucose cotransporter family of membrane channels (SGLT). It is estimated that over 200 molecules of water chaperone for each molecule of glucose taken up.[40] These water molecules are transported uphill against the gradient because they are involved in the energetically favorable transport of Na^+.

Primary active transporters are central to membrane transport because they utilize ATP to form gradients across membranes. These gradients then serve to drive other membrane transport processes. Secondary transporters utilize the gradient produced by the primary active transporters to couple the transfer of substrates across the membrane. Three methods of secondary transport, known as antiport, symport and uniport are shown in

Fig. 1.10. There are many secondary transport processes that have been shown to also transport water.[38–40]

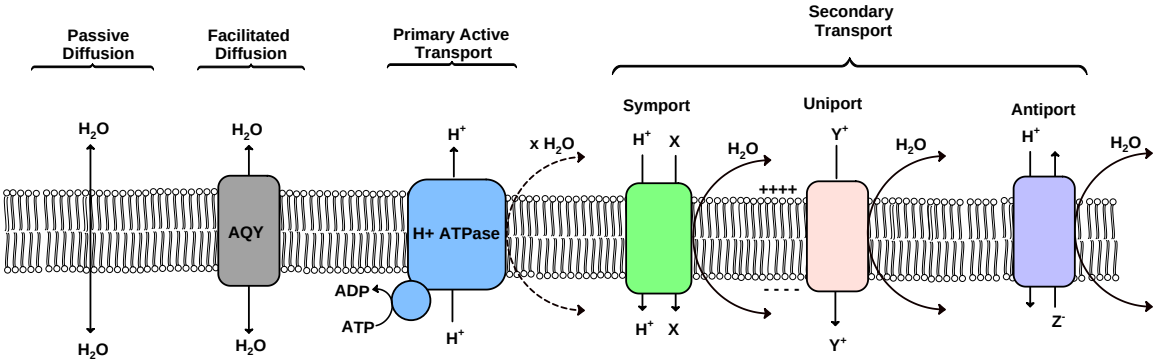

Figure 1.10 Exchange across the membrane can occur through a number of different processes. Passive diffusion is the diffusion of a molecule through the phospholipid membrane without the aid of a channel. Facilitated diffusion is a pore in the membrane that allows a molecule to pass through the membrane with little resistance. Primary active transport utilizes ATP to transport material across the membrane. Secondary transport utilizes the gradient produced by primary active transport to facilitate the uptake or efflux of a substrate. Many secondary transport processes have been shown to utilize water to facilitate the passage of substrates across the membrane.[38–41]

1.7 The "Active Water Cycling" Hypothesis

The "active water cycling" (AWC) theory posits that k_{io} is made up of both passive, $k_{io}(p)$ and active components, $k_{io}(a)$.

$$k_{io} = k_{io}(a) + k_{io}(p) \quad \textbf{(1.11)}$$

The passive component of k_{io} is a function of the passive permeability of the cell membrane as well as the cellular morphology. Passive k_{io}, is defined by Eqn. 1.12 and

incorporates the surface area (SA) to volume (V) ratio and the passive permeability of water through the membrane (P_w). A drastic change in membrane composition can alter P_w; however, passive k_{io} is also affected by changes to cell size.[42]

$$k_{io}(p) = \frac{SA}{V} P_w \qquad \textbf{(1.12)}$$

The AWC theory also posits that active k_{io} can serve as a proxy for measuring ATP*ase* activity *in vivo*. There are a number of measurements in the literature that support the importance of ATP driven pumps to k_{io}. The inhibition of the Na^+/K^+ ATP*ase* pump with ouabain has been shown to reduce k_{io} in perfused mammalian heart tissue.[43] The reduction in k_{io} observed in heart tissue upon exposure to ouabain is not a result of a change in cell volume and can therefore cannot be easily explained by a change passive permeability. Similarly, k_{io} has been shown to decrease in yeast cells in which the ATP driven proton pump known as the H^+ATP*ase* (coded by the gene *pma1*) has been inhibited with ebselen.[44] These studies also reported that changes to volume that occurs upon inhibition with ebselen cannot adequately explain the change in k_{io} observed. The authors of the AWC theory do not suggest that the water is exclusively exchanged through the ATP*ase* pump, but also through processes that may utilize the gradient produced by the pump. Eqn. 1.13 represents ATP driven water transport which is hypothesized to drive the active component of water exchange k_{io}.

$$k_{io}(a) = \frac{x}{[H_2O_i]} MR_{ATPase} \qquad \textbf{(1.13)}$$

The stoichiometric mole ratio of water, *x*, describes the amount of water transferred as a result of the activity of ATP driven pumps and [H_2O_i] represents the intracellular water concentration.

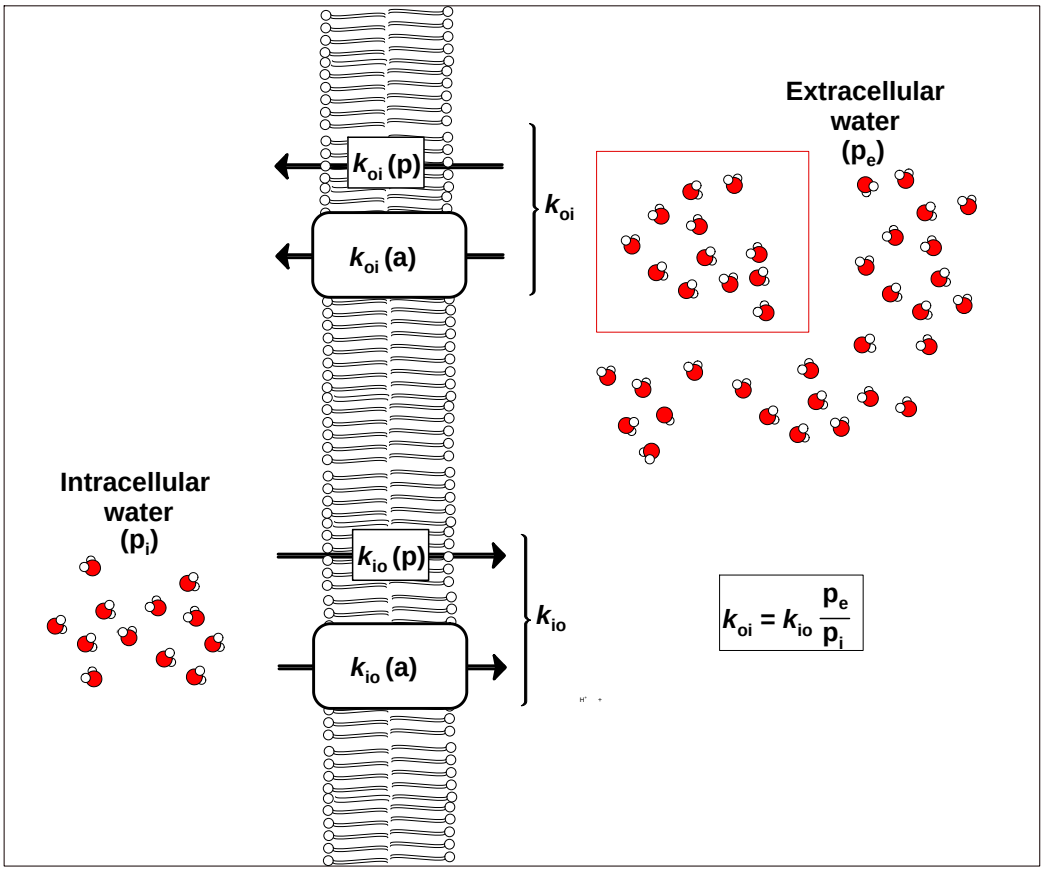

Figure 1.11 Steady-state transmembrane water exchange can be described by the rate constants k_{io} (in → out: efflux) and k_{oi} (out → in: influx). The rate constant for water efflux, k_{io} is made up of both active (a) and passive processes (p).The two rate constants, k_{io} and k_{oi} are related through the population fractions of water in the extracellular environment, p_e, and in the intracellular environment, p_i. When p_i and p_e are equal, k_{oi} equals k_{io}.

1.8 Measuring Water Exchange *In Vivo*

The measurement of k_{io} has be conducted *in vivo* using MRI and holds considerable promise as a potential biomarker for diagnostic imaging. In a series of imaging studies, k_{io} has been shown to correlate with tumor metastatic potential and with head and neck cancer mortality.[45] k_{io} was also found to vary not only between normal and pathological tissue, but also across the tissue associated with a single pathology. A comparison of k_{io} to other imaging modalities, such as positron emission tomography (PET) with the radio tracer ^{18}Fluoro – deoxyglucose (^{18}FDG) can be seen in Fig 1.12.

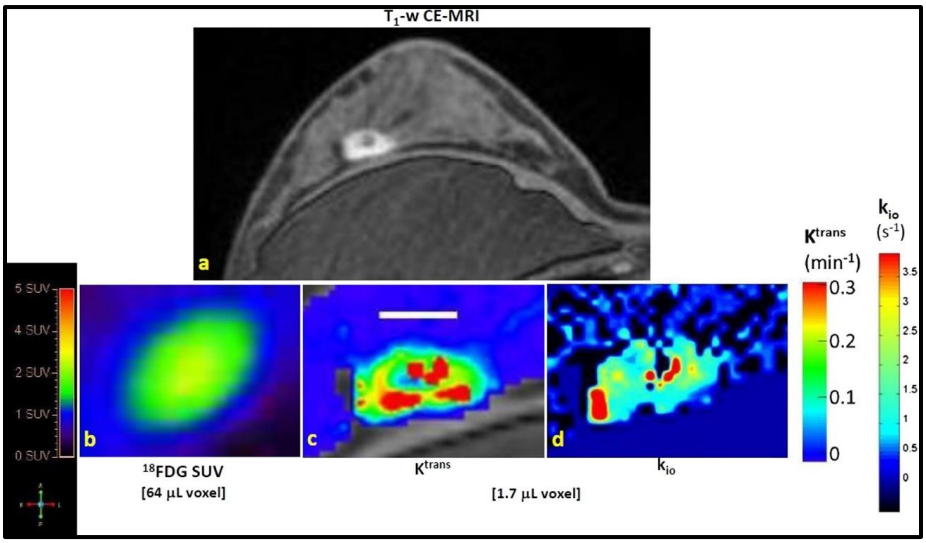

Figure 1.12 T1 weighted contrast enhanced MRI shows the delineation of a breast cancer tumor. FDG SUV indicates the standard uptake value of the radiotracer ^{18}Fluoro – deoxyglucose. K^{trans} indicates the extravasation rate of the contrast agent. k_{io} is rate constant for water efflux. [46]

In this comparison, the standard uptake value (SUV) of ^{18}FDG is compared with two MRI parameters, K^{trans}, which is the contrast agent extravasation rate and k_{io}. K^{trans} is a

measure of the leakiness of the vasculature in a region of interest. It is clear from this comparison that MRI has an advantage over PET in terms of resolution. The parameter k_{io} is alluring because unlike K^{trans}, it is a rate constant, not a rate, and is reflective of an intrinsic cellular property, as opposed to K^{trans} which is reflective of a tissue macrostructure.

1.9 *Saccharomyces cerevisiae* as a model system for metabolism and exchange

In this work, *Saccharomyces cerevisiae* is used as a model system to probe exchange. *S. cerevisiae* is a single celled, eukaryotic organism, which characteristically divides by budding. Although there are countless differences between the physiology of humans and yeasts, *S. cerevisiae* provide a suitable platform to explore the fundamental biological implications of steady-state transmembrane water exchange for a number of reasons. 2SX modeling operates under the assumption that the extracellular and intracellular environments are well mixed. 2SX modelling also requires a known concentration of extracellular contrast agent for accurate measurement. In cell suspensions, the control of the extracellular contrast agent concentration is easily managed, which greatly simplifies the relaxometric determinations of k_{io}. *S. cerevisiae* are also quite robust and can readily withstand gentle centrifugation to create pellets to be placed in the NMR. Pelletized samples provide substantial intracellular water populations, which makes the measurement of k_{io} more practical. Pelleted cell samples can serve to represent a one voxel “images” of water exchange.

Alongside the many industrial applications, *S. cerevisiae* is widely used as model organism due to its ease in preservation and its rapid growth. In 1996, the strain SC288 was the first organism to have its genome fully sequenced.[47] This effort sparked the era of modern genomics and introduced many new technologies which further expanded the budding yeast's utility as a model organism. The ease at which the yeast genome can be manipulated has prompted the creation of libraries containing thousands of genetically modified strains all readily available for purchase. [48] Fig. 1.13 depicts the most common method of genome manipulation in yeast.

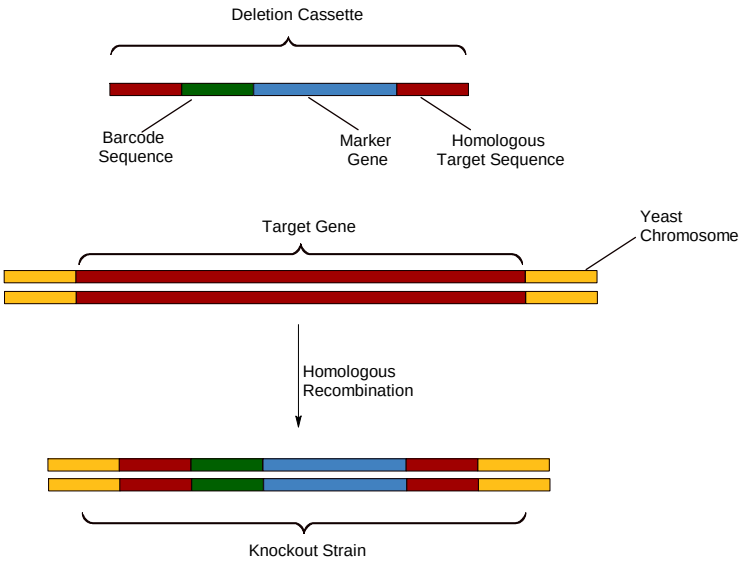

Figure 1.13 Non-essential genes can be knocked out of yeast though the use of a deletion cassette carried into the cell by a plasmid vector. The gene deletion project helped to create a knockout library through the systematic deletion of each non-essential gene in the yeast genome.

1.10 The Crabtree Effect

S. cerevisiae can be cultivated in a number of ways which gives the experimenter a great deal of flexibility in designing experiments. The metabolism of yeasts is a particularly intriguing and a potentially diagnostically relevant starting point for probing steady-state exchange. The fermentation of sugars into ethanol is one of the most well-known (and perhaps well-appreciated) traits of yeast Saccharomyces *cerevisiae*. *S. cerevisiae* cells, like cancer cells, are observed to undergo fermentation even in the presence of adequate oxygen. The Crabtree effect, first described by Herbert Grace Crabtree in 1929, is the propensity for yeast to undergo fermentation even in well oxygenated conditions.[49,50] An estimated 18 molecules of ATP are generated through the complete oxidation of glucose during cellular respiration, while only 2 molecules of ATP are estimated to be produced during aerobic fermentation.[51] Although the yield of ATP generated per molecule of glucose is approximately 9 times greater during cellular respiration, the rate of ATP generation during aerobic fermentation occurs at a faster rate. The Crabtree effect can be described as a tradeoff between rate of ATP production and yield of ATP per molecule of glucose.

Trading off the yield of ATP per molecule glucose to increase the rate of ATP production gives an evolutionary advantage when competing for shared resources in nature. In this respect, the Crabtree effect may be analogous to the Warburg effect in cancerous cells; however, in cancer cells lactic acid is the major fermentative product.[52,53] This production of ethanol by yeast is thought to have arisen because of a Make-Accumulate-Consume strategy whereby Crabtree positive yeast evolved to quickly ferment sugars around them,

and then consumed the ethanol later, if necessary.[54] *S. cerevisiae* provide a platform to understand the energetics of metabolism and how it relates to k_{io}.

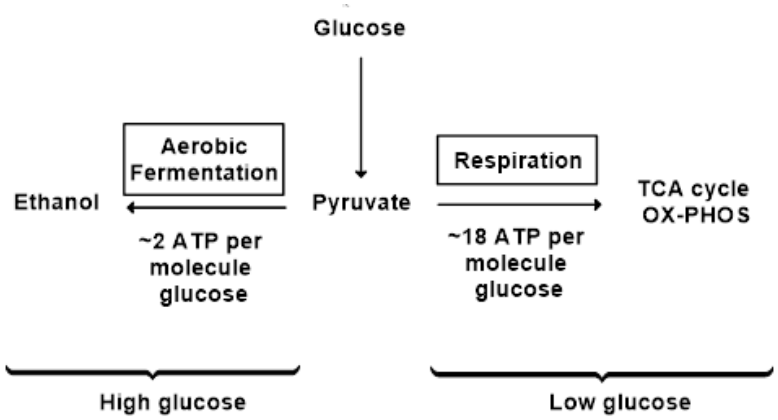

Figure 1.14 The Crabtree Effect in *Saccharomyces cerevisiae* is the tendency to ferment ethanol even in well oxygenated conditions. The extracellular glucose concentration is the determining factor for the metabolic pathway utilized by yeast.

1.11 Thesis Outline

Understanding water exchange in the context of cellular energetics is key to understanding the diagnostic relevance of a change in k_{io}. There are three fundamental questions that we seek to answer in order to further our understanding of k_{io} namely:

Can proliferating cells be differentiated from quiescent cells by their water exchange rates?

Growing cells differ from quiescent cells in a number of respects and it is of great interest to understand how these changes may affect k_{io}. As unregulated growth is one of the hallmarks of cancerous cells, understanding how water exchange differs in growing

versus quiescent cells is of significant interest. The AWC hypothesis predicts that growing cells will undergo more rapid exchange through active k_{io} due to the increased nutrients taken up and expelled in comparison to quiescence. In Chapter 2, we explore how k_{io} changes across a growth curve of batch cultivated yeast.

How can glucose metabolism affect k_{io}?

Although metabolic influences on k_{io} have been proposed, the relationship between steady-state water exchange and fundamental cellular processes such as glucose metabolism is poorly understood. In Chapter 4, we examine how the various pathways of glucose metabolism can alter k_{io} using glucose limited chemostat cultures of yeast.

Can changes to k_{io} affect the observed relaxivity of contrast agents?

Along with answering biologically significant questions, we also look at how yeast cells can be used as a model system to probe the effects of compartmentalization on the quantification of GBCAs. In Chapter 3, we explore how changes to k_{io} can affect the quantification of MRI contrast agents.

1.12 References

1. Grover, V. P. B. *et al.* Magnetic Resonance Imaging: Principles and Techniques: Lessons for Clinicians. *J. Clin. Exp. Hepatol.* **5**, 246–255 (2015).
2. Health care use - Magnetic resonance imaging (MRI) exams - OECD Data. *theOECD* http://data.oecd.org/healthcare/magnetic-resonance-imaging-mri-exams.htm.
3. Magnetic Resonance Imaging (MRI). https://www.nibib.nih.gov/science-education/science-topics/magnetic-resonance-imaging-mri.
4. Ponce de Leon, M. Safety Considerations in Magnetic Resonance Imaging of Patients With Implanted Medical Devices. *Contin. Lifelong Learn. Neurol.* **22**, 1691 (2016).
5. Frank Gaillard | profile | Radiopaedia.org. *Radiopaedia* https://radiopaedia.org/users/frank?lang=us.
6. Oliveira, I. S., Hedgire, S. S., Li, W., Ganguli, S. & Prabhakar, A. M. Blood pool contrast agents for venous magnetic resonance imaging. *Cardiovasc. Diagn. Ther.* **6**, 508–518 (2016).
7. Gatehouse, P. D. *et al.* Applications of phase-contrast flow and velocity imaging in cardiovascular MRI. *Eur. Radiol.* **15**, 2172–2184 (2005).
8. Hyperpolarized 13C MRI: State of the Art and Future Directions | Radiology. https://pubs.rsna.org/doi/full/10.1148/radiol.2019182391.
9. Stabile, A. *et al.* Multiparametric MRI for prostate cancer diagnosis: current status and future directions. *Nat. Rev. Urol.* **17**, 41–61 (2020).
10. Advances in clinical MRI technology | Science Translational Medicine. https://stm.sciencemag.org/content/11/523/eaba2591?rss=1.
11. Grist, T. M. The Next Chapter in MRI: Back to the Future? *Radiology* **293**, 394–395 (2019).
12. The Nobel Prize in Physics 1952. *NobelPrize.org* https://www.nobelprize.org/prizes/physics/1952/summary/.
13. Damadian, R. Tumor detection by nuclear magnetic resonance. *Science* **171**, 1151–1153 (1971).
14. Damadian, R. Apparatus and method for detecting cancer in tissue. (1974).
15. Lauterbur, P. C. Image Formation by Induced Local Interactions: Examples Employing Nuclear Magnetic Resonance. *Nature* **242**, 190–191 (1973).
16. Mansfield, P. Multi-planar image formation using NMR spin echoes. *J. Phys. C Solid State Phys.* **10**, L55–L58 (1977).

17. The Nobel Prize in Physiology or Medicine 2003. *NobelPrize.org* https://www.nobelprize.org/prizes/medicine/2003/press-release/.

18. Pearson, H. Physician launches public protest over medical Nobel. *Nature* **425**, 648–648 (2003).

19. Wade, N. Doctor Disputes Winners of Nobel in Medicine (Published 2003). *The New York Times* (2003).

20. Pohost, G. M., Elgavish, G. A. & Evanochko, W. T. Nuclear magnetic resonance imaging: With or without nuclear? *J. Am. Coll. Cardiol.* **7**, 709–710 (1986).

21. Fuller, G. H. Nuclear Spins and Moments. *J. Phys. Chem. Ref. Data* **5**, 835–1092 (1976).

22. Rowlinson *, J. S. The Maxwell–Boltzmann distribution. *Mol. Phys.* **103**, 2821–2828 (2005).

23. von Schulthess, G. K. The Physical Basis of Magnetic Resonance Imaging. in *Morphology and Function in MRI: Cardiovascular and Renal Systems* (ed. von Schulthess, G. K.) 3–32 (Springer, 1989). doi:10.1007/978-3-642-73516-5_2.

24. Larmor Frequency - an overview | ScienceDirect Topics. https://www.sciencedirect.com/topics/computer-science/larmor-frequency.

25. Bloch, F. Nuclear Induction. *Phys. Rev.* **70**, 460–474 (1946).

26. Paley, M. MRI of tissues with short T2s and T2*s. G. M. Bydder, G. D. Fullerton and I. R. Young. *NMR Biomed.* **26**, 1336–1337 (2013).

27. Carr, H. Y. & Purcell, E. M. Effects of Diffusion on Free Precession in Nuclear Magnetic Resonance Experiments. *Phys. Rev.* **94**, 630–638 (1954).

28. Chavhan, G. B., Babyn, P. S., Thomas, B., Shroff, M. M. & Haacke, E. M. Principles, Techniques, and Applications of T2*-based MR Imaging and Its Special Applications. *RadioGraphics* **29**, 1433–1449 (2009).

29. Lohrke, J. *et al.* 25 Years of Contrast-Enhanced MRI: Developments, Current Challenges and Future Perspectives. *Adv. Ther.* **33**, 1–28 (2016).

30. Wahsner, J., Gale, E. M., Rodríguez-Rodríguez, A. & Caravan, P. Chemistry of MRI Contrast Agents: Current Challenges and New Frontiers. *Chem. Rev.* **119**, 957–1057 (2019).

31. The effects of equilibrium transcytolemmal water exchange on the determination of contrast reagent concentration in vivo - Springer - 2002 - Magnetic Resonance in Medicine - Wiley Online Library. https://onlinelibrary.wiley.com/doi/full/10.1002/mrm.10099.

32. Lee, J.-H. & Springer, C. S. Effects of equilibrium exchange on diffusion-weighted NMR signals: the diffusigraphic ‘shutter-speed’. *Magn. Reson. Med.* **49**, 450–458 (2003).

33. Li, X., Mangia, S., Lee, J., Bai, R. & Springer, C. S. NMR shutter-speed elucidates apparent population inversion of 1H2O signals due to active transmembrane water cycling. *Magn. Reson. Med.* **82**, 411–424 (2019).

34. Paganelli, C. V. & Solomon, A. K. THE RATE OF EXCHANGE OF TRITIATED WATER ACROSS THE HUMAN RED CELL MEMBRANE. *J. Gen. Physiol.* **41**, 259–277 (1957).

35. Preston, G. M., Carroll, T. P., Guggino, W. B. & Agre, P. Appearance of water channels in Xenopus oocytes expressing red cell CHIP28 protein. *Science* **256**, 385–387 (1992).

36. Benga, G. *et al.* Water permeability in human erythrocytes: identification of membrane proteins involved in water transport. *Eur. J. Cell Biol.* **41**, 252–262 (1986).

37. Brown, D. The Discovery of Water Channels (Aquaporins). *Ann. Nutr. Metab.* **70**, 37–42 (2017).

38. Zeuthen, T. Water-transporting proteins. *J. Membr. Biol.* **234**, 57–73 (2010).

39. Zeuthen, T. & MacAulay, N. Cotransport of water by Na+–K+–2Cl− cotransporters expressed in Xenopus oocytes: NKCC1 versus NKCC2. *J. Physiol.* **590**, 1139–1154 (2012).

40. Zeuthen, T., Meinild, A.-K., Loo, D. D. F., Wright, E. M. & Klaerke, D. A. Isotonic transport by the Na+-glucose cotransporter SGLT1 from humans and rabbit. *J. Physiol.* **531**, 631–644 (2001).

41. Zeuthen, T., Gorraitz, E., Her, K., Wright, E. M. & Loo, D. D. F. Structural and functional significance of water permeation through cotransporters. *Proc. Natl. Acad. Sci.* **113**, E6887–E6894 (2016).

42. Mathai, J. C., Tristram-Nagle, S., Nagle, J. F. & Zeidel, M. L. Structural Determinants of Water Permeability through the Lipid Membrane. *J. Gen. Physiol.* **131**, 69–76 (2008).

43. Coelho-Filho, O. R. *et al.* Role of Transcytolemmal Water-Exchange in Magnetic Resonance Measurements of Diffuse Myocardial Fibrosis in Hypertensive Heart Disease. *Circ. Cardiovasc. Imaging* **6**, 134–141 (2013).

44. Zhang, Y., Poirier-Quinot, M., Springer, C. S. & Balschi, J. A. Active Trans-Plasma Membrane Water Cycling in Yeast Is Revealed by NMR. *Biophys. J.* **101**, 2833–2842 (2011).

45. Springer, C. S. Using $^{1}H_2O$ MR to measure and map sodium pump activity in vivo. *J. Magn. Reson.* **291**, 110–126 (2018).

46. Springer, C. S. *et al.* Intratumor mapping of intracellular water lifetime: metabolic images of breast cancer? *Nmr Biomed.* **27**, 760–773 (2014).

47. Goffeau, A. *et al.* Life with 6000 genes. *Science* **274**, 546, 563–567 (1996).

48. Giaever, G. & Nislow, C. The Yeast Deletion Collection: A Decade of Functional Genomics. *Genetics* **197**, 451–465 (2014).

49. Crabtree, H. G. The carbohydrate metabolism of certain pathological overgrowths. *Biochem. J.* **22**, 1289–1298 (1928).

50. Crabtree, H. G. Observations on the carbohydrate metabolism of tumours. *Biochem. J.* **23**, 536–545 (1929).

51. Pfeiffer, T. & Morley, A. An evolutionary perspective on the Crabtree effect. *Front. Mol. Biosci.* **1**, (2014).

52. Diaz-Ruiz, R., Rigoulet, M. & Devin, A. The Warburg and Crabtree effects: On the origin of cancer cell energy metabolism and of yeast glucose repression. *Biochim. Biophys. Acta BBA - Bioenerg.* **1807**, 568–576 (2011).

53. Schuster, S., Boley, D., Möller, P., Stark, H. & Kaleta, C. Mathematical models for explaining the Warburg effect: a review focussed on ATP and biomass production. *Biochem. Soc. Trans.* **43**, 1187–1194 (2015).

54. Hagman, A., Säll, T., Compagno, C. & Piskur, J. Yeast "Make-Accumulate-Consume" Life Strategy Evolved as a Multi-Step Process That Predates the Whole Genome Duplication. *PLoS ONE* **8**, (2013).

CHAPTER 2. STEADY-STATE TRANSMEMBRANE WATER EXCHANGE IN BATCH CULTURES OF *S. CEREVISIAE*

2.1 Introduction

Until now, the relationship between steady-state transmembrane water exchange and cellular function in yeast has been reserved to cells harvested in the stationary phase.[1] In this chapter, we will use batch cultivation as a platform to probe the effects of cell growth on the rate constant for steady-state transmembrane water efflux, k_{io}. Proliferating cells differ from quiescent cells in a number of ways which we hypothesize will impact k_{io}. Due to the presence of newly budded cells, proliferating yeast cells are on average, smaller than mature quiescent cells.[2] Proliferating cells also consume far more nutrients than quiescent cells. We hypothesize that both of these qualities will increase the values for k_{io} in proliferating cells, distinguishing them from quiescent cells. Using a variety of gene knockouts, we will also explore how the presence of a number of transmembrane proteins may affect active k_{io} during periods of growth and quiescence to study the potential mechanism for water exchange.

Batch cultivation of S. cerevisiae

When grown in batch culture, yeast typically exhibit three distinct growth phases. The three growth phases are known as the exponential, post diauxic and stationary growth phases. There is also a lag phase, which is a period of non-growth that occurs when a colony changes carbon sources. Together these phases make up the characteristic growth curve of a Crabtree positive *Saccharomyces cerevisiae* culture.[3,4] In aerobic batch cultivation, a flask containing complete media is inoculated with a starter culture and

agitated on a shaker. The flask is covered by an aerated lid that permits gas exchange and prevents contamination. Batch cultivation is a dynamic process, where the nutrient content and cell density are constantly changing. The rate of colony growth changes as the cells consume nutrients in the media and, in turn, respond to their altered environment. The progression of the culture through the various growth phases can be visualized by plotting the cell density over time. Cell density can be monitored by either optical density measurements at 600 nm (OD_{600}) or through direct cell counting with a microscope and a counting chamber. The growth phases indicates not only a change of metabolism and growth rate, but also a moving population distribution of cells along the cell cycle (Fig. 2.1).[2]

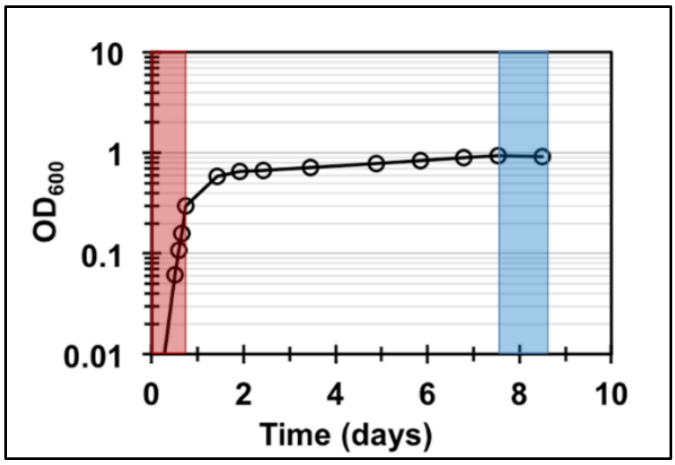

Figure 2.1 A typical growth curve of *S. cerevisiae* grown in complete media. The exponential phase (red) and stationary phase (blue) are highlighted

The moving distribution begins with the majority of cells actively dividing in the exponential growth phase. The cells are growing rapidly and consuming glucose. After all the glucose is consumed the yeast enter the post diauxic phase and begin to metabolize the ethanol generated by fermentation in the exponential growth phase. The rate of cell

growth decelerates during the post diauxic shift, eventually colony growth comes to a halt and it enters the stationary phase when resources are depleted and the majority of the cells are quiescent.[5]

Lag phase

One of the most important characteristics of the fitness of a strain is its ability to overcome changes to the carbon sources of the environment.[6] The delay that occurs upon switching carbon sources is referred to as the lag phase. The length of the lag phase is dependent on how rapidly the cells can alter their gene expression in order to consume a new carbon source.[6] A short lag phase can thus be directly tied to the competitive fitness of a strain in the wild. Bakers, who do not wish to prepare their dough the night before, often utilize "instant" yeast, which has a shorter lag time than other varieties of active baking yeast, due to the inclusion of a number of various rehydration controlling agent as well as citric acid.[7] Some strains have evolved to grow more readily on one particular carbon source, which makes the lag phase vary not only for each strain but also for each carbon source each strain consumes more readily.[4] In batch cultures containing as single fermentable carbon source such as glucose, two lag phases can be observed. The initial lag phase immediately follows inoculation and the second lag phase, sometimes referred to as the diauxic shift, occurs once the glucose in the media is consumed and the catabolism of ethanol begins.

Exponential phase

Once the cells are adapted to a particular carbon source, they begin a stage of steady, exponential growth. Like the duration of the lag phase, the rate of growth in the

exponential phase varies significantly depending on the strain, the carbohydrate and a number of environmental conditions.[3] Strains typically double every 2 – 6 hours in the exponential phase at room temperature in complete media. Throughout the exponential phase, the colony consumes glucose and produces ethanol. The production of ethanol in well aerated conditions is described as the Crabtree effect. Yeast strains exhibiting this phenotype are considered to be Crabtree positive. During the exponential growth phase, the colony grows asynchronously, and the cells are distributed along the various stages of the cell cycle. There average cell size can vary as a result of this distribution, where age and clonal variability both play a role in determining the size of a cell.[8] Interestingly, although the yeast cells are capable of consuming the ethanol from the fermentation metabolic pathway, the cells only do so once all of the glucose (or other sugars) in the media has been depleted. This has led to the make-accumulate-consume theory to explain the evolutionary advantages of the Crabtree effect.[9] Yeast cells have evolved a strategy to consume as much glucose as they can, as rapidly as they can and they process the ethanol later, if needed. Although this strategy is inefficient in terms of ATP produced per molecule of glucose, it likely makes the culture more competitive in the wild.[10,11]

Diauxic Shift and Post Diauxic Phase

Once the glucose in the media is consumed, yeast cells move onto the next available energy source: ethanol. The metabolism of ethanol occurs is a three-step process beginning with the oxidation of ethanol to acetaldehyde by alcohol dehydrogenase (ADH). The acetaldehyde is then converted to acetate which acetyl-CoA synthetase ligates with coenzyme A to produce acetyl-CoA.[12] The post diauxic phase is the period

when the yeast consumes ethanol. This growth phase typically occurs over a few days and results in only one or two culture doublings.

Stationary phase and sporulation

A colony enters the stationary phase when the nutrient content in the media has been completely depleted. This typically occurs after five to seven days of growth in nutrient rich media in standard conditions. During the stationary phase, the cells enter a state of quiescence and have increased stores of the carbohydrates glycogen and trehalose.[2] Trehalose accumulation can protect the quiescent cell from damage by oxidative stress.[13] Interestingly, as the viability of yeast cells in the stationary phase does not always appear to correlate with the intracellular concentration of glycogen or trehalose.[14] There are many mechanistic aspects of metabolism in quiescent cells that remains largely unknown, however, there is indirect evidence pointing to lipid metabolism playing a role.[2]

Diploid yeast cells may also undergo meiosis and create spores upon carbon starvation. [15] The propensity and conditions required for a colony to sporulate is strain dependent and can also be highly influenced by the growth media.[16] Sporulation efficiency can be increased by introducing the cells to a nitrogen poor medium, which consists of primarily of sodium acetate.[17] The transition of a proliferating diploid cell into a mature spore is accompanied by a series of morphological changes.[18] During sporulation, each set of chromosome is duplicated and four enveloping membranes produce two haploid cells of each mating type.[18]

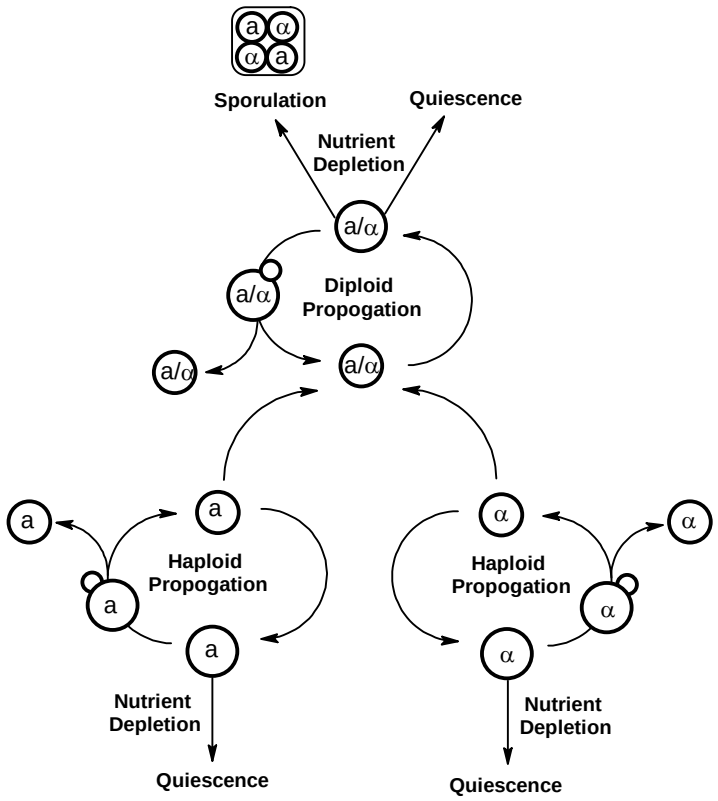

Figure 2.2 A schematic of the possible life cycles of a yeast cell. When nutrients are freely available, yeast cells bud and produce daughter cells. Haploid yeast cells, of either the α or a mating type can propagate in isolation. Diploid cells, containing both the α and a mating type, also freely bud and produce daughter cells when nutrients are present. When diploid cells are starved of nutrients, they enter a quiescent state or they can undergo a process known as sporulation.

Growth and k_{io}

In this chapter, water exchange is investigated with respect to cellular growth using batch cultures of S. *cerevisiae*. Forward light scatter (FSC) was measured to contextualize k_{io} with respect to changes in cellular morphology that may occur along the growth curve. Using a variety of designer deletion mutants made available from the *Yeast Deletion Project*, the contribution of individual membrane proteins to water exchange during

periods of growth and quiescence is also investigated to further understand the mechanism of k_{io} across a growth curve.[19]

2.2 Materials and Methods

Strains

FY4 [MATa], (A gift from Dr. Dunham)

Fleischmann's Active Dry Baker's Yeast (F. Bakers, locally purchased)

Red Star Baking Yeast (locally purchased)

BY4743 [MATa/α his3Δ1/his3Δ1 leu2Δ0/leu2Δ0 LYS2/lys2Δ0 met15Δ0/MET15 ura3Δ0/ura3Δ0] (purchased from EUROSCARF)

BY4743 (*Δpma1*) [MATa/α; ura3Δ0/ura3Δ0; leu2Δ0/leu2Δ0; his3Δ1/his3Δ1; met15Δ0/MET15; LYS2/lys2Δ0; YGL008c/YGL008c::kanMX4] (purchased from EUROSCARF)

BY4742 (*Δaqy2*)[MATα; ura3Δ0; leu2Δ0; his3Δ1; lys2Δ0; YLL052::kanMX4] (purchased from EUROSCARF)

BY4742 (*Δcch1*) [MATα; ura3Δ0; leu2Δ0; his3Δ1; lys2Δ0; YGR217W::kanMX4] (purchased from EUROSCARF)

BY4742 (*Δnha1*) [MATα; ura3Δ0; leu2Δ0; his3Δ1; lys2Δ0; YLR138W::kanMX4] (purchased from EUROSCARF)

BY4742 (*Δpmr1*) [MATα; ura3Δ0; leu2Δ0; his3Δ1; lys2Δ0; YGL167C::kanMX4] (purchased from EUROSCARF)

Batch cultivation and OD_{600}

Pre-cultures were grown overnight in complete media (YPD, Difco) before the batch cultures were inoculated. Each strain was grown in triplicate in 300 mL of YPD in 500 mL flasks topped with aerated lids (Pyrex). The flasks were shaken vigorously to maintain thorough aeration for the duration of the experiment. Cell density was

monitored using an optical density at 600 nm wavelength using a Bio-Rad UV-Vis spectrometer. Culture samples were diluted 1:30 (*v*/*v*) before cell density measurements.

Sporulation protocol

Cells were first grown overnight in pre-sporulation medium containing 5% glucose, 3% nutrient broth (Difco), and 1% yeast extract (BD Diagnostics), (*m/v*). After 24 hours of growth in the pre-sporulation medium, the cells were filtered and transferred to sporulation medium containing 1% potassium acetate, 0.005% zinc acetate (*m/v*) and supplements of uracil ($20mgL^{-1}$), histidine ($20mgL^{-1}$), and leucine ($30mgL^{-1}$). Cells were grown in triplicate cultures and exposed to sporulation media for one week before water exchange measurements.[17]

NMR sample preparation

For each water exchange measurement between 15 - 30 mL aliquots were collected from the three replicate cultures and centrifuged at 900 g for one minute. The supernatant was removed and combined with the gadolinium-based contrast (GBCA), Prohance (gadoteridol, Bracco Imaging), to make a 10 mM Gd^{3+} solution. Each cell sample was washed three times with the doped supernatant and transferred to a heavy walled NMR tube. The samples were then pelleted into heavy walled NMR tubes (Wilmad 535PP) using a centrifuge at 900 g for two minutes. The total pellet preparation time was 8 minutes.

Pelleting samples both increases the intracellular volume and prevents settling over the course of the measurement. However, it does mean that a substantial quantity of cells was

required for each NMR measurement: on the order of 10^9 cells per sample. Although 10^9 cells were easily obtained with 15 mL of the stationary phase culture, 30 mL of culture was needed to produce pellets in the late-exponential phase.

NMR measurements

The longitudinal relaxation rate constants ($R_1 = 1/T_1$) were measured using an inversion recovery pulse sequence on a Bruker Avance III 600 MHz spectrometer, equipped with a temperature controlled TXI probe set to 25°C. Samples were left to acclimatize for four minutes while the 90° pulse was calibrated. A 90° pulse calibration was performed before each measurement by collecting a nutation spectrum and calculating the 90° pulse length from the 360° pulse. The 90° pulse length ranged from 9.5 – 10.5 μs. An inversion recovery pulse sequence (180° – τ – 90°) was used to measure longitudinal relaxation. Each longitudinal relaxation measurement consisted of four scans and 32 points with a variable delay (τ) ranging from 1 ms to 3 s. The relaxation delay was 3.5 s. The total measurement time was 10 minutes.

2SX fitting parameters

The R_1 data collected was fit to the 2SX system of equations described in Chapter 1 to calculate k_{io}. The fitted 2SX parameters were the intracellular water mole fraction (p_i), the relaxivity of the contrast agent (r_1) and the transmembrane water exchange rate constant (k_{io}). The value of the intrinsic intracellular water exchange rate constant, R_{1i} was set to 1.1 s^{-1}, the extracellular contrast agent concentration, [RR] was set to 10 mM, and the relaxation rate of contrast free extracellular water, R_{1eo}, was set as 0.3 s^{-1}.

Calculation of growth rate

Growth rates were calculated by first plotting the time *vs* OD_{600} absorbance data logarithmically then examining the growth curves for linear segments. These linear segments were then fit to the exponential function in Eqn. 2.1.

$$A(t) = A_0 e^{rt} \quad \textbf{(2.1)}$$

Where A(t) is the absorbance at a given time, A_0 is the starting absorbance, r is the growth rate constant and t is time. These can be converted to a culture doubling time (T_d), Eqn. 2.2, which is often used as a more tangible and convenient method for describing growth. The exponential growth rates presented are an average of three cultures for each strain.

$$T_d = \frac{\ln(2)}{r} \quad \textbf{(2.2)}$$

Flow cytometry measurements:

Samples of cells for flow cytometry measurements were collected during the exponential and stationary growth phases were fixed using 4% paraformaldehyde in phosphate buffered saline (PBS) and stored at -80ºC. Forward light scatter (FSC) measurements were collected for each fixed sample using flow cytometry. The average cell size of a sample was approximated by comparison with a standard curve made from polystyrene beads measuring 1, 3 and 6 μm in diameter. The mean FSC from the histogram was compared to a standard curve and the average diameter of cells was approximated in both

the stationary and exponential growth phases. The surface area and volume of the yeast was geometrically approximated as a sphere.

2.3 Results

k_{io} across a growth curve of wild type strains

The rate constant for transmembrane water efflux, k_{io}, was measured across the growth curves of a number of wild type strains. The wild type strains surveyed consist of both common laboratory strains and commercially available baking strains. Fleischmann's baking yeast (F. Baker's ATCC 7794) and Red Star baking yeast are commercially available baking strains and were locally purchased, while BY4742, BY4743 and FY4 are all common laboratory strains and were either gifts from another lab or purchased through a strain database known as EUROSCARF. The behavior of water exchange was observed to differ between common laboratory strains and the commercially available baking strains (Fig. 2.3).

In the two baking strains, k_{io} is greater in exponentially growing cells than in quiescent stationary phase cells. This indicates that water exchange is more rapid in the exponential phase than in the stationary phase for these strains. For the Red Star baking strain (ATCC 58532) k_{io} was found to be 4.36 s^{-1} (SD = 0.060) in the late-exponential growth phase. The rate of water exchange slowed as the colony matured to the stationary phase and k_{io} was observed to decrease to 1.39 s^{-1} (SD = 0.045). Fleischmann's baking yeast (F. Baker's, ATCC 7794), was also observed to exchange water rapidly during growth than during quiescence. The value of k_{io} measured for the late exponential growth phase of F.

Baker's cells, was observed to be 3.45 s^{-1} (SD = 0.094). As the culture progressed to the stationary phase where k_{io} was observed to decrease to 1.34 s^{-1} (SD = 0.020).

The laboratory wild type strains (BY4742, BY4743 and FY4) exhibit markedly different behavior. The values for k_{io} in the three commercially available strains showed little change across the growth curve. FY4 (Mat α) is a prototrophic haploid strain developed by Fred Winston's lab. The k_{io} value for FY4 in mid-exponential growth phase was found to be 2.44 s^{-1} (SD = 0.067). In the stationary phase, a slight increase to k_{io} was observed 2.67 s^{-1} (SD = 0.183). BY4743 is a homozygous diploid made popular due to the *Yeast Deletion Project*.[20] BY4743 cells growing in the late exponential phase were observed to exchange water k_{io} was observed to be 3.67 s^{-1} (SD = 0.393). When these cells reached the stationary phase the value for k_{io} was measured to be 3.73 s^{-1} (SD = 0.176). The value

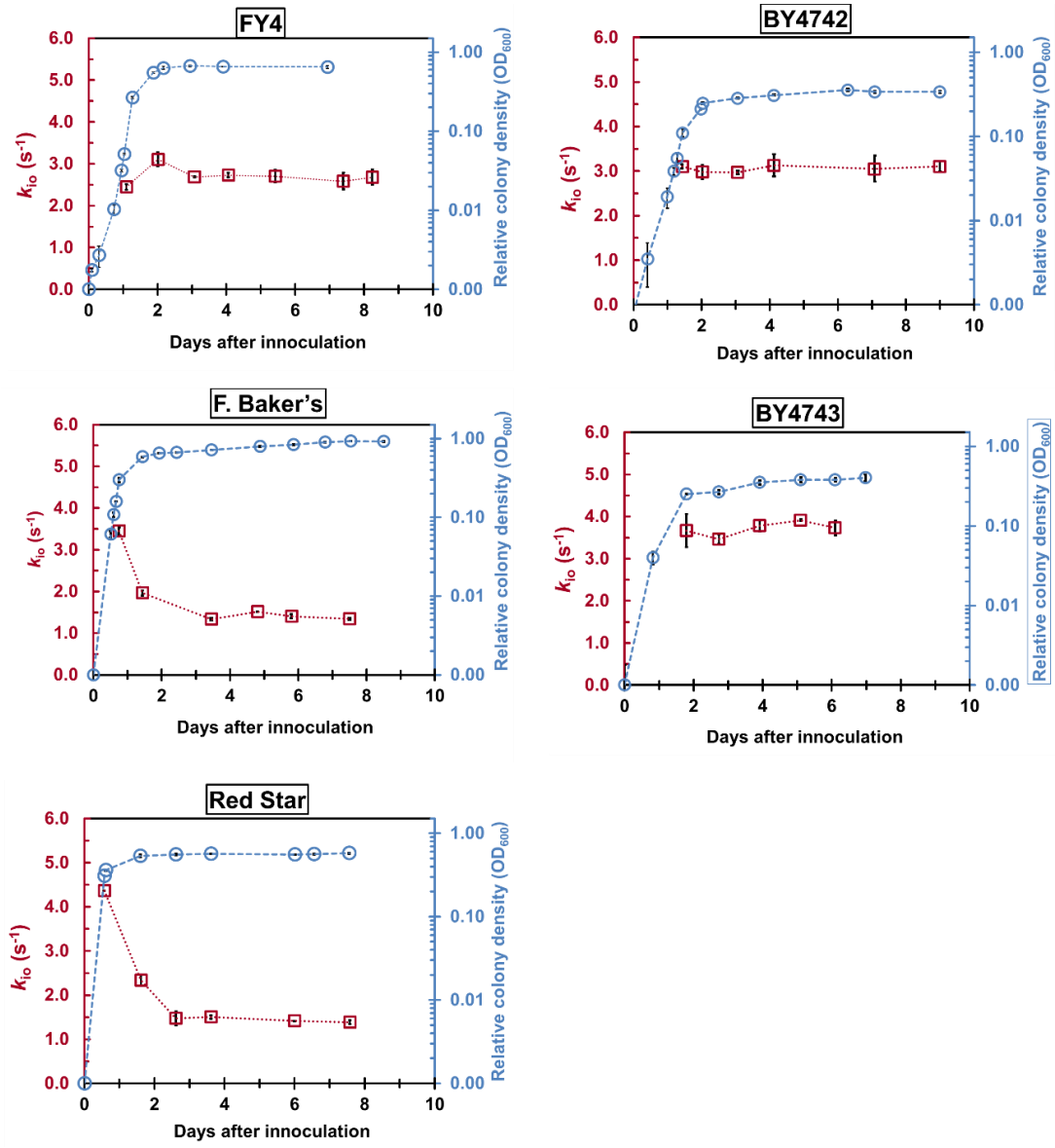

Figure 2.3 The rate constant for transmembrane water efflux, (k_{io}, shown in red) was measured across the growth curve of a number of wild type strains of Saccaromyces cerevisiae. The growth curve was measured using optical density at 600 (OD_{600}, shown in blue) Each data point represents the mean value from three biological replicates. Error bars represent the one standard deviation above and below the mean.for k_{io} in the late exponential growth phase of the haploid strain BY4742 was found to be 3.10 s^{-1} (SD = 0.051). In the stationary phase, k_{io} was observed to be 3.11 s^{-1} (SD = 0.119).

Growth phase and cell size in wild type strains

Cell size distribution was approximated using flow cytometry. Histograms of forward light scatter (FSC, arbitrary units) were collected during the exponential and stationary growth phases. The histograms for the wild type strains measured can be seen in Fig. 2.4. As was the case in the k_{io} measurements, there is a noticeable difference between the FSC histograms of the commercially available baking yeast strains and the FSC histograms of the laboratory strains.

The histograms for the Red Star baking strain reveal that the distribution of cells was more uniform in the exponential growth phase than in the stationary growth phase. Stationary phase cells of this strain appear to be larger than the exponentially growing cells. There appears to be two populations of cells within the stationary phase histogram of the Red Star strain. One of these populations is about the same size as the exponentially growing cells, and the other considerably larger.

The FSC histograms collected in the exponential phase of Fleischmann's baking yeast (F. Baker's) also appeared to be more uniform than the stationary phase samples. The stationary phase histogram consists of three populations, one that is smaller than exponentially growing cells, one that is roughly similar size and one that is considerably larger than exponentially growing cells.

The FSC histograms for the laboratory strains FY4, BY4742 and BY4743 were considerably more uniform between the exponential and stationary growth phase samples in comparison to the commercially available baking strains.

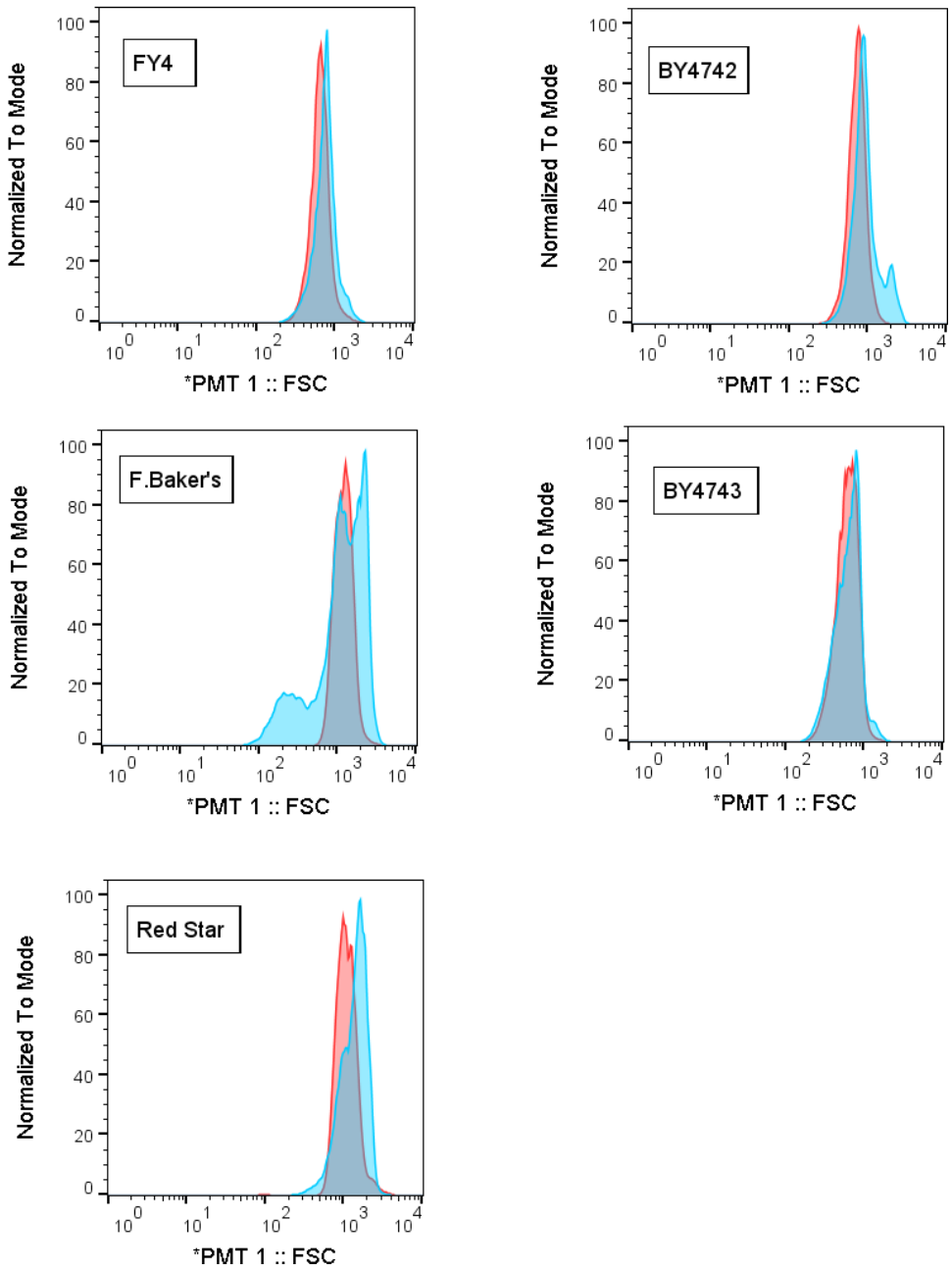

Figure 2.4 Forward light scatter histograms were measured were collected using flow cytometry. Each histogram is composed of more than 10,000 counts. Histograms were collected for each wild type strain in the exponential (red) and stationary (blue) growth phases.

Exponential growth rate and wild type k_{io}

The maximum growth rates and k_{io} of the wild type strains are compared in Table 2.1. There was a substantial difference in the growth rates of the wild type strains. The fastest growing strain, F. Baker's, doubled twice as fast during the exponential growth phase as slowest growing strain. There does not appear to be a clear correlation between maximum growth rate and k_{io}. F. Baker's yeast and the laboratory strain BY4743 were found to have very similar values for k_{io} in the exponential phase however; the doubling time of Fleischmann's yeast was just under half the doubling time of BY4743. The exponential doubling time of the FY4 laboratory yeast was on the same order as the baking yeast strains.

Table 2.1 Wild Type Strains Growth Rates

Strain	Growth Rate (hr^{-1})	T_d (hrs)	k_{io} (s^{-1})
FY4	0.251	2.727	2.44
F. Baker's	0.264	2.628	3.45
BY4743	0.127	5.458	3.67
BY4742	0.151	4.590	3.11
Red Star	0.232	2.985	4.36

Sporulation and k_{io}

The BY4743 and F. Baking strains were inoculated in sporulation media. The value for k_{io} measured in BY4743 cells exposed to sporulation media for one week was over 6 standard deviations lower than the values observed for BY4743 cells grown in YPD for

the same time period (stationary phase, Fig 2.5). The average value of k_{io} in the sporulated cells was found to decrease to less than half of the value measured in the exponential and stationary growth phases. This difference is almost identical to the decrease in k_{io} we observe between the exponential and stationary phase baking yeast. Notably, the value measured for k_{io} in F. baker's yeast incubated in sporulation medium was not appreciably different from the value of k_{io} for stationary phase cultures.

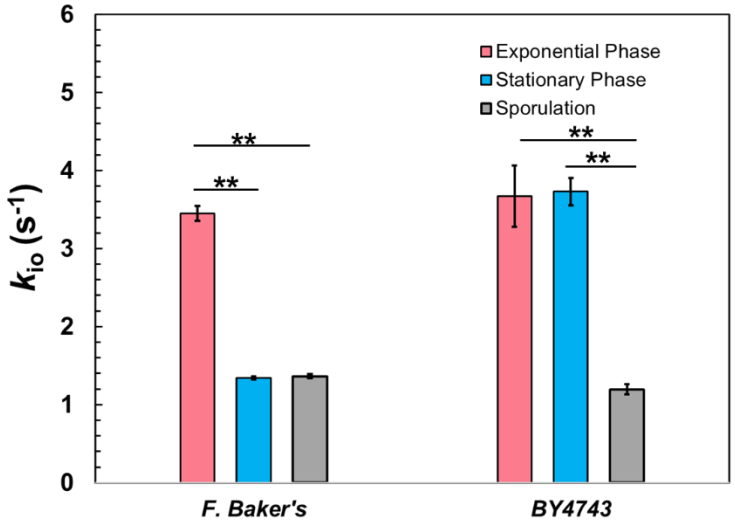

Figure 2.5 The transmembrane water exchange rate constant (k_{io}) was compared between the wild type strains, Fleischmann's baking yeast and BY4743 in a number of conditions. The exponential phase and stationary phase values of k_{io} were measured in the batch cultures grown in YPD. The sporulation values of k_{io} were measured after the strains were inoculated in sporulation media for one week. Asterisks indicate statistical significance between measurements (P (T<=t) two-tail, **P ≤ 0.01).

k_{io} in knockout strains

The Saccharomyces Genome project has led to the creation of a number of knockout databanks for common yeast strains. There are entire collections of non-essential gene knockouts for the laboratory strains BY4742 and BY4743. A number of genes that may be associated with transmembrane transport were investigated to probe possible mechanisms of water exchange. The descriptions for each knockout can be found in Table 2.2.

Table 2.2 These five knockouts were selected to give a broad survey into the relationship between water exchange kinetics and cellular function. The descriptions were taken from the *Saccharomyces Gene Database* (SGD).[20]

Gene	Systematic Name	Function
cch1	YGR217W	Voltage-gated high-affinity calcium channel; involved in calcium influx in response to some environmental stresses as well as exposure to mating pheromones
aqy2	YLL052C	Aquaporin water channel that mediates water transport across cell membranes
pma1	YGL008C	Plasma membrane P2-type H^+ATP*ase*; pumps protons out of cell; major regulator of cytoplasmic pH and plasma membrane potential
nha1	YLR138W	Na^+/H^+ antiporter; involved in sodium and potassium efflux through the plasma membrane
pmr1	YGL167C	High affinity Ca^{2+}/Mn^{2+} P-type ATP*ase*; required for Ca^{2+} and Mn^{2+} transport into Golgi

In a similar fashion to the wild type experiments described previously, k_{io} was measured across the growth curve of the knockout strains (Fig. 2.6). Most of the knockouts were of the haploid BY4742 genotype, however, the strain *Δpma1* is a heterozygous knockout of

the diploid wild type strain BY4743. The *Δpma1* mutant accounted for the largest observed decrease in k_{io}. Notably, this is the only knockout for which the decrease in k_{io} persists across all growth phases.

In the *Δaqy2* strain, k_{io} was observed at 2.61 s^{-1} (SD = 0.099) in the exponential growth phase which is slower in comparison to the wild type BY7472. When the colony matured, k_{io} was observed to rise to 3.59 s^{-1} (SD = 0.448) in the stationary phase, which was greater than wild type stationary phase value. For the *Δcch1* knockout strain, k_{io} was observed to be 2.60 s^{-1} (SD = 0.051) in the exponential which represents a reduction in water exchange in comparison to the exponentially growing wild type strain, BY4742. Similar to *Δaqy2,* the value for k_{io} in the *Δcch1* strain was observed to increase as the culture approached the stationary phase. During the stationary phase, k_{io} of the *Δcch1* knockout was observed to be 3.95 s^{-1} (SD = 0.071). This represents an increase in comparison with the stationary phase wild type. The *Δnha1* strain showed the most variability of any knockout sampled. The average k_{io} measured in the exponential growth phase was 3.17 s^{-1} (SD = 0.259), which represents a slight decrease from the wild type BY4742 value. The average k_{io} value measured in the stationary phase increased to 3.89 s^{-1} (SD = 0.461). The *Δpmr1* mutant strain had a surprising effect on the water exchange rate across the growth curve. The value of k_{io} measured in the exponential phase was 3.54 s^{-1} (SD = 0.153). These values were greater than those observed for the wild type BY4742 exponential phase. Interestingly, k_{io} decreased steadily each day until it reached 2.48 s^{-1} (SD = 0.033) in the stationary phase, which was considerably lower than the wild type BY4742 value.

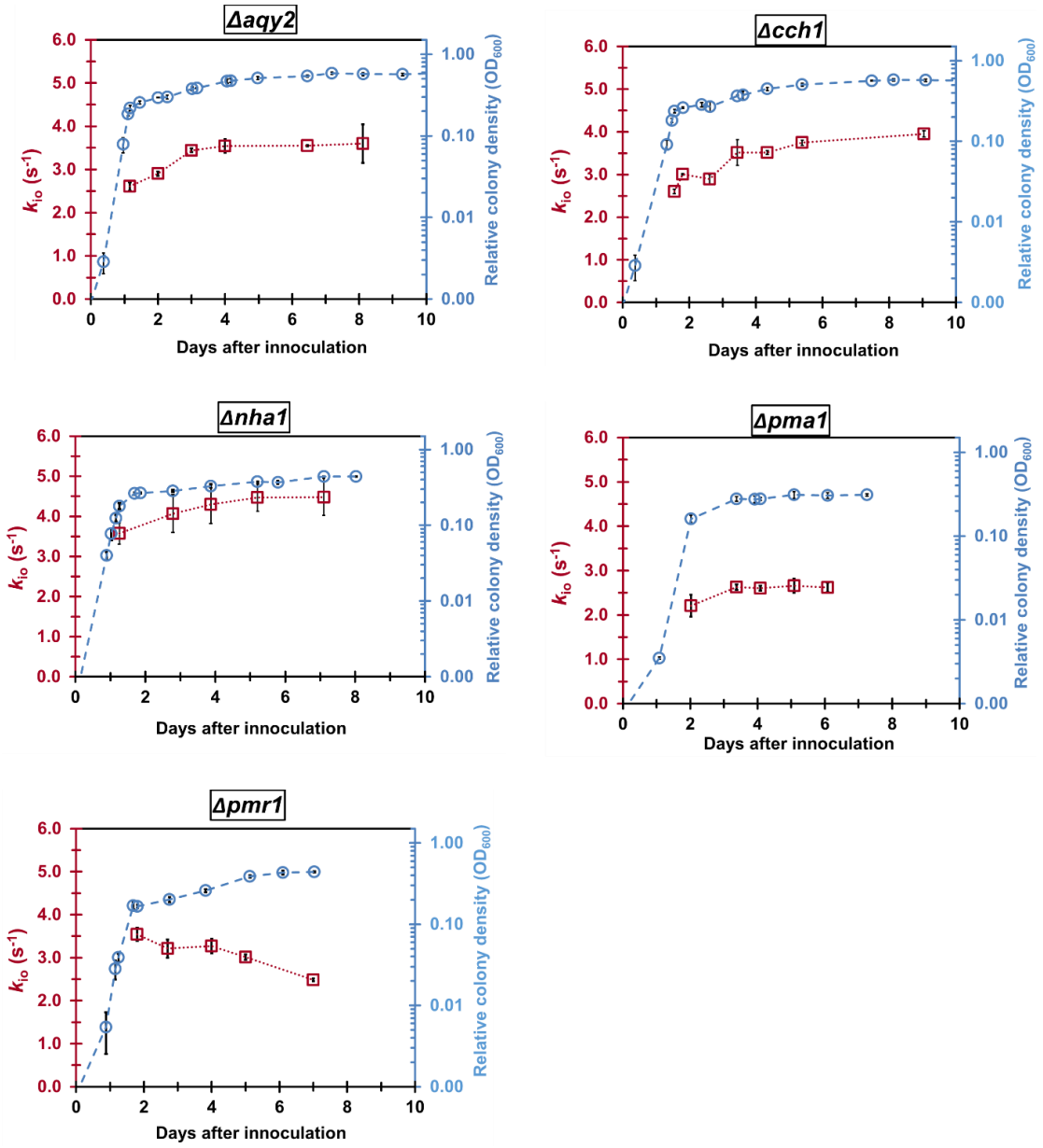

Figure 2.6 The rate constant for transmembrane water efflux, k_{io}, (shown in red) was measured across the growth curve of a number of knockout strains of *S. cerevisiae*. The growth curve was measured using optical density at 600 (OD_{600}, arbitrary units, shown in blue) Each data point represents the mean value from three biological replicates. Error bars represent the one standard deviation above and below the mean.

FSC across a growth curve of knockout strains

Samples from each knockout strain were collected during the exponential and stationary growth phases and measured using flow cytometry. Histograms of forward light scatter (FSC, arbitrary units) for the exponential and stationary growth phases of each knockout strain and can be seen in Fig. 2.7. These histograms can serve to estimate how the average cell size may change during the growth and quiescence. They may also serve to measure the potential effect of each knockout on cell size with respect to the wild type.

The FSC histograms for the *Δaqy2, Δcch1,* and *Δnha1* knockouts all feature similar distributions and reveal that the average cell in the exponential phase is slightly smaller than the average cell in the stationary phase. These histograms feature distributions that are similar to the wild type BY4742 strain. The FSC histograms for the *Δpma1* strain reveal that very little change occurs to the average cell size between the exponential and stationary phase. The *Δpma1* histograms are similar to the wild type BY4743 strain.

The *Δpmr1* knockout had the most dramatic effect on FSC histograms. The deletion of *pmr1* caused a second, larger population to appear in the stationary phase. The stationary phase histogram of the *Δpmr1* strain is significantly different from the BY4742 wild type strain.

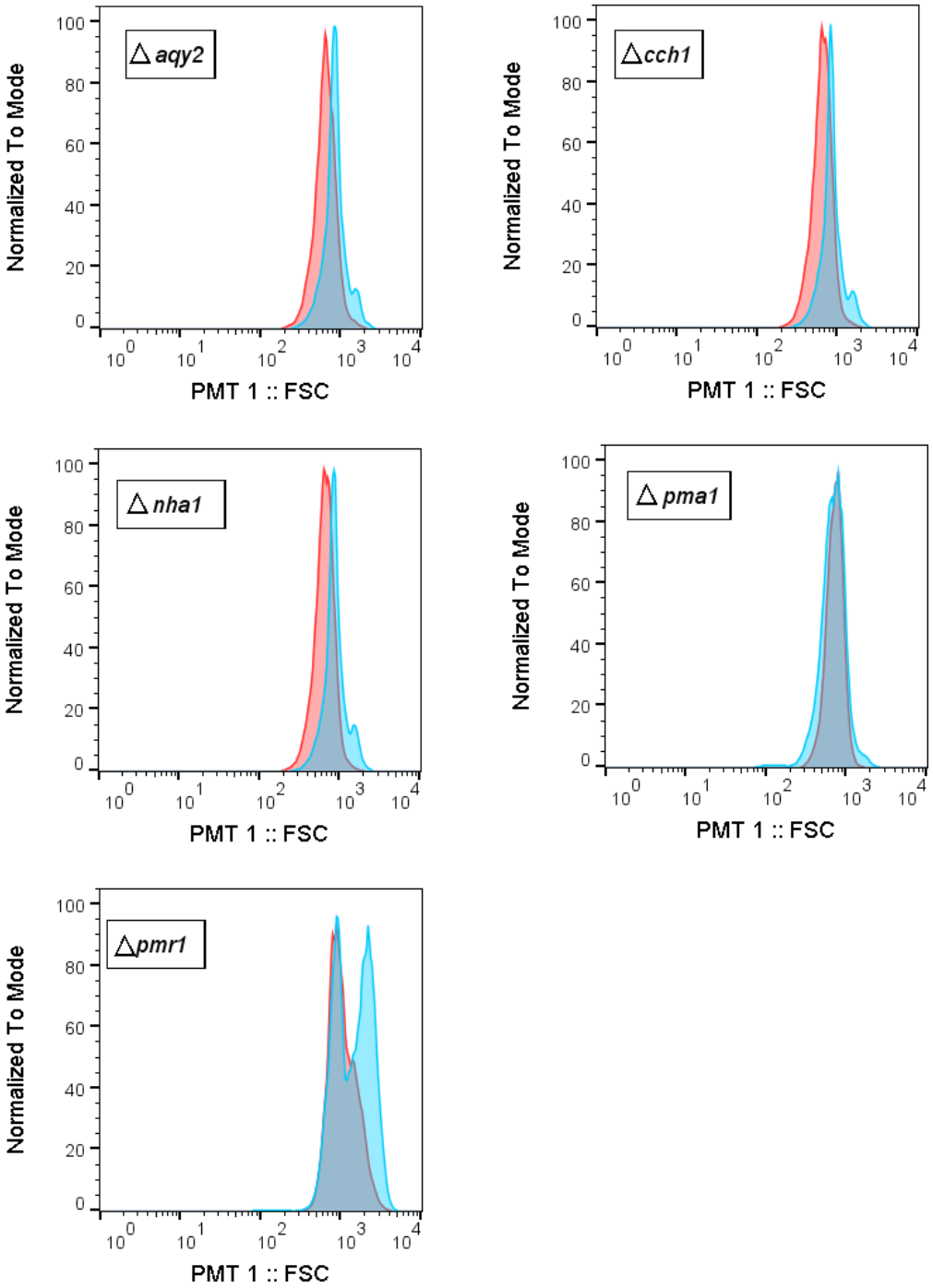

Fig 2.7 Forward light scatter histograms were collected for each knockout strain using flow cytometry. Each histogram is composed of more than 10,000 counts. Histograms were collected for each knockout strain in the exponential (red) and stationary (blue) growth phases.

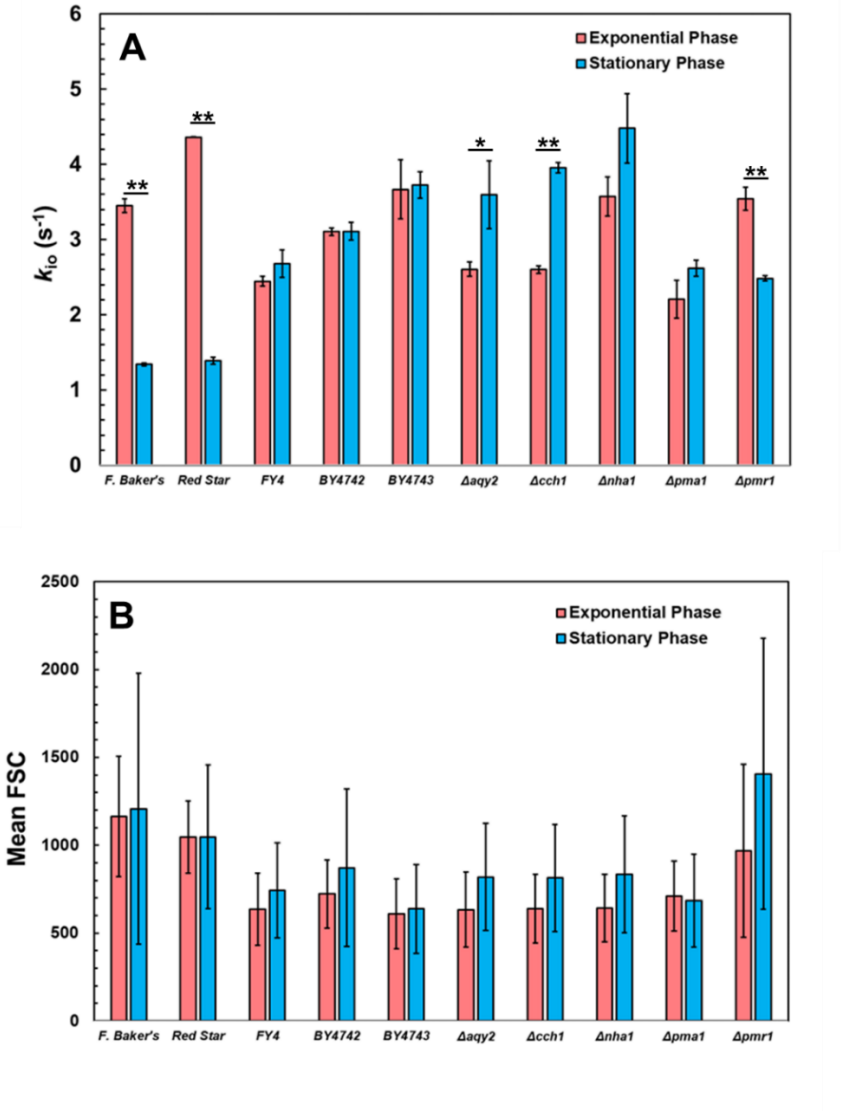

Fig 2.8 (**A**)Transmembrane water efflux rate constants, k_{io}, were measured in the exponential (red) and stationary (blue) growth phases of a series of wild type and knockout strains of S. cerevisiae. Error bars represent one standard deviation above and below the mean (n = 3). Asterisks indicate statistically significant differences between k_{io} values measured during the exponential and stationary growth phase (P (T<=t) two-tail, * P ≤ 0.05, **P ≤ 0.01). (**B**) The mean forward light scatter intensity (FSC, arbitrary units) was measured using flow cytometry to provide context into the cell size changes that occur between the exponential (red) and stationary (blue) growth phases. Error bars represent one standard deviation above and below the mean (n = >10,000).

k_{io} and knockout growth rates

The exponential growth rates for the knockout strains can be seen in Table 2.3. The deletion of the genes selected for this study did not appear to have an effect on growth rate, the only exception was *Δaqy2*, which was observed to have a slightly faster growth rate with respect to the wild type strain.

Table 2.3 Knockout Strains Growth Rates

Knockout	Growth Rate (hr^{-1})	T_d (hrs)	k_{io} (s^{-1})
Δaqy2	0.214	3.25	2.61
Δcch1	0.155	4.49	2.60
Δnha1	0.168	4.14	3.57
Δpma1	0.140	4.94	2.21
Δpmr1	0.152	4.56	3.54

k_{io} and the surface to area ratio (SA/V)

The mean FSC during the exponential and stationary growth phases was calculated for each strain and is presented in Fig. 2.8. These mean FSC measurements can be compared to the k_{io} measurements to get an understanding about how the changes to cell size may impact k_{io}. Using the spherical approximations for surface area and volume, and calibration to a standard curve of polystyrene beads, the average SA/V ratio was approximated for all strains during both the exponential and stationary phases. Approximations for the surface area to volume ratio (SA/V) were plotted against the values of k_{io} observed during both growth phases in Fig. 2.10.

2.4 Discussion

Why does k_{io} decrease across the growth curve of baking yeast?

The wild type strains measured in this work consist of both commercially available baking strains (Red Star, F. Baker's) as well laboratory cultivated strains (BY4743, BY4742, FY4). All strains are Crabtree positive and exhibit three growth phases in their respective growth curve. The growth curve for each wild type strain is unique with respect to the duration of the lag phase, the slope of the exponential and post diauxic phases as well as the timing for the entrance into the stationary phase. Because of these differences, it is important to compare the values for k_{io} to the growth phase of that particular strain and not simply with the time after inoculation value as the timing of the growth phases can differ between strains.

It is clear from a comparison of the wild type strains, that the behavior of water exchange across the growth curve of yeast cultures is not conserved among strains. In the commercially available baking strains, F. Baker's and Red Star, k_{io} is observed to decrease across the growth phase. In the laboratory strains, we observe that k_{io} is consistent across the growth curve.

An examination of the cells with flow cytometry reveals that the baking strains also exhibited the greatest change in morphology upon culture maturation. The stationary phase FSC histograms of the Red Star and F. Baker's strain contain multiple populations, while the FSC histograms in the baking strains were far more uniform and exhibited little change between the growth phases.

What causes the baking strains to drastically alter k_{io} upon entrance to the stationary phase? One possible explanation for the difference in water exchange behavior between these wild type strains is the propensity for sporulation. Sporulation efficiency is known to be highly variable, but it can be induced with nitrogen deficient sporulation media, which consists primarily of sodium acetate.[16,21]

Sporulation results in a significant restructuring of the cellular architecture.[18] Unlike mitosis, where the mother yeast cell produces daughter yeast cells through the process of budding, upon sporulation, the chromosomes are separated by meiosis, which produces four haploid nuclei (two of each mating type).[15,18] Each of these nuclei is enveloped within an additional membrane inside the cytoplasm of the original mother cell.[15,18] The mother cell membrane remains intact even after the spores have matured. The four nuclei enveloped in the mother cell often appear as distinct tetrads, which can be seen in Fig. 2.9.

The ability for spores to withstand harsh conditions is likely the primary function of spore formation.[22] Sporulated cells have a higher resistance to acetic acid, sodium hydroxide, ether, high temperatures, and high concentrations of sodium chloride. Sporulated cells have also been observed to pass through the digestive tract of *Drosophilia* flies unscathed which has led to speculation that sporulation may be advantageous because it opens the possibility of insect vectors.[22] Strains with a high sporulation propensity may be beneficial to use as consumer yeast because of the increased robustness of the spore. This may have led to the commercial adoption of strains that were eager to form spores.

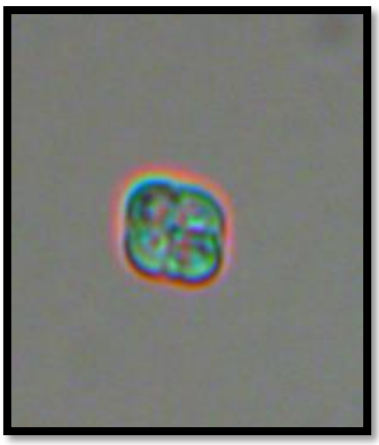

Figure 2.9 An image taken of a spore from Fleischmann's baking yeast using an inverted objective microscope at 400× magnification

The tendency for a diploid cell to sporulate is not only strain dependent, but also medium dependent. There is a vast range of sporulation efficiency for strains grown in glucose.[15,21] Sporulation occurs only in polyploidy strains, so in order to test the effect of sporulation on k_{io} within laboratory strains, the homozygous diploid BY4743 was selected to study alongside F. Baker's yeast.

The k_{io} values observed in Fig 2.5 indicate that sporulation media induces a change in cellular water exchange rate. The BY4743 strain appears to sporulate at low efficiencies in the typical batch culture media (which contains glucose), however, when grown in sporulation media, a higher percentage of BY4743 cells can be induced to sporulate. This increase in sporulation efficiency appears to drastically alter the water exchange kinetics. F. Baker's strains sporulates in glucose based media, which may be the reason why little change in k_{io} is observed when the strain is grown in sporulation media. These observations are consistent with the limited literature available on F. Baker's yeast.[23]

The full extent of the effect of sporulation on k_{io} is unclear. The additional membrane is almost certain to change in passive permeability to the membrane certainly contributes to the decrease observed in k_{io}, but it is difficult to say with certainty that a change in active water exchange does not also play a role. In addition to the development of an additional membrane within the mother cell sporulation involves a significant change in gene expression of a number of membrane transporters.[16]

Active and passive k_{io} across the growth curve

The k_{io} value observed for a cell pellet is the sum of the active and passive components. Understanding how the average cell size changes is key to understanding if the changes to k_{io} observed are due to a change in the active and passive k_{io}. Although it may be possible to infer changes to passive and active k_{io} in the baking strains, active and passive k_{io} are more easily studied in the wild type BY4742/BY4743 and gene knockout strains. This is due to the more uniform distributions of FSC for these strains, which allows for greater confidence in the cell size analysis, and therefore greater confidence into the breakdown of active and passive components.

Although the cells of the BY4742 strain (and to a lesser extent the BY4743 strain) appear to slightly grow in size upon maturation, a corresponding change in k_{io} was not observed between samples collected in the exponential and stationary growth phases. An increase in cell size should lead to a corresponding decrease in the contribution of passive k_{io}. If the total k_{io} value observed remains constant, and the passive k_{io} decreases due to an increase in cell size, then active k_{io} must compensate. Interestingly, this suggests that active k_{io} does not decrease when a culture enters the stationary phase.

It is somewhat paradoxical to suggest that active k_{io} should not decrease in stationary phase cells. Active k_{io} is, by definition, directly or indirectly driven by energetically demanding processes. One might assume that these energetic processes are more costly when nutrition is in short supply, however, these observations would suggest they occur even when the nutrients in the media are completely consumed.

The simplest explanation for active k_{io} is that water is co-transported with nutrients, and thus, scales with nutrient uptake. From this comparison of exponential and stationary phase cells, it is clear that this explanation is not adequate. Active k_{io} is not representative of cellular growth or nutritional uptake in yeast cells. Although there is clearly more material crossing the membrane in the exponential phase when compared to the stationary phase, steady-state water exchange is more rapid in in the stationary phase.

Mechanisms of water exchange

To further unravel the nature of k_{io} across the growth curve, a number of gene knockouts were examined. Previous studies conducted by Zhang and colleagues have demonstrated that the heterozygous deletion of the gene *pma1,* which codes for an ATP driven proton pump known as H^+ATP*ase,* lowers k_{io} in stationary phase yeast cells.[1] Zhang and colleagues have also previously demonstrated that H^+ATP*ase* inhibition with ebselen lowers k_{io} in yeast cells in the stationary phase.[1] Our results from the stationary phase align with the values reported of these previous studies. In addition to observations of k_{io} in the stationary phase, we report the values for k_{io} for the H^+ATP*ase* in the exponential phase.

The heterozygous deletion of *pma1* suppresses water exchange across all growth phases. The FSC histograms for the *Δpma1* strain are very similar in the exponential and stationary phase. There is also very little difference between the mean FSC of the BY4743 wild type and of the *Δpma1* strain. This indicates that the changes to k_{io} observed between the wild type and knockout strain are due almost entirely to changes in active k_{io}. The *pma1* heterozygous knockout was the most impactful knockout to k_{io} observed, which supports the hypothesis that water exchange in yeast is driven by the H^+ATP*ase*. Although the H^+ATP*ase* contributes significantly to k_{io} over the entire growth curve, other methods of water transmembrane transport, do not appear to have similarly consistent contributions to k_{io}. The deletion of *aqy2* and *cch1* impacts k_{io} differently depending on the growth phase.

The knockout strains *Δcch1* and *Δaqy2* have suppressed values for k_{io} in the exponential phase, however, this suppression is not maintained through to the stationary phase. Instead, the values for k_{io} measured in the stationary phase of the *Δcch1* and *Δaqy2* strains were observed to increase beyond the wild type stationary phase values. In *Δcch1* and *Δaqy2* strains, the FSC was also observed to increase when moving from the exponential to the stationary growth phase.

The value of k_{io} increases when moving to the stationary phase in the *Δcch1* and *Δaqy2* strains. This change to k_{io} occurs even as the average cell increases size. An increase in cell size implies that the passive contribution to k_{io} decreases. Despite the decrease in passive k_{io}, the overall k_{io} increases, which suggests an increase in active k_{io} in the stationary phase. Like in the wild type BY4742 strain discussed previously, it appears

that the *Δcch1* and *Δaqy2* strains have elevated contributions of active k_{io} in the stationary phase.

There are a number of peculiarities that arise from these knockout studies. We have observed that k_{io} of the *Δcch1* and *Δaqy2* increases past the k_{io} observed for the wild type strain in the stationary phase. Why might the k_{io} of a knockout increase beyond the wild type value? It is peculiar that a strain with a gene associated with water transport knocked out would exhibit k_{io} values that exceed the wild type value. For this, we propose a tentative answer, but one that should certainly be studied further. The deletion of any gene may cause compensatory changes within the regulation of water exchange.

Another peculiarity is that in the wild type BY4742 strain as well as in the knockouts *Δaqy2* and *Δcch1*, active k_{io} appears to increase in the stationary phase. This observation appears to conflict with the portion of the AWC hypothesis that predicts a connection between metabolism, cellular energetics and active k_{io}.

The effects of intracellular ATPases on k_{io}

The gene *pmr1* codes for an intracellular ATP*ase*, responsible for Ca^{2+} and Mn^{2+} transport in the Golgi apparatus.[24–26] The gene *pmr1* is required for normal Golgi function.[24] A number of downstream effects can be seen in the *pmr1* knockout. The *Δpmr1* strain is deficient of an intracellular ATP*ase* located on the Golgi apparatus. The deletion does not have a significant effect on maximum growth rate, however, there was a substantial change in morphology which was revealed by the FSC measurements. The FSC histogram for *Δpmr1* depicts a change in morphology occurs due to this mutation

which likely contributes to the decrease in the observed k_{io} across the growth curve. The involvement of the Golgi apparatus in lipid synthesis may explain both the size and k_{io} irregularities observed for this knockout strain. Lipid metabolism likely plays a key role in sustaining k_{io} in stationary phase cells.

SA/V vs k_{io}

When plotted against each other, the SA/V ratio and k_{io} can provide insight as to what processes are responsible to changes to water exchange. If changes to k_{io} were driven solely by changes in cell size, then we should expect a moderate degree of positive correlation between the SA/V ratio and k_{io}. Fig. 2.10 shows that when this exercise is conducted in exponential phase cells and stationary phase cells, two trends emerge. The degree of correlation between SA/V and k_{io} is very low in both charts of Fig. 2.10, which implies that active k_{io} is a significant contribution to the total k_{io}.

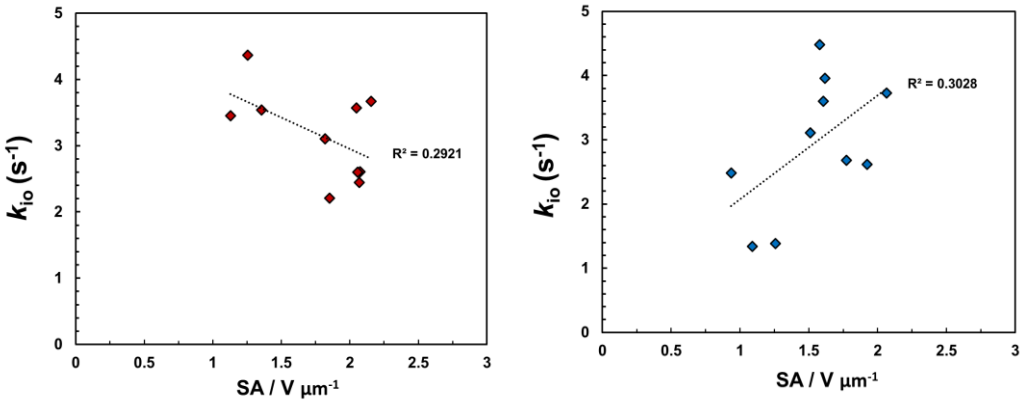

Figure 2.10 The surface area to volume ratio (SA/V) and k_{io} shows a low degree of negative correlation in exponential phase yeast cells (left, red) and a low degree of positive correlation with stationary phase yeast (right, blue). The trendlines were only to guide the reader's eye to the potential difference between the stationary and exponential phases.

2.5 Conclusions

The first question we sought to answer in this chapter concerned the relationship between nutrient transport and steady state water exchange. The initial hypothesis tested was that faster growing cells uptake nutrients at a more rapid pace than quiescent cells, leading to faster rates of active k_{io}. To answer this, k_{io} was measured across the growth curves of a selection of wild type and knockout yeast strains and compared to FSC measurements to estimate cell size. In two commercially available baking yeast strains, k_{io} was observed to drastically decrease upon entrance to the stationary phase. This was an intriguing result, that at first glance, appears to confirm the initial hypothesis however, it did not hold true for other widely used wild type laboratory strains such as BY4742, BY4743 and FY4, nor did it appear to hold true for the knockout strains measured.

This ease with which the baking yeasts sporulate in YPD may explain the vastly different trends of k_{io} in baking yeast strains compared to laboratory yeast strains. We investigated the possibility of differences in sporulation efficiency causing the change in k_{io}. When grown in sporulation media, we observed values of k_{io} in Fleischmann's baking strains similar to the stationary phase observed when grown in YPD, but we found that k_{io} decreases over 50% in the BY4743 strain grown in sporulation media. We will explore the possibility of using sporulated yeast as a model system in more detail in Chapter 3.

The second objective of this chapter was to understand how the presence of particular transmembrane proteins may be involved in the mechanism of water exchange across the growth curve. Four knockouts were selected to represent proteins that are potentially involved in water cotransport. The results from these studies suggests a significant level

of complexity to water exchange with respect to the relationship between growth and transmembrane proteins. This survey of knockouts demonstrate that water membrane-bound transporter proteins facilitate the exchange water across the cell membrane, however, the extent that each protein plays a role in water exchange appears to be dynamic and changes across a growth curve. Water exchange was steadily suppressed only in the case of the *Δpma1* mutant. This suggests water exchange kinetics are driven by the activity of the H^+ATP*ase* across the entire growth curve, but also indicates that the mechanism of secondary transport changes dynamically. The nature of transmembrane water exchange as it relates to metabolism and the H^+ATP*ase* will be explored in greater detail in Chapter 4. The decrease in k_{io} observed in the knockouts for *Δcch1* and *Δaqy2* correlate to the expression profiles of the respective genes previously reported in the literature.[27,28] Perhaps even more intriguingly, we observed a decrease in k_{io} across the growth curve of *Δpmr1*. This decrease demonstrates that steady state water regulation is sensitive to interruptions in lipid synthesis, and that intracellular defects can affect water exchange.

2.5 References

1. Zhang, Y., Poirier-Quinot, M., Springer, C. S. & Balschi, J. A. Active Trans-Plasma Membrane Water Cycling in Yeast Is Revealed by NMR. *Biophys. J.* **101**, 2833–2842 (2011).

2. Gray, J. V. *et al.* 'Sleeping beauty': quiescence in Saccharomyces cerevisiae. *Microbiol. Mol. Biol. Rev. MMBR* **68**, 187–206 (2004).

3. Olivares-Marin, I. K., González-Hernández, J. C., Regalado-Gonzalez, C. & Madrigal-Perez, L. A. Saccharomyces cerevisiae Exponential Growth Kinetics in Batch Culture to Analyze Respiratory and Fermentative Metabolism. *J. Vis. Exp. JoVE* (2018) doi:10.3791/58192.

4. Perez-Samper, G. *et al.* The Crabtree Effect Shapes the Saccharomyces cerevisiae Lag Phase during the Switch between Different Carbon Sources. *mBio* **9**, (2018).

5. Alberghina, L., Smeraldi, C., Ranzi, B. M. & Porro, D. Control by Nutrients of Growth and Cell Cycle Progression in Budding Yeast, Analyzed by Double-Tag Flow Cytometry. *J. Bacteriol.* **180**, 3864–3872 (1998).

6. Vermeersch, L. *et al.* On the duration of the microbial lag phase. *Curr. Genet.* **65**, 721–727 (2019).

7. Wegman, R. A. & Langejan, A. Instant dry yeast. (1994).

8. Porro, D., Vai, M., Vanoni, M., Alberghina, L. & Hatzis, C. Analysis and modeling of growing budding yeast populations at the single cell level. *Cytom. Part J. Int. Soc. Anal. Cytol.* **75**, 114–120 (2009).

9. Hagman, A., Säll, T., Compagno, C. & Piskur, J. Yeast "Make-Accumulate-Consume" Life Strategy Evolved as a Multi-Step Process That Predates the Whole Genome Duplication. *PLoS ONE* **8**, (2013).

10. Pfeiffer, T. & Morley, A. An evolutionary perspective on the Crabtree effect. *Front. Mol. Biosci.* **1**, (2014).

11. Pfeiffer, T., Schuster, S. & Bonhoeffer, S. Cooperation and competition in the evolution of ATP-producing pathways. *Science* **292**, 504–507 (2001).

12. Saccharomyces cerevisiae ethanol degradation. (https://pathway.yeastgenome.org/YEAST/NEW-IMAGE?type=PATHWAY&object=PWY3O-4300.

13. Benaroudj, N., Lee, D. H. & Goldberg, A. L. Trehalose accumulation during cellular stress protects cells and cellular proteins from damage by oxygen radicals. *J. Biol. Chem.* **276**, 24261–24267 (2001).

14. Silljé, H. H. W. *et al.* Function of Trehalose and Glycogen in Cell Cycle Progression and Cell Viability in Saccharomyces cerevisiae. *J. Bacteriol.* **181**, 396–400 (1999).

15. Neiman, A. M. Sporulation in the Budding Yeast Saccharomyces cerevisiae. *Genetics* **189**, 737–765 (2011).

16. Gerke, J. P., Chen, C. T. L. & Cohen, B. A. Natural Isolates of Saccharomyces cerevisiae Display Complex Genetic Variation in Sporulation Efficiency. *Genetics* **174**, 985–997 (2006).

17. Yeast Sporulation Medium. *Cold Spring Harb. Protoc.* **2017**, pdb.rec090076 (2017).

18. Neiman, A. M. Ascospore Formation in the Yeast Saccharomyces cerevisiae. *Microbiol. Mol. Biol. Rev.* **69**, 565–584 (2005).

19. Brachmann, C. B. *et al.* Designer deletion strains derived from Saccharomyces cerevisiae S288C: a useful set of strains and plasmids for PCR-mediated gene disruption and other applications. *Yeast Chichester Engl.* **14**, 115–132 (1998).

20. Saccharomyces Genome Database | SGD. https://www.yeastgenome.org/.

21. Tomar, P. *et al.* Sporulation Genes Associated with Sporulation Efficiency in Natural Isolates of Yeast. *PLOS ONE* **8**, e69765 (2013).

22. Coluccio, A. E., Rodriguez, R. K., Kernan, M. J. & Neiman, A. M. The Yeast Spore Wall Enables Spores to Survive Passage through the Digestive Tract of Drosophila. *PLoS ONE* **3**, (2008).

23. Kong, I. I., Turner, T. L., Kim, H., Kim, S. R. & Jin, Y.-S. Phenotypic evaluation and characterization of 21 industrial Saccharomyces cerevisiae yeast strains. *FEMS Yeast Res.* **18**, (2018).

24. Antebi, A. & Fink, G. R. The yeast Ca^{2+}-ATPase homologue, PMR1, is required for normal Golgi function and localizes in a novel Golgi-like distribution. *Mol. Biol. Cell* **3**, 633–654 (1992).

25. Sorin, A., Rosas, G. & Rao, R. PMR1, a Ca2+-ATPase in Yeast Golgi, Has Properties Distinct from Sarco/endoplasmic Reticulum and Plasma Membrane Calcium Pumps. *J. Biol. Chem.* **272**, 9895–9901 (1997).

26. Dürr, G. *et al.* The medial-Golgi Ion Pump Pmr1 Supplies the Yeast Secretory Pathway with Ca^{2+} and Mn^{2+} Required for Glycosylation, Sorting, and Endoplasmic Reticulum-Associated Protein Degradation. *Mol. Biol. Cell* **9**, 1149–1162 (1998).

27. Furukawa, K., Sidoux-Walter, F. & Hohmann, S. Expression of the yeast aquaporin Aqy2 affects cell surface properties under the control of osmoregulatory and morphogenic signalling pathways. *Mol. Microbiol.* **74**, 1272–1286 (2009).

28. Teng, J. *et al.* Hyperactive and hypoactive mutations in Cch1, a yeast homologue of the voltage-gated calcium-channel pore-forming subunit. *Microbiol. Read. Engl.* **159**, 970–979 (2013).

CHAPTER 3. THE EFFECTS OF TRANSMEMBRANE WATER EXCHANGE ON THE RELAXIVITY OF RESPONSIVE CONTRAST AGENTS

3.1 Introduction

Responsive MRI contrast agents are designed to alter their relaxivity in response to environmental stimuli, which can be used to signal the presence of a biomarker of interest. In this chapter, we will take a brief pause from the biological implications of water exchange to explore how changes to k_{io} may affect the quantification of a responsive MRI contrast agents.

Relaxivity

The relaxation catalyzing interaction between electron spin and nuclear spin was first characterized by Solomon, Bloembergen and Morgan (SBM) in the middle of the 20th century.[1,2] This description of the dipole-dipole interaction serves as the foundation for the field of MRI contrast agents. Longitudinal relaxivity (r_1) is a measure of a solute's ability to increase the longitudinal relaxation rate constant of water (R_1^w). Relaxivity is typically characterized in aqueous solutions and it is often used to evaluate the efficacy of gadolinium-based contrast agents (GBCAs). The R_1 of a solution containing distilled water and a GBCA can be described with equation 3.1.

$$R_1 = r_1[GBCA] + R_1^w \quad \textbf{(3.1)}$$

The R_1 of a solution is linearly related to the relaxivity (r_1) and concentration of a contrast agent, [GBCA]. It is important to note that the relaxivity of an agent is not directly measured, but through interpretation of the R_1 of water. At clinical field strengths (1.5-

3T) the relaxivity of most contrast agents ranges from 3.5 – 4.5 mM^{-1} s^{-1}. At 25 °C and 600 MHz the R_1^w of distilled water is about 0.3 s^{-1}.

The seven unpaired elections that occupy the 4f orbital of the Gd^{3+} ion are extraordinarily capable at inducing relaxation. Other paramagnetic ions, such as Fe^{2+} and Mn^{2+}, have been proposed as a potential base of an MRI contrast agents; however, because of their effectiveness, GBCAs remain the only agents currently used in clinics.[3–5] Although paramagnetic compounds are the focus of the field of MRI contrast agents many non-paramagnetic solutes, in particular macromolecules, can also have affect the R_1^w. The relaxivity a compound typically weakens as field strength increases.[6,7]

Improving contrast agents

Despite the widespread use of GBCAs in clinics today, there remains a substantial effort to improve the efficacy of contrast agents. There are three principal approaches to develop a more effective contrast agent. The first is through an improvement in the agent's inherent relaxivity. This is done through careful structural manipulation of the complex in order to change properties such as the rotational correlation rate and water residence lifetime.[8,9] Adjusting these parameters, which are outlined in SBM theory, can increase an agent's inherent relaxivity. The second approach is the development of a targeting vector that would associate (either covalently bonded or though hydrophobic interactions) with a specific biomarker of interest. In this case, contrast agent aggregation would reflect the presence of a biomarker which would then be visible in an image.[10,11]

The third approach is through responsive agents. Responsive GBCAs change their relaxivity in response to a biomarker of interest.[12–14] Many agents in the second approach can also overlap with the third approach. The relaxivity of targeted agents can change upon macromolecule binding, as binding to a large molecule greatly alters the rotational correlation rate.

Responsive agents typically exploit one of three physio-chemical parameters that are known to govern relaxivity. The rate of molecular tumbling ($1/\tau_R$); the rate of inner-sphere water exchange (k_{ex}); and the number of water molecules capable of occupying coordination sites on the metal ion (q) are all mechanisms to change relaxivity in response to a biomolecule or an environmental condition.[15,16] Of the three variables, changing the hydration number is by far the most common approach to the design of responsive agents. Changing q also has the added advantage that it is the least sensitive to changing magnetic field strength.

One example of this approach is a pH responsive agent reported in 2004.[17] At high pH GdNP-DO3A is a tetra-anionic ligand capable of occupying eight of the nine inner-sphere coordination sites of Gd^{3+}. The ninth coordination site is available for a labile water bond. When the pH is lowered, protonation of the nitrophenol group causes it to dissociate from the Gd^{3+} center opening up a second coordination site for water. This change in hydration state, q, from one bound water molecule to two bound water molecules causes a proportional increase in relaxivity (Fig. 3.1).

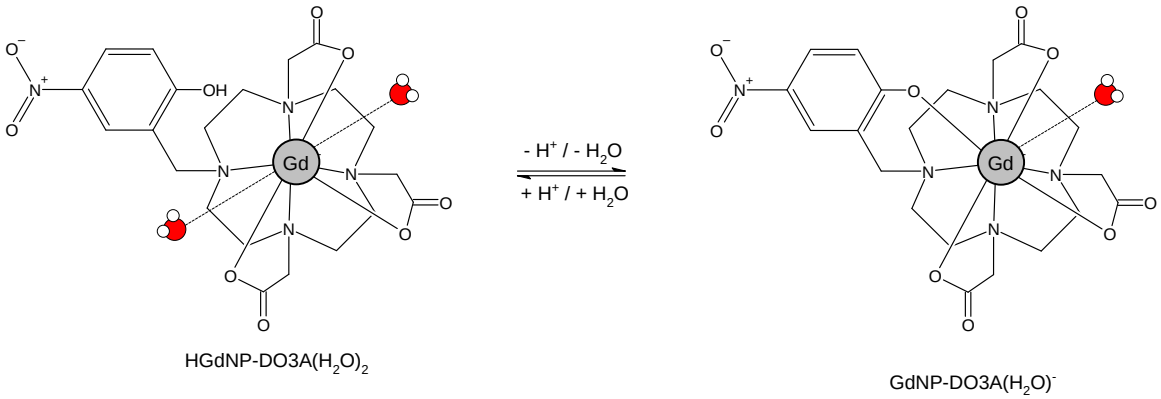

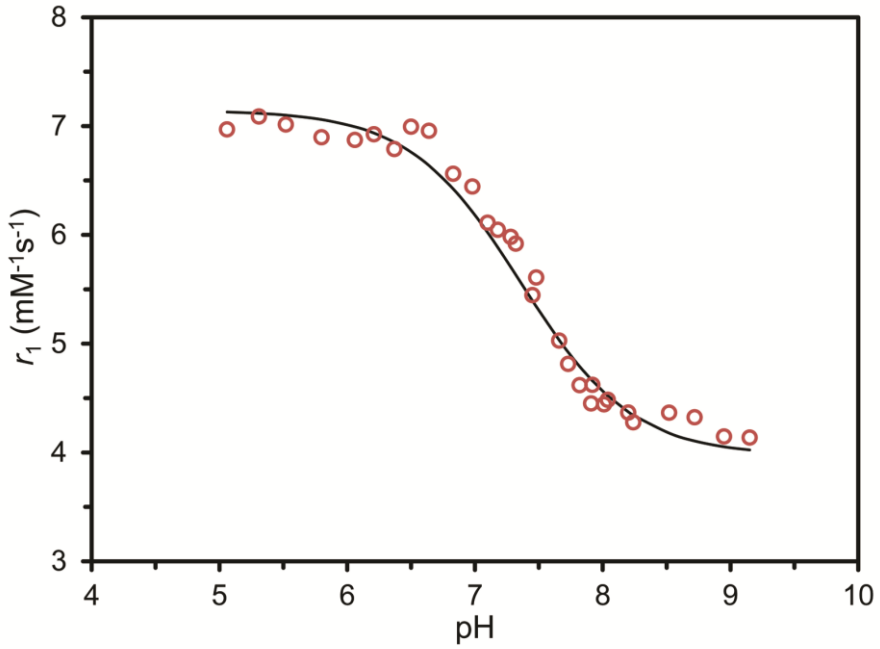

Figure 3.1 The relaxivity of GdNP-DO3A in aqueous solution at 298 K and 20 MHz exhibits a change from 4.0 $mM^{-1}s^{-1}$ at high pH to 7.1 $mM^{-1}s^{-1}$ at low pH. The change in relaxivity can be attributed to a change in the hydration number of the chelate that occurs when the nitrophenol ligand becomes protonated and dissociates from the Gd^{3+} center

In this example, the distribution of hydration numbers of the complex is affected by the presence of H^+ in solution. Because r_1 is proportional to q, accurate quantification of the

relaxivity would permit measurement of pH *in vivo*, which as a number of potential diagnostic applications; however, quantifying relaxivity in cell systems is complicated by the compartmentalization of water.

Contrast agents and relaxivity in cell systems

The relaxivity of a contrast agent is commonly expressed by the first term in Eqn. 3.2. This equation can be expanded to illustrate how relaxivity depends on the volume of the system.

$$r_1 = \frac{R_1 - R_1^{\mathrm{W}}}{[\mathrm{GBCA}]} = \frac{\Delta R_1 \cdot \mathrm{vol}}{\mathrm{mol}_{\mathrm{GBCA}}} \qquad \textbf{(3.2)}$$

The r_1 of a solute is a measure of the magnitude of difference in the measured R_1 with respect pure water (R_1^{w}) per unit concentration. In this formulation the units of relaxivity are $mM^{-1}s^{-1}$. But this situation can only be true in aqueous samples when the entire volume of the sample is filled with water. This is rarely the case *in vivo*, and, because the density of water is 1 gmL^{-1}, relaxivity is more properly represented by equation 3.

$$\mathrm{r}_1 = \frac{\Delta \mathrm{R}_1 \cdot \mathrm{mass\ H_2O\ obs}}{\mathrm{mol}_{\mathrm{GdL}}} \qquad \textbf{(3.3)}$$

In this more general formulation, the units of relaxivity are $kgmmol^{-1}s^{-1}$ (or in non-SI units $mmolal^{-1}s^{-1}$). It is only the case that $kgmmol^{-1}s^{-1}$ equals $mM^{-1}s^{-1}$ when the entire volume is occupied by water. *In vivo* $kgmmol^{-1}s^{-1}$ does not equal $mM^{-1}s^{-1}$ for two reasons. The first is that some part of the volume is displaced by cellular architecture, and the second is that the *in vivo* volume is compartmentalized by cell membranes. GBCAs are

strictly confined to the extracellular compartment and, because contrast agents are effective over a short distance (~6 – 7 Å), the contrast agent can only act on extracellular water. *In vivo*, 75 – 80 % of all water is located within the cell membrane, where it inaccessible to the contrast agent. This creates a scenario where the water available to the contrast agent is a function mass fraction of water in each compartment and the rate of exchange between them.

Using baker's yeast as a model for exchange

Understanding how compartmentalization may affect the observed relaxivity of a GBCA is essential to the accurate quantification of relaxivity. In Chapter 2, commercially available baking yeast strains were observed to decrease water exchange as the culture progressed through a growth curve. In this chapter, we will use the commercially available strain Fleischmann's baking yeast as a model system to probe the relationship between k_{io} and relaxivity.

Responsive model

The effect of a change in hydration state can be simulated by using the following agents: $GdDTPA^{2-}$ which has a hydration state of 1 (q = 1); and $GdTTHA^{3-}$ which has a hydration state of 0 (q = 0). Inner sphere water describes the water molecules bound to the metal and represents the significant portion of relaxivity. Although coordinated water molecules are typically the focus of discussions of relaxivity, non-coordinated water is also relaxed by the tumbling paramagnetic dipole of Gd^{3+}. $GdTTHA^{3-}$ interacts exclusively with non-cordinated water, while $GdDTPA^{2-}$ enhances the relaxation of water

through interactions with both coordinated and non-coordinated water molecules. Fig. 3.6 shows the nature of the water-GBCA interaction in the extracellular space.

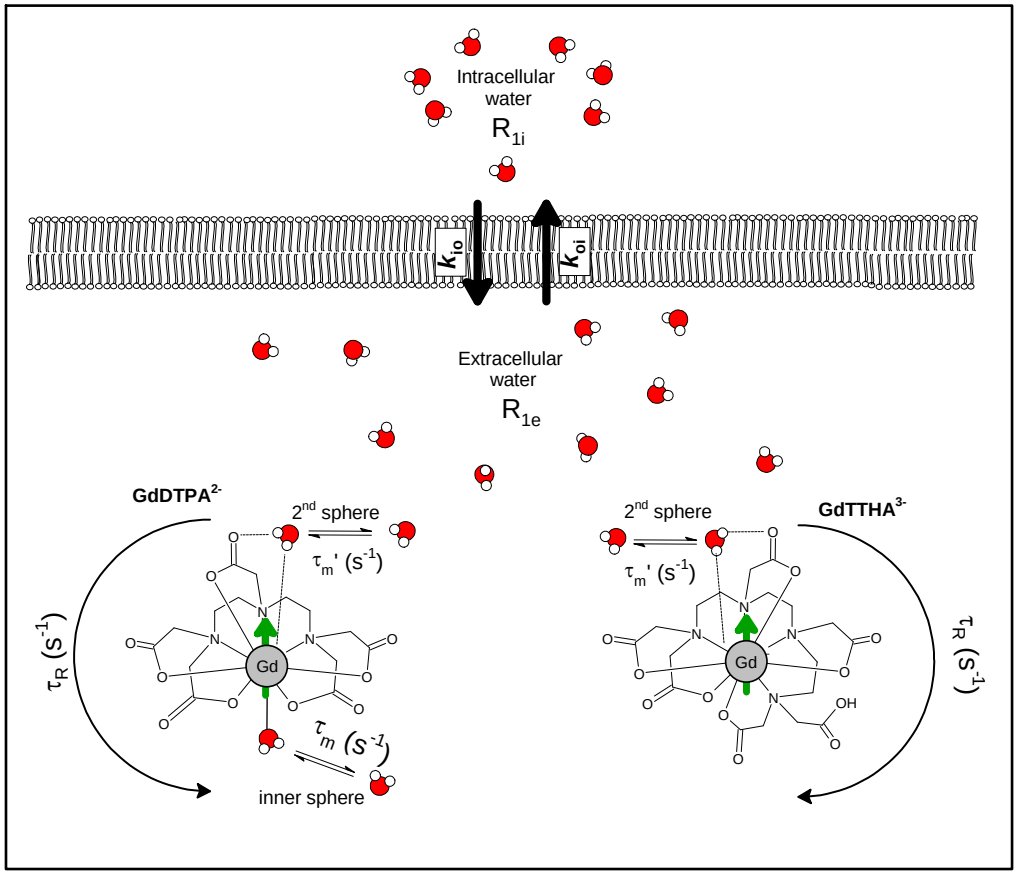

Figure 3.2 A schematic of the compartmentalization of water relaxation in cell systems containing GdDTPA^{2-} and GdTTHA^{2-}. The mean lifetime of the labile water Gd^{3+} bond is given by τ_m. The second-sphere interactions occur as a result of hydrogen bonding between passing water molecules and the carbonyls of the chelate which occurs on a lifetime of τ_m'. The rotational correlation time is given by τ_R. Figure adapted from Caravan et al.[19]

^{1}H nuclei on non-bound water are relaxed by the chelate tumbling which generates oscillations of the paramagnetic dipole. The relaxation catalyzing interaction with second

sphere water can account for around half of the relaxivity of a complex.[18] GBCAs tumble in solution at a rate which can be characterized by a rotational correlation time, τ_R. As they tumble, water is exchanged on and off any open coordination sites available on the Gd^{3+} ion.

3.2 Materials and Methods

Growth conditions

Pre-cultures of F. Baker's yeast (Fleischmann's active baking yeast, ATCC 7754, locally purchased) were grown overnight in complete media (YPD, Difco) before the culture flasks were inoculated into growth flasks. Strain was grown in triplicate using 300 mL of YPD in 500 mL flasks topped with aerated lids (Pyrex). The flasks were shaken vigorously to maintain thorough aeration for the duration of the experiment. Cell density was monitored using an optical density at 600 nm wavelength using a Bio-Rad UV-vis spectrometer. The exponentially growing cells were taken when the OD_{600} was greater than 0.4 and 0.7 (arbitrary units) after a 1:30 dilution. The stationary phase was collected after 7 days.

Relaxivity measurements in cell pellets

During the stationary and exponential growth phases, 15 mL aliquots of culture from three batch cultures were collected and centrifuged. The supernatant from each aliquot was removed and combined with the $GdDTPA^{2-}$ or $GdTTHA^{3-}$. Three samples were prepared for each of the following extracellular concentrations of GBCA: 0.125mM,

0.25mM and 0.5mM. Each cell sample was washed with contrast agent (3 × 1.0 mL) and resuspended in heavy walled NMR tube. The cells were then pelleted in the NMR tube using a centrifuge at 900 g for two minutes. Contrast free samples were washed and resuspended in their native supernatant before they were pelleted and measured. The longitudinal relaxation rate constant (R_1) of the cell pellets was measured on a Bruker Avance III 600 MHz spectrometer using the inversion recovery pulse sequence after acclimatizing for 5 mins to the internal probe temperature which was set to 25 °C. Each inversion recovery measurement contained 4 scans of 32 points with a variable delay ranging from 1 ms to 10 s and a relaxation delay of 10.5 s. The values for R_1 were obtained by integrating the water peak in the Fourier transformed FID for each delay time using Bruker's Topspin© data processing software.

Saturation recovery to measure inherent relaxivity in pure water

At 600 MHz, the inversion recovery pulse sequence cannot be used to accurately measure the inherent relaxivity of a contrast agent when dissolved in pure water. This is due to an effect known as radiation damping, which can artificially increase R_1.[23,24] Radiation damping is not an issue in the cell pellet samples due to the heterogeneity the pellet, which increases R_2 sufficiently to minimize the effects of radiation damping.

The saturation recovery pulse sequence ('satrec' on Bruker's TopSpin©) was used for the relaxivity measurements of the aqueous samples to avoid radiation damping. These samples were measured at 1.0, 3.0 and 5.0 mM concentrations of GBCA at 25°C. Each saturation recovery curve consisted of 16 points each made up of 4 scans taken with a variable delay time ranging from 1 ms to 600 ms. Saturation pulse was set to 4.7 ppm

with a pulse power of 3.187 x 10^{-5} W and pulse length was adjusted to be 1.5× the expected T_1 ($1/R_1$) of the sample (600 ms – 1.2 s).

3.3 Results

Growth phase and k_{io}

Batch cultures of baking yeast can provide reproducible and variable native exchange environments with which the effects of k_{io} on r_1 can be observed. The values of k_{io} observed in exponential phase cultures (~3.5 s^{-1}) and stationary phase cultures (~1.5 s^{-1}) of the baking yeast, Fleischmann's baking yeast, demonstrate a range that is similar to those reported from measurements *in vivo*.[20–22]

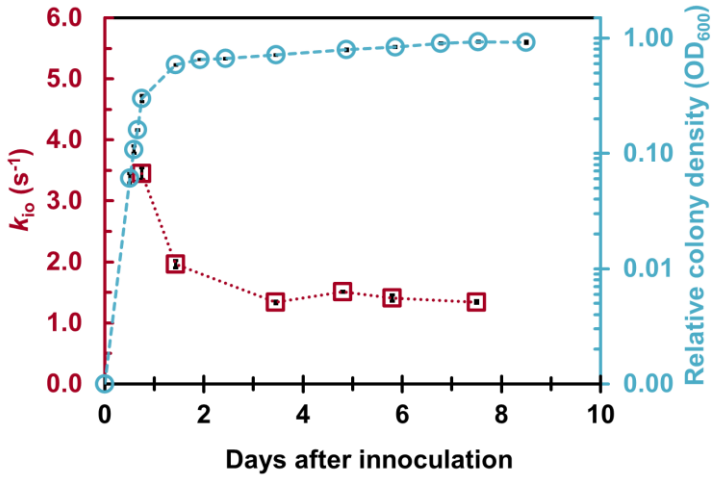

Figure 3.3 Batch cultivation of the commercially available baking strain, Fleischmann's baking yeast (F. Baker's) provides a platform with which water exchange kinetics can be easily probed. Values for transmembrane water efflux, k_{io}, measured in the exponential growth phase are more than double the values measured in the stationary growth phase.

Intracellular water mole fraction

The intracellular water mole fraction, p_i, of the yeast pellet was measured at a GBCA concentration of 10 mM using 2SX fitting model. The average p_i was plotted against the growth phase to approximate a total volume based extracellular concentration.

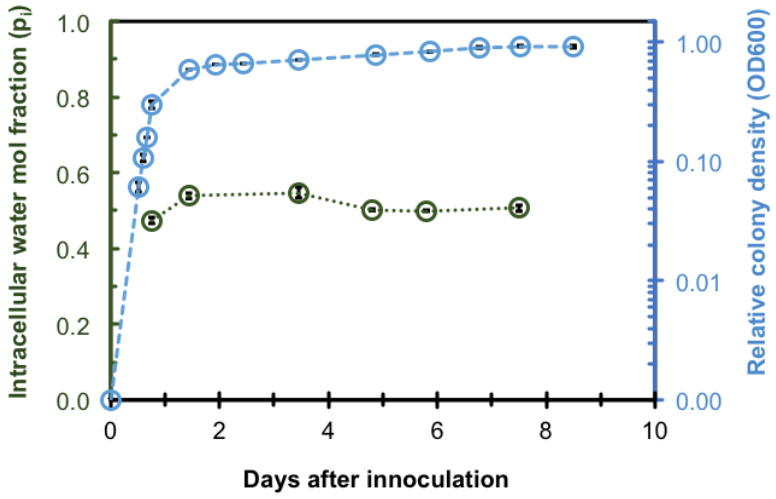

Figure 3.4 The intracellular water mole fraction measured from cells pellets prepared with 10mM contrast agent and modeled in the SXR (as demonstrated in Chapter 2). Each data point represents the average of a series of biological triplicates, and the error bars represent one standard deviation above and below the average.

Relaxivity in two exchange regimes

The rate of water exchange in the commercially available yeast strain, Fleischmann's Active baking yeast (F. Baker's), was observed to change upon the maturation of the culture. To study the effects of this change membrane exchange on relaxivity, cells were collected during the exponential and stationary growth phases when the difference in k_{io} was greatest, and doped with GBCA in the extracellular space at concentrations of 0.1

mM, 0.25 mM and 0.50 mM. The two chelates $GdDTPA^{2-}$ and $GdTTHA^{3-}$ were selected to simulate the extremes of a responsive contrast agent that changes the value of q upon response to a hypothetical marker of interest. The two chelates GdDTPA and GdDTPA have different values for r_1 in distilled water due to their differences in hydration state (q = 1 versus q = 0). The relaxivity of both GBCAs was calculated in a range of conditions by taking the slopes from the $[Gd^{3+}]$ vs R_1 plots in Fig 3.5. The inherent relaxivity for each GBCA was characterized in distilled water, and is shown as the dashed lines in Fig. 3.5. Observed relaxivity, which is shown as the open circles and diamonds in Fig. 3.5 was calculated in the cell pellets where the GBCA is restricted to the extracellular water volume. In these pellets, the extracellular water makes up only about half of the total water volume. This can be seen from the fittings of p_i in Fig. 3.4.

Low concentrations of GBCA were used to ensure that the measured relaxation remained mono-exponential over the course of the inversion recovery measurement. Each individual R_1 measurement was made in biological triplicate, and the R_1 of each concentration was found from plotting the average of these values. Error bars were included to represent the standard deviation between the three measurements. The relaxivity was calculated from a linear regression and the fits are summarized in Table 3.1. The observed relaxivity for both contrast agents appeared to change decrease when k_{io} decreased. The magnitude of change between the exponential and stationary phase was greater in $GdDTPA^{2-}$ than in $GdTTHA^{3-}$.

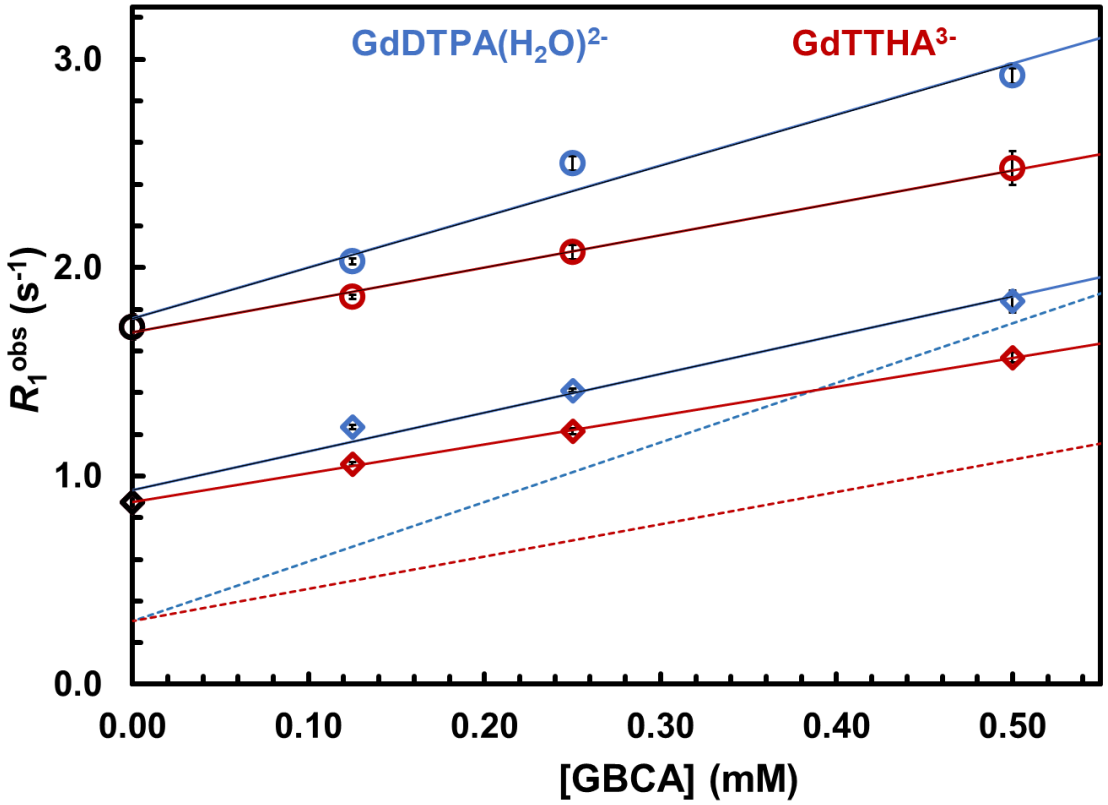

Figure 3.5 The longitudinal relaxation rate constant (R_1) was measurements at three concentrations of $GdDTPA^{2-}$ (blue) or $GdTTHA^{3-}$ (red) in suspensions of yeast cells in the exponential (circles) and stationary (diamonds) growth. The water exchange rate, k_{io}, is ~3.5 s^{-1} in the exponential phase and ~1.5 s^{-1} in the stationary phase. The inherent relaxivity of $GdDTPA^{2-}$ and $GdTTHA^{3-}$ in aqueous solution is given by the blue and red dashed line respectively. The concentration of GBCA reflects the concentration of the solution used to wash the pellets. Each point represents an average of biological triplicates. Error bars in R_1 represent one standard deviation above and below the average.

Table 3.1 Intrinsic relaxivity and observed relaxivity

	Hydration number (*q*)	**k_{io} (s^{-1})**	**Intrinsic r_1 ($mM^{-1}\,s^{-1}$)**	**Observed r_1 ($mM^{-1}\,s^{-1}$)**	**R^2**
$GdDTPA^{2-}$	1	~3.5	3.12	2.44	0.972
$GdTTHA^{3-}$	0	~3.5	2.03	1.55	0.996
$GdDTPA^{2-}$	1	~1.5	3.12	1.86	0.981
$GdTTHA^{3-}$	0	~1.5	2.03	1.37	0.999

The relaxivity (r_1) a GBCA is measured from the slope of the R_1 *vs* [Gd^{3+}] plots shown in Fig. 3.4. The observed relaxivity of $GdDTPA^{2-}$ and $GdTTHA^{3-}$ was measured in yeast pellets at 600 MHz and 25 °C and compared to the inherent values measured in fresh medium under the same conditions. The relaxivities were measured in both the exponential (k_{io} ~ 3.5 s^{-1}) and stationary (k_{io} ~ 1.5 s^{-1}).

3.4 Discussion

Inherent and observed relaxation

In diffuse cell systems, where water exchange across the cell membrane is sufficiently rapid, the observed relaxivity of a GBCA approaches the inherent relaxivity. When water exchange across the membrane is more limited, as in the case of stationary phase yeast

cells, the observed relaxivity of the contrast agent decreases. The effect of k_{io} on relaxivity is apparent in the changes to the slope of R_1 *vs* [Gd^{3+}]. Although changes to each individual slope is subtle, a comparison between the slopes of the red and blue lines, (which represent the various conditions of $GdTTHA^{3-}$ and $GdDPTA^{3-}$, respectively) reveals the effect of k_{io} on relaxivity. In the inherent relaxivity measurements (red and blue dashed lines), the difference between the relaxivity of the two contrast agents is greatest. This measurement was taken in the absence of compartmentalization. In stationary phase cell pellets (diamonds) where water exchange is the slowest, the difference in relaxivity between the two contrast agents is the smallest. In the exponential phase where exchange is fast (circles), the relaxivities of the $GdDTPA^{2-}$ and $GdTTHA^{3-}$ are closer to the respective inherent values.

It is important to make the distinction that there are no inherent changes to the relaxivity of either GBCA between the exponential and stationary phase and that the observed relaxivity appears to decrease as a function of exchange. The effect of water exchange on observed relaxivity appears to be more significant in chelates with a higher inherent relaxivity. The magnitude of change in observed relaxivity due to the changes in membrane water exchange is greater in $GdDTPA^{2-}$ than in $GdTTHA^{3-}$.

The change in observed relaxivity of $GdDTPA^{2-}$ between the exponential and stationary growth phases is comparable to the change in inherent relaxivity observed between $GdDTPA^{2-}$ and $GdTTHA^{3-}$. The changes to relaxivity seen in this work are also comparable to the changes in inherent relaxivity in many other responsive agents reported in the literature.[15] The difference in the hydration state between $GdDTPA^{2-}$ and

$GdTTHA^{3-}$ (q = 1 and q = 0) represents an absolute maximum response that could be garnered for an agent of this type. This implies that there is potential for k_{io} to be even more confounding in a true responsive agent than in our $GdDTPA^{2-}$/$GdTTHA^{3-}$ model. A responsive agent designed to change hydration number would likely feature a distribution of 0 and 1 hydration numbers *in vivo*. For example, take the chelate GdNP-DO3A. A change in pH from 5.5 to 9.0 results in a change in inherent relaxivity equal to about 3 mM^{-1} s^{-1}. However, a change from a pH of 7 to a pH of 5 garners a response of only ~1.5 mM^{-1} s^{-1}. The values for k_{io} between exponentially and stationary phase cells are similar to values measured in a number of pathologies *in vivo*.[20–22] This highlights the importance of considering k_{io} when quantifying relaxivity in cell systems.

Extracellular concentration vs total concentration

The measurements of observed relaxivity from Table 3.1 were calculated using the concentration of GBCA in the extracellular wash solution. In the cell pellets, the intracellular water volume fraction, p_i, was found to remain largely static between 0.47 and 0.50 across the growth curve. Almost half of the water in the system is inside the membrane, however, the measurements of observed relaxivity are not reflective of this. A volume correction alone still leads to erroneously high calculations of relaxivity.

Shutter speed and changes to r_1

One consequence of the relationship between observed relaxivity and k_{io} is that it indicates the relaxation system of the pellet is not beyond fast exchange limit (FXL). When the membrane k_{io} is around 3.5 s^{-1}, the observed relaxivity approaches the intrinsic

relaxivity of the chelate. This suggests that a membrane exchange rate of 3.5 s^{-1} may be close to the fast exchange limit (FXL) which describes a diffuse system. When exchange is slowed down, the intracellular water is less likely to be relaxed by the GBCA in the extracellular compartment. This leads to a decrease in observed relaxivity.

As discussed in the introductory chapter, the fast exchange limit shutter speed condition occurs when:

$$|R_{1e}-R_{1i}| << k_{ex} \quad \textbf{(3.4)}$$

Where the k_{ex} in the cell system is much greater than the shutter-speed. In such conditions, the R_1 is defined as:

$$R_1 = p_i R_{1i} + p_e R_{1e} \quad \textbf{(3.5)}$$

Where p_i and p_e are the intracellular and extracellular water volume fractions and R_{1i} and R_{1e} are the intracellular and extracellular relaxation rate constants, respectively. Compartmentalized systems in the FXL behave like a diffuse, homogeneous solution. R_1 in a cell system is therefore, the mass balanced sum of the relaxation rate constants of the two compartments (Eqn. 3.5). If the membrane exchange were to be far beyond the FXL in the yeast pellets, the observed relaxivity of the contrast agents would remain unaffected by a change in membrane exchange. Since a change in the observed relaxivity appears to change due to a change k_{io} and that the relaxation measured exhibits mono-exponential behavior, we can assume that these pellets are outside the FXL and in the fast

exchange regime (FXR). Mono-exponential relaxation in the FXR can be modeled with Eqn. 3.6.

$$R_1(obs) = \frac{1}{2}\,[R_{1i} + R_{1e} + \mathrm{k}_{io} + \mathrm{k}_{oi}] - \frac{1}{2}\{[(R_{1i} - R_{1e}) + (\mathrm{k}_{io} - \mathrm{k}_{oi})]^2 + 4(\mathrm{k}_{io}\mathrm{k}_{oi})\}^{1/2} \quad \textbf{(3.6)}$$

R_1 in the absence of GBCA

One interesting observation is that the y-intercept of the relaxivity measurements changes between the stationary and exponential growth phase. The R_1 of the yeast pellet measured in the absence of GBCA was found to be lower in the stationary growth phase than in the exponential growth phase. In addition to slowing water exchange, the further compartmentalization of the intracellular environment that occurs upon culture maturation also alters the contrast free R_1 of a cell pellet. The R_1 of the supernatant does not appreciably change, which implies that the change in R_1 of the pellet is due to a change in the relaxation rate constant of intracellular water R_{1i}.

To understand the dynamics of intracellular relaxation, it is useful to imagine a theoretically isolated intracellular water population. If the intracellular water compartment is well-mixed, meaning that the time scale of diffusion is significantly greater than the water protein interaction a single relaxation signal is generated which can be described with Eqn. 3.7.

$$R_{1i} = r_{mm}[MM] + R_1^{water} \quad \textbf{(3.7)}$$

Where r_{mm}[MM] represents the sum of dipole interactions between the concentration of macromolecules [MM] and their averaged relaxivity r_{mm}. The magnitude of this dipole-

dipole relaxation interaction is largely influenced by the field strength of the external magnet. In systems where the diffusion of water is sufficiently slow, such as frozen and thawed agarose gel, the water bound to protein can be distinguished from bulk water, but in more typical conditions water appears as one signal.[25] The value of R_{1i} is governed by the interaction between water and intracellular macromolecules, r_{mm}[MM].

The intrinsic values for R_{1i} can be modeled between the stationary and exponential growth phases using Eqn. 3.7, if we assume that the pellets are in the FXR. This exercise reveals that that k_{io} alone cannot fully account for the changes in R_1 observed in the absence of contrast agent. There are changes to the inherent R_{1i} that also occur in addition to the change in exchange rate. When modeling R_{1i} in the two growth phases using the FXR equation, we find that the intrinsic R_{1i} changes over the growth phase from 4.01 s^{-1} in the exponential growth phase to 1.68 s^{-1} in the stationary growth phase. R_{1i} decreases nearly 60%, which presents a significant change to the quantity r_{mm}[MM] in the stationary phase.

It is difficult to say definitively if the changes in baking yeast are due to the relaxivity of macromolecules, r_{mm}, or to a change in their concentration, [MM]. There does not appear to be a significant change to the intracellular water volume fraction p_i, however this does not reveal much detail about the compartment dynamics. These experiments were conducted at high fields with the goal of minimizing the effect of macromolecular content on relaxivity, however it appears that the R_1 of the cell pellets is susceptible to biological changes within the cell even at 600 MHz. Field cycling relaxometry, where r_1

is measured across many field strengths, would offer additional insight into how intracellular water changes across the growth curve of baking yeast.

Limitations

Although there are many advantages to using yeast as a model system for exchange, there are also several limitations that may affect the translation of these results. The intracellular water volume fraction, p_i, of the yeast pellet prepared with these methods is consistently around 0.47-0.50. As previously stated, *in vivo,* p_i is ranges between 0.75 - 0.8 depending on the tissue type. The effect of k_{io} on relaxivity may be magnified *in vivo* due to the increased intracellular volume fraction. The extracellular contrast agent is evenly distributed in a yeast pellet, whereas *in vivo* tissue it is far more irregular. Finally, another potentially consequential difference between relaxivity measurements *in vivo* versus *in vitro* is the native shutter-speed, or the absolute difference between the intracellular R_1 (R_{1i}) and the extracellular R_1 (R_{1e}). The shutter-speed is greater in the yeast pellet than in tissue because of the lack of relaxation catalyzing extracellular macromolecules that are present in the extracellular water *in vivo*, but largely absent in cell culture media.

3.4 Conclusions

Currently, clinical contrast enhanced MRI scans are entirely qualitative. The addition of quantification into MRI scans would be beneficial to both diagnostics and therapy evaluation. The chemistry and design of responsive chelates promises to increase the

diagnostic power of MRI, however the quantification of the response of these contrast agents is not straightforward. In this chapter, we have demonstrated that transmembrane water exchange can affect observed relaxivity of a contrast agent using commercially available baking yeast grown in batch culture to model exchange. In Chapter 2, we reported that Fleischmann's active dry yeast (F. Baker's) undergoes a >50% decrease in k_{io} between the exponential and stationary growth phases. The relaxivity of two chelates, $GdTTHA^{3-}$ and $GdDTPA^{2-}$, was measured during periods of rapid exchange ($k_{io} \sim 3.5\ s^{-1}$) and in slow exchange ($k_{io} \sim 1.5\ s^{-1}$) to simulate a change relaxivity that would occur through a change in hydration state. We found that a change in k_{io} can influence the observed relaxivity. The effect can appear similar to a change in hydration state and therefore may present a confounding variable in any attempt to quantify the relaxivity of contrast agents outside of aqueous or single compartment systems.

These changes to relaxivity are not caused by any inherent changes to the dynamics of the contrast agent, but instead by transmembrane water exchange, which affects the amount of water available to the contrast agent. The effect of k_{io} on relaxivity may ultimately lead to erroneous assignments of biological conditions if left unaccounted for How to accurately account for water exchange in responsive agents *in vivo* is another challenge altogether. A simple volume correction using the intracellular water volume fraction does not adequately address the disparities between observed and inherent relaxivity measurements. It is clear that a thorough understanding of the NMR shutter-speed regime is integral to the accurate interpretation of relaxivity in compartmentalized systems.

3.5 References

1. Solomon, I. Relaxation Processes in a System of Two Spins. *Phys. Rev.* **99**, 559–565 (1955).

2. Bloembergen, N. & Morgan, L. O. Proton Relaxation Times in Paramagnetic Solutions. Effects of Electron Spin Relaxation. *J. Chem. Phys.* **34**, 842–850 (1961).

3. Zareei, L. *et al.* A New Potential Contrast Agent for Magnetic Resonance Imaging: Iron Oxide-4A Nanocomposite. *J. Biomed. Phys. Eng.* **9**, 211–216 (2019).

4. Exceedingly small iron oxide nanoparticles as positive MRI contrast agents | PNAS. https://www.pnas.org/content/114/9/2325.

5. Pan, D., Schmieder, A. H., Wickline, S. A. & Lanza, G. M. Manganese-based MRI contrast agents: past, present and future. *Tetrahedron* **67**, 8431–8444 (2011).

6. Rooney, W. D. *et al.* Magnetic field and tissue dependencies of human brain longitudinal 1H2O relaxation in vivo. *Magn. Reson. Med.* **57**, 308–318 (2007).

7. Leone, L., Ferrauto, G., Cossi, M., Botta, M. & Tei, L. Optimizing the Relaxivity of MRI Probes at High Magnetic Field Strengths With Binuclear GdIII Complexes. *Front. Chem.* **6**, (2018).

8. Payne, K. Investigations into the Effects of Water Exchange and the Structure of Lanthanide Chelates. *Diss. Theses* (2016) doi:10.15760/etd.3275.

9. Jacques, V. *et al.* High relaxivity MRI contrast agents part 2: Optimization of inner- and second-sphere relaxivity. *Invest. Radiol.* **45**, 613–624 (2010).

10. Rust, L., Payne, K. M., Carniato, F., Botta, M. & Woods, M. Differences in the Relaxometric Properties of Regioisomeric Benzyl-DOTA Bifunctional Chelators: Implications for Molecular Imaging. *Bioconjug. Chem.* **30**, 1530–1538 (2019).

11. Morawski, A. M., Lanza, G. A. & Wickline, S. A. Targeted contrast agents for magnetic resonance imaging and ultrasound. *Curr. Opin. Biotechnol.* **16**, 89–92 (2005).

12. Woods, M., Zhang, S., Ebron, V. H. & Sherry, A. D. pH-Sensitive Modulation of the Second Hydration Sphere in Lanthanide(III) Tetraamide–DOTA Complexes: A

Novel Approach to Smart MR Contrast Media. *Chem. – Eur. J.* **9**, 4634–4640 (2003).

13. Davies, G.-L., Kramberger, I. & Davis, J. J. Environmentally responsive MRI contrast agents. *Chem. Commun. Camb. Engl.* **49**, 9704–9721 (2013).

14. Yoo, B. & Pagel, M. D. An overview of responsive MRI contrast agents for molecular imaging. *Front. Biosci. J. Virtual Libr.* **13**, 1733–1752 (2008).

15. Hingorani, D. V., Bernstein, A. S. & Pagel, M. D. A review of responsive MRI contrast agents: 2005–2014. *Contrast Media Mol. Imaging* **10**, 245–265 (2015).

16. Lohrke, J. *et al.* 25 Years of Contrast-Enhanced MRI: Developments, Current Challenges and Future Perspectives. *Adv. Ther.* **33**, 1–28 (2016).

17. Woods, M. *et al.* Synthesis, relaxometric and photophysical properties of a new pH-responsive MRI contrast agent: the effect of other ligating groups on dissociation of a p-nitrophenolic pendant arm. *J. Am. Chem. Soc.* **126**, 9248–9256 (2004).

18. Wahsner, J., Gale, E. M., Rodríguez-Rodríguez, A. & Caravan, P. Chemistry of MRI Contrast Agents: Current Challenges and New Frontiers. *Chem. Rev.* **119**, 957–1057 (2019).

19. Caravan, P., Farrar, C. T., Frullano, L. & Uppal, R. Influence of molecular parameters and increasing magnetic field strength on relaxivity of gadolinium- and manganese-based T1 contrast agents. *Contrast Media Mol. Imaging* **4**, 89–100 (2009).

20. Landis, C. S. *et al.* Equilibrium transcytolemmal water-exchange kinetics in skeletal muscle in vivo. 12.

21. Springer, C. S. *et al.* Intratumor mapping of intracellular water lifetime: metabolic images of breast cancer? *Nmr Biomed.* **27**, 760–773 (2014).

22. Li, X. *et al.* Cell Membrane Water Exchange Effects in Prostate DCE-MRI. *J. Magn. Reson. San Diego Calif 1997* **218**, 77–85 (2012).

23. Mao, X., Guo, J. & Ye, C. Radiation damping effects on spin—lattice relaxation time measurements. *Chem. Phys. Lett.* **222**, 417–421 (1994).

24. Krishnan, V. V. & Murali, N. Radiation damping in modern NMR experiments: Progress and challenges. *Prog. Nucl. Magn. Reson. Spectrosc.* **68**, 41–57 (2013).

25. Hills, B. P., Takacs, S. F. & Belton, P. S. The effects of proteins on the proton N.M.R. transverse relaxation time of water. *Mol. Phys.* **67**, 919–937 (1989).

CHAPTER 4. STEADY-STATE TRANSMEMBRANE WATER EXCHANGE IN GLUCOSE LIMITED CHEMOSTAT CULTURES OF *S. CEREVISIAE*

4.1 Introduction

The natural environment of wild yeasts (e.g., the juice of a fallen fruit) is moderately acidic. Yeast cells take advantage of low extracellular pH by utilizing a pH gradient to couple the transport of nutrients with the transport of protons.[1] The pump responsible for maintaining the membrane gradient across yeast cell membranes is the H^+ATP*ase* (encoded by the gene *pma1*).[2] In Chapter 2, the heterozygous knockout of *pma1,* was observed to depress values of k_{io} across the growth curve of batch cultivated yeast colonies. Similar correlations between k_{io} and ATP driven transport have been made across a range of cell types.[3,4] These observations have led to the active water cycling hypothesis which posits that k_{io} can be used to measure the activity of ATP driven pumps. In this chapter, we explore the relationship between k_{io}, glucose metabolism and H^+ATP*ase* using glucose limited chemostats.

Chemostat cultivation of Saccharomyces cerevisiae

Chemostats were developed independently by Monod and Novick and Szilard in the late 1950's as a method to continuously grow microbes.[5,6] Continuous culture systems have been critical to our understanding of how physiology changes with rates of growth and metabolism.[7,8] Chemostats operate by pumping fresh nutrients into the culture vessel at a set flow rate, while simultaneously ejecting both biomass and spent nutrients at an equal

flow rate, thereby maintaining a constant volume. A steady-state of growth within the chemostat can be achieved when the culture strikes a balance between dilution rate (D) and culture growth rate (u). This results in an environment where the culture biomass and metabolic profile are also in the steady-state. A steady-state can be achieved so long as the dilution rate is slower than the conditional maximum growth rate of the culture (u_{max}). Cultures grow to steady state typically after 5 – 10 volume changes.

Commercially available chemostat systems are quite elaborate and can cost upwards of $40,000. These systems are equipped with a wide range of sensors used to monitor various aspects of the culture. Dunham and coworkers at the University of Washington published an open-source schematic for a homemade chemostat.[9] Although the homemade chemostats are not equipped with many of the sensors that may be available on commercially available systems, they provide a cost-effective platform to study continuous yeast cultivation using commonly available laboratory equipment. The chemostat system outlined used in this work is quite simple, and a schematic is shown in Fig. 4.1.

The composition of the media fed into the chemostat has a significant effect on the culture. Chemostat media is contains an excess concentration of all nutrients with the exception of the limiting nutrient. The limiting nutrient is entirely consumed by the culture and determines the density of the culture and, by extension, u_{max}. The biomass yield (Y) is governed by equation 4.1, where the C_R is the concentration of the limiting nutrient in the fresh media, C_B is the concentration of biomass in the culture and C_S is the residual concentration of the limiting substrate in the culture.[10]

$$Y = \frac{C_B}{C_R - C_S} \quad \textbf{(4.1)}$$

The dilution rate (D) is the ratio of the flow rate to the culture volume (Eqn. 4.2). Maximum flow rates rarely exceed 0.5 hr^{-1}. The inverse of the flow rate is the time that it takes the culture to undergo one volume turnover.

$$D = \frac{flow\ rate}{culture\ volume} \quad \textbf{(4.2)}$$

The steady-state of a chemostat culture is defined as the condition where the culture growth rate, μ, is equal to the dilution rate, D. In this condition, μ is equal to the quantity defined by Eqn. 4.3 where K_s is the affinity constant for growth on the limiting nutrient.

$$\mu = D = \frac{\mu_{max} C_S}{K_S + C_S} \quad \textbf{(4.3)}$$

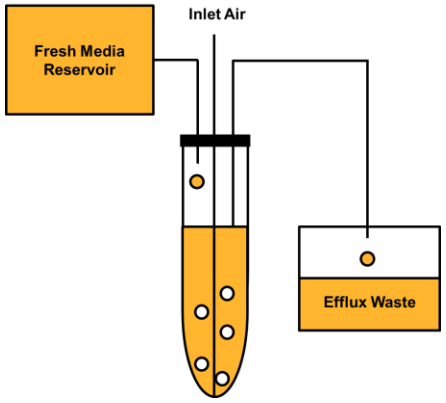

Figure 4.1 Chemostats allow for steady state cultivation of yeast. In this steady state, the growth rate, population and metabolic flux of the culture remains constant. Chemostats operate by continuously diluting the colony with fresh media while excess culture is continuously expelled to hold a constant volume. The chemostats utilize the flow of sterile air to ensure the culture is well mixed as well as providing positive pressure to power the efflux of culture.

The Crabtree effect in chemostat cultures

The Crabtree effect can be readily observed in glucose limited chemostats.[11] At low concentrations of glucose, the culture completely oxidizes any available glucose in the media and produces little to no ethanol. As the concentration of glucose increases beyond a critical point, the culture switches from exclusively respiration to a combination of respiration and fermentation. This switch allows the cells to consume glucose more rapidly. Metabolic efficiency, in terms of biomass produced per gram of glucose consumed is no longer a priority in fermenting cultures, and the switch to fermentation leads to a dramatic decrease in biomass yield of the culture.[11]

Glucose signaling and transport

The HXT (**H**e**X**ose **T**ransport) family of membrane channels are the primary mechanism of glucose uptake in yeast.[12,13] The transport of glucose through the HXT proteins occurs through facilitated diffusion. Sugar uptake and phosphorylation (the first step in glycolysis) are tightly coupled. This results in very little non-phosphorylated glucose present in the cytosol.[10] The rapid phosphorylation of glucose likely helps to maintain the glucose concentration difference between the cytosol and the extracellular space which drives glucose uptake. The HXT proteins have varying degrees of affinities toward glucose.

One of the major pathways regulating which transporter is expressed are the signaling proteins RGT2 and SNF3.[14,15] While RGT2 and SNF3 resemble HXT transporters, they do not transport glucose. Instead, they operate as sensors which help the cell detect the

extracellular glucose content and adapt the internal machinery accordingly.[16,17] The membrane-bound proteins SNF3 and RGT2 undergo conformational changes upon sensing glucose which allows them to bind the intracellular glucose repressing proteins MIG1, MTH1 and STD1.[18,19] Fig. 4.2 depicts the relationship between glucose detection and HXT expression. This example only includes HXTs 1-4, but there have been more than 17 HXT transporters identified in yeast which have varying affinities to glucose.[20]

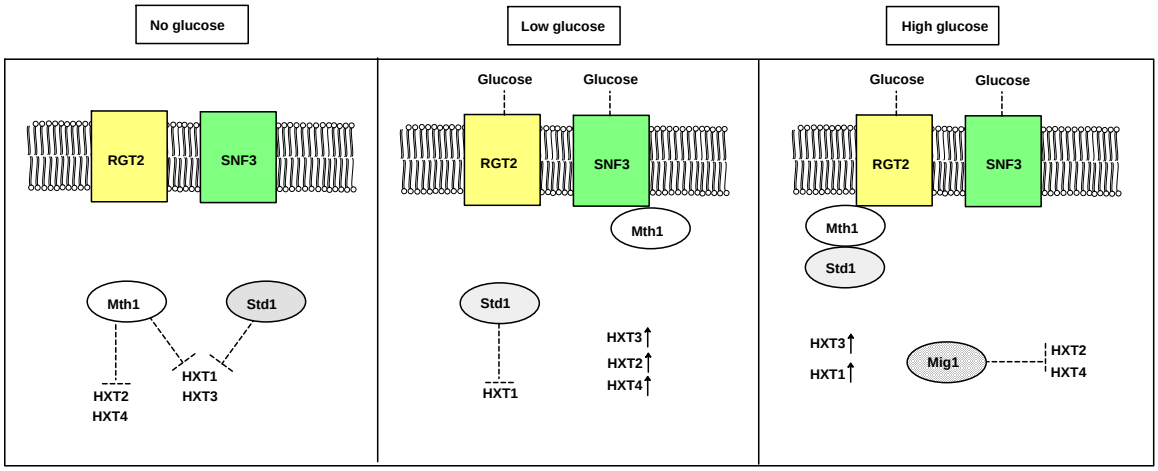

Figure 4.2 The relationship between the glucose sensors, RGT2 and SNF3 and the expression of HXT glucose transporters demonstrates an ability for the yeast to situationally express high and low affinity HXT transporters depending on the availability of extracellular glucose. Signaling is dependent on the conformational changes that occur to SNF3 and RGT2 upon their interaction with glucose. These conformational changes allow for the linkage of Mth1 onto SNF3 or Mth1 and Std1 onto RGT2 depending on the extracellular glucose concentration.

Pma1 and glucose metabolism

The transcription of the gene *pma1* is tied to glucose metabolism.[21] Sugars metabolized by the glycolytic pathway, such as glucose, fructose and mannose, lead to H^+ATP*ase*

activity while non-metabolized glucose analogues such as deoxyglucose do not.[22] Fig. 4.3 is a depiction of a proposed relationship between H^+ATP*ase* driven water transport and glucose metabolism. The fermentation of glucose leads to the production of excess protons, which necessitates an increase in the activity of the H^+ATP*ase* to pump protons out of the cytosol. In low glucose conditions when the cell is undergoing exclusively oxidative phosphorylation, the H+ATPase is inactive.[23] It is hypothesized that cells undergoing fermentation will exhibit faster rates of active water exchange than those undergoing primarily oxidative phosphorylation due to the role of the H^+ATP*ase* in maintaining the pH of the cytosol.

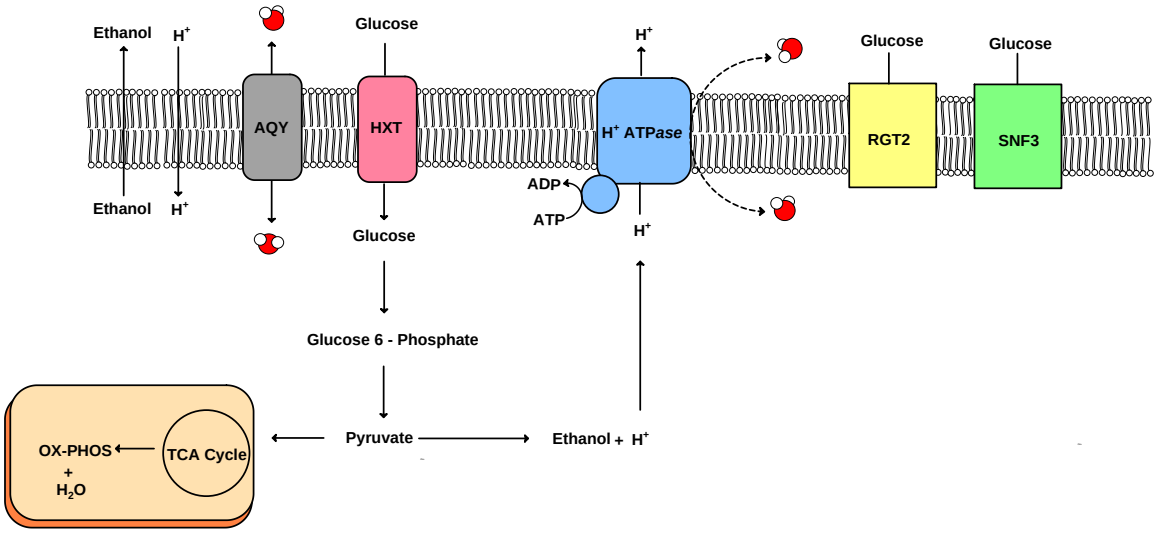

Figure 4.3 The primary roles of the H^+ATP*ase* coded by the gene *pma1* are to mediate the pH of the cytosol and to maintain the proton gradient across the membranes. The fermentation of glucose leads to acidification of the cytosol. H^+ATP*ase* is known to contribute to active k_{io}.

4.2 Materials and Methods:

Strains:

FY4 [MATa], - A gift from Professor Dunham

Fleischmann's Active Dry Baker's Yeast, [unknown ploidy] - locally purchased

BY4743 [MATa/α his3Δ1/his3Δ1 leu2Δ0/leu2Δ0 LYS2/lys2Δ0 met15Δ0/MET15 ura3Δ0/ura3Δ0] - purchased from EUROSCARF

BY4743 **(*Δpma1*)** [MATa/MATα; ura3Δ0/ura3Δ0; leu2Δ0/leu2Δ0; his3Δ1/his3Δ1; met15Δ0/MET15; LYS2/lys2Δ0; YGL008c/YGL008c::kanMX4] - purchased from EUROSCARF

BY4742 **(*Δsnf3*)** [MATα; ura3Δ0; leu2Δ0; his3Δ1; lys2Δ0; YDL194w::kanMX4] - purchased from EUROSCARF

BY4742 **(*Δrgt2*)** [MATα; ura3Δ0; leu2Δ0; his3Δ1; lys2Δ0; YDL138w::kanMX4] - purchased from EUROSCARF

Table 4.1 Knockout strains used in this study. The descriptions of these genes were taken from the *Saccharomyces Gene Database* (SGD).[24]

Gene	Systematic Name	Function
pma1	YGL008C	Plasma membrane P2-type H^+-ATPase; pumps protons out of cell; major regulator of cytoplasmic pH and plasma membrane potential
snf3	YDL194W	Plasma membrane low glucose sensor, regulates glucose transport; high affinity sensor that contains 12 predicted transmembrane segments and a long C-terminal tail required for induction of hexose transporters
rgt2	YDL138W	Plasma membrane high glucose sensor that regulates glucose transport; low affinity sensor that contains 12 predicted transmembrane segments and a long C-terminal tail required for hexose transporter induction

Media

Complete minimal media was used for both preculture and chemostat cultivation. The recipe, obtained from *Yeast Protocols,* contains L-tryptophan (20 mgL^{-1}), L-histidine-HCl (20 mgL^{-1}), L-arginine-HCl (20 mgL^{-1}), L-methionine-HCl (20 mgL^{-1}) , L-leucine (30 mgL^{-1}), L-isoleucine (30 mgL^{-1}), L-lysine-HCL (30 mgL^{-1}), L-tyrosine (30 mgL^{-1}), L-phenylalanine (50 mgL^{-1}), L-valine (150 mgL^{-1}), -serine (400 mgL^{-1}), L-threonine (200 mgL^{-1}), L-glutamic acid (100 mgL^{-1}), L-aspartic acid (100 mgL^{-1}), uracil (20 mgL^{-1}), adenine sulfate (20 mgL^{-1}). The media is also supplemented with 6.7 g yeast nitrogen base (with ammonium sulfate and without amino acids, purchased from BD diagnostics) and glucose (1 mgL^{-1} for the respiring cultures and 7.5 mgL^{-1} for the fermenting cultures).

Chemostat cultivation

Chemostats were built in-house using designs from *The Chemostat Manual* as a reference.[9] Two chemostats cultures were run in parallel, with either 0.1% glucose or 0.75% glucose to afford two distinct metabolic conditions. Chemostats had a total volume of 120 mL and a set culture volume of 70 mL. The chemostats were aerated and vigorously mixed using sterile breathing air (Airgas). Precultures of cells were grown overnight before their addition to fresh media within the chemostat. The culture was allowed to grow for at least 24 hours at 30 ℃ under air flow before dilution. The dilution rate was constant in all conditions and set to 0.256 hr^{-1}. Steady-state growth was typically achieved within 10

volume changes, and was confirmed using OD_{600}. Cell density was measured with microscopy and a Neubauer improved hemocytometer.

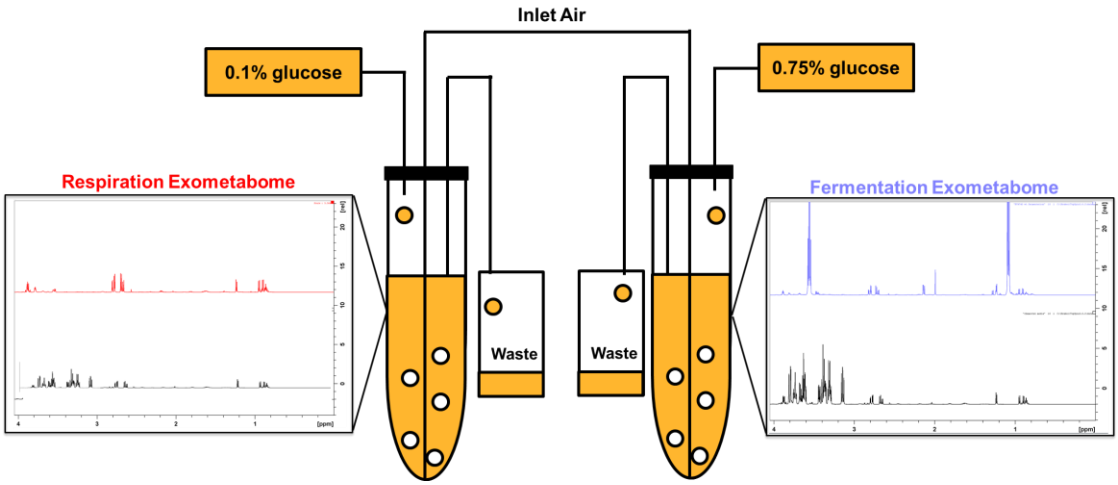

Figure 4.4 Yeast cultures in chemostats respond to the extracellular glucose concentration by adapting the mechanism of glucose metabolism. The change in metabolism can be easily seen in the NMR spectra for the exometabolome.

Exo-metabolome measurements

The exo-metabolome of each culture was measured using a Bruker Avance III 600 MHz NMR spectrometer. 1 mL of steady-state culture was collected from the discharge port and centrifuged using Eppendorf Minispin centrifuge (10,000 rpm, 3 min). The supernatant was diluted 1:1 (*v:v*) with a solution of D_2O containing an internal standard (standard : succinic acid, [3mM]). The metabolites were quantified using a water-suppression pulse

sequence. Each measurement consisted of 512 scans, a relaxation delay time of 8 seconds and an acquisition time of 5 seconds.

Flow cytometry measurements

Samples were fixed using 4% paraformaldehyde in phosphate buffered saline (PBS) and stored at -80ºC. Forward light scatter (FSC) measurements were collected for each fixed sample using flow cytometry. The mean FSC from each sample histogram was compared to a standard curve and the average diameter of cells was approximated in both the stationary and exponential growth phases. The surface area and volume of the yeast was geometrically approximated as a sphere.

Water exchange sample preparation and relaxation measurement

For each water exchange measurement, three 25 mL aliquots were collected from the efflux port and centrifuged at 900 g for one minute. The supernatant was removed and combined with the gadolinium-based contrast (GBCA), Prohance (gadoteridol, Bracco Imaging), to make a 10 mM Gd^{3+} solution. Each cell sample was washed three times with the doped supernatant and transferred to a heavy walled NMR tube. The samples were then pelleted into heavy walled NMR tubes (Wilmad 535PP) using a centrifuge at 900 g for two minutes. The total pellet preparation time was 8 minutes. The longitudinal relaxation rate constants ($R_1 = 1/T_1$) were measured using an inversion recovery pulse sequence in a Bruker Avance III 600 MHz spectrometer, equipped with a temperature controlled TXI probe set to 25 °C. Samples were allowed to acclimatize for four minutes while the 90° pulse length and power

were calibrated. A 90° pulse calibration was performed before each measurement by collecting a nutation spectrum and calculating the 90° pulse length from the 360° pulse. The 90° pulse length ranged from 9.5 – 10.5 μs. An inversion recovery pulse sequence (180° – τ – 90°) was used to measure the longitudinal relaxation rate constant. Each longitudinal relaxation measurement consisted of four scans and 32 points with a variable delay (τ) ranging from 1 ms to 3 s. The relaxation delay was 3.5 s. The total measurement time was 10 minutes.

2SX fitting parameters

The fitted 2SX parameters were the intracellular water mol fraction (p_i), the relaxivity of the contrast agent (r_1) and the transmembrane water exchange rate constant (k_{io}). The other 2SX parameters were held constant to the following values. The values for the intrinsic intracellular water exchange rate constant were set to, R_{1i} was 1.1 s^{-1}, the extracellular contrast agent concentration, [RR] was fixed at 10 mM, and the relaxation rate of the contrast free extracellular water, R_{1eo} was fixed at 0.3 s^{-1}.

2, 4, Dinitrophenol exposure

Samples of the three wild type strains were collected from steady state cultures in the fermentation and respiration regime and exposed to increasing concentrations of the protonophore, 2,4 dinitrophenol (2,4 DNP). Samples were exposed to 2,4 DNP for 15 mins before inversion recovery measurements were taken. Each measurement was conducted in biological triplicate.

4.3 Results

Establishing two metabolic regimes

Three wild type and three knockout strains were cultivated in both 0.1% glucose and 0.75% glucose at a dilution rate of 0.256 hr^{-1}. The difference in glucose concentration greatly altered the metabolic profile of each culture (Tables 4.2-4.3 and Figs 4.5-4.6).

The two metabolic conditions produced by these chemostats represent either side of a critical glucose concentration which induces the Crabtree effect. This critical point represents a significant change to mechanisms of glucose metabolism. In both conditions, the entire quantity of glucose available in the media is consumed by the culture. It is clear that aerobic fermentation allows for the cells to metabolize glucose more rapidly. The switch to aerobic fermentation also allows the culture to sustain a greater culture density. This clearly demonstrates the advantage that the Crabtree effect confers to yeast cells. The relative efficiency of fermentation versus complete respiration can easily be seen by comparing the number of cells created per gram of glucose consumed. There are two additional consequences for the switch to a fermentation heavy metabolism, which are the production of ethanol and a drop in pH, each have been quantified in Tables 4.2 and 4.3.

Table 4.2 Profiles of chemostat cultures fed 0.75% glucose

Yeast Strain	glucose uptake (fmol cell^{-1} s^{-1})	EtOH production (fmol cell^{-1} s^{-1})	cell density (10^7 cell mL^{-1})	pH
Fleischmann's	5.43	6.01	12.7	3.2
FY4	3.90	4.55	17.8	3.6
BY4743	3.99	4.93	17.3	3.2
Δpma1	3.49	4.47	19.8	3.3
Δsnf3	3.12	1.32	21.6	3.2
Δrgt2	3.65	4.14	19.0	3.2

Table 4.3 Profiles of chemostat cultures fed 0.1% glucose

Yeast strain	glucose uptake (fmol cell^{-1} s^{-1})	cell density (10^7 cell mL^{-1})	pH
Fleischmann's	0.86	10.8	4.9
FY4	0.99	9.3	6.0
BY4743	0.94	9.8	4.6
Δpma1	0.83	11.2	4.8
Δsnf3	0.70	13.2	5.3
Δrgt2	1.04	8.9	4.7

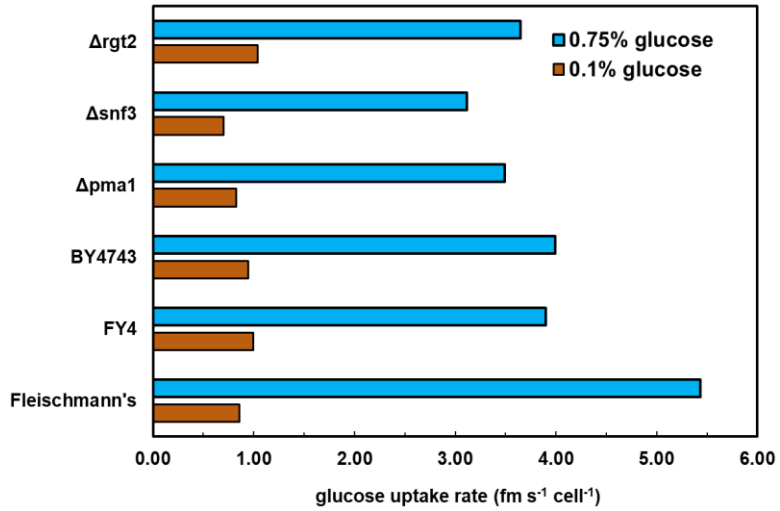

Figure 4.5 The glucose uptake rates of each strain grown in 0.75% glucose (*m:v*, blue) and 0.1% glucose (*m:v*, red)

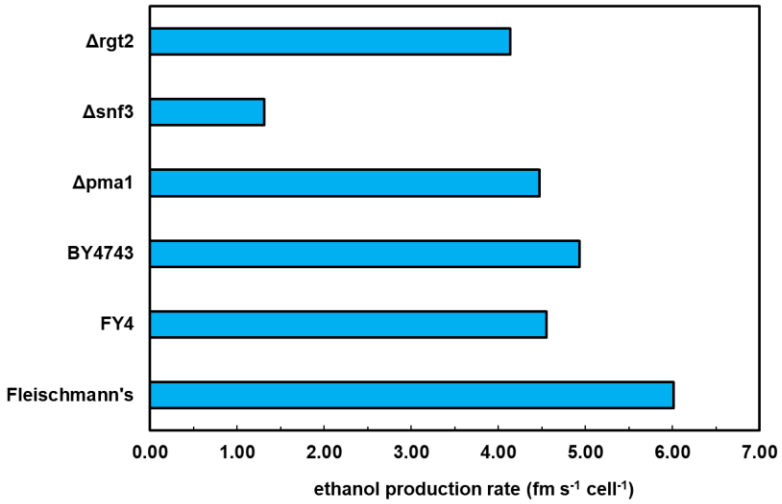

Figure 4.6 The ethanol production rates of yeast strains grown in 0.75% glucose (*m:v*).

Measuring k_{io} in two metabolic regimes

Fig. 4.7 depicts the measurements of k_{io} observed in the two metabolic conditions. Interestingly, in all strains measured, k_{io} was observed to be lower for cultures grown in 0.75% glucose than for cultures grown in 0.1% glucose. The difference between k_{io} in the respiring and fermenting cultures varied between strains, however in all cases a statistically significant difference was observed. A comparison between the k_{io} values measured for the wild type BY4743 and the subsequent knockouts reveals a few notable differences. The heterozygous knockout of *pma1* decreased k_{io} for cultures grown in 0.75% glucose, however, values of k_{io} for *pma1* knockout cells grown in 0.1% glucose were not statistically different from the wild type BY4743 values. When comparing knockouts for the genes encoding two glucose sensors, *snf3* and *rgt2*, the knockout of *snf3* carried more obvious consequences, both in terms of metabolic profile and water exchange. While the values of k_{io} observed for 0.1% glucose cultures were similar between the two glucose sensor knockouts, knocking out *snf3* decreased k_{io} for cultures grown in 0.75% glucose in comparison to the k_{io} values of *rgt2* knockout grown in the same conditions.

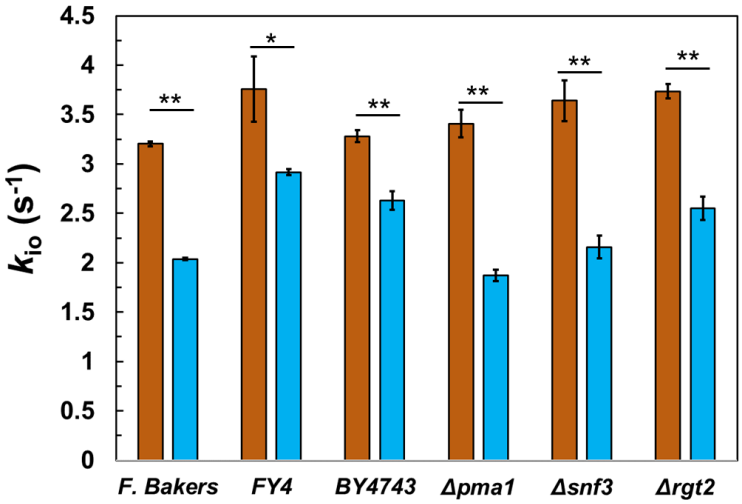

Figure 4.7 The rate constant for water efflux, k_{io}, of yeast strains grown in fermentation (blue) and respiration (red) conditions (0.75% and 0.1% *m:v* glucose, respectively). Each data point represents the average of three measurements and error bars indicate one standard deviation above and below the mean. Asterisks indicate statistically significant differences between the two conditions. (P (T<=t) two-tail, * P ≤ 0.05, **P ≤ 0.01)

Approximating cell size using flow cytometry

The average diameter of a cell was approximated by first measuring histograms of forward light scatter intensity (FSC, shown in Fig. 4.8). Mean FSC values of BY4743 and the subsequent knockouts were calculated from these histograms (Fig. 4.9) and compared to a standard curve prepared with polystyrene beads of known sizes to yield an approximate cell diameter (Tables 4.4 and 4.5). Correlation with FSC of polystyrene beads should not be taken as absolute quantification of cell size; however, the relative changes observed in these experiments were considered appropriate to compare because they occur in the same cell type and therefore are assumed to have similar indices of refraction.

In general, the average cell in the respiring cultures was typically smaller than the average cell in fermenting cultures. The only exception was the FY4 strain, which featured two populations in the histogram and likely indicated that cells flocculated in low glucose conditions (an assumption supported by microscopy). Fermenting cells are larger on average than the respiring cells, which indicates a smaller SA/V ratio.

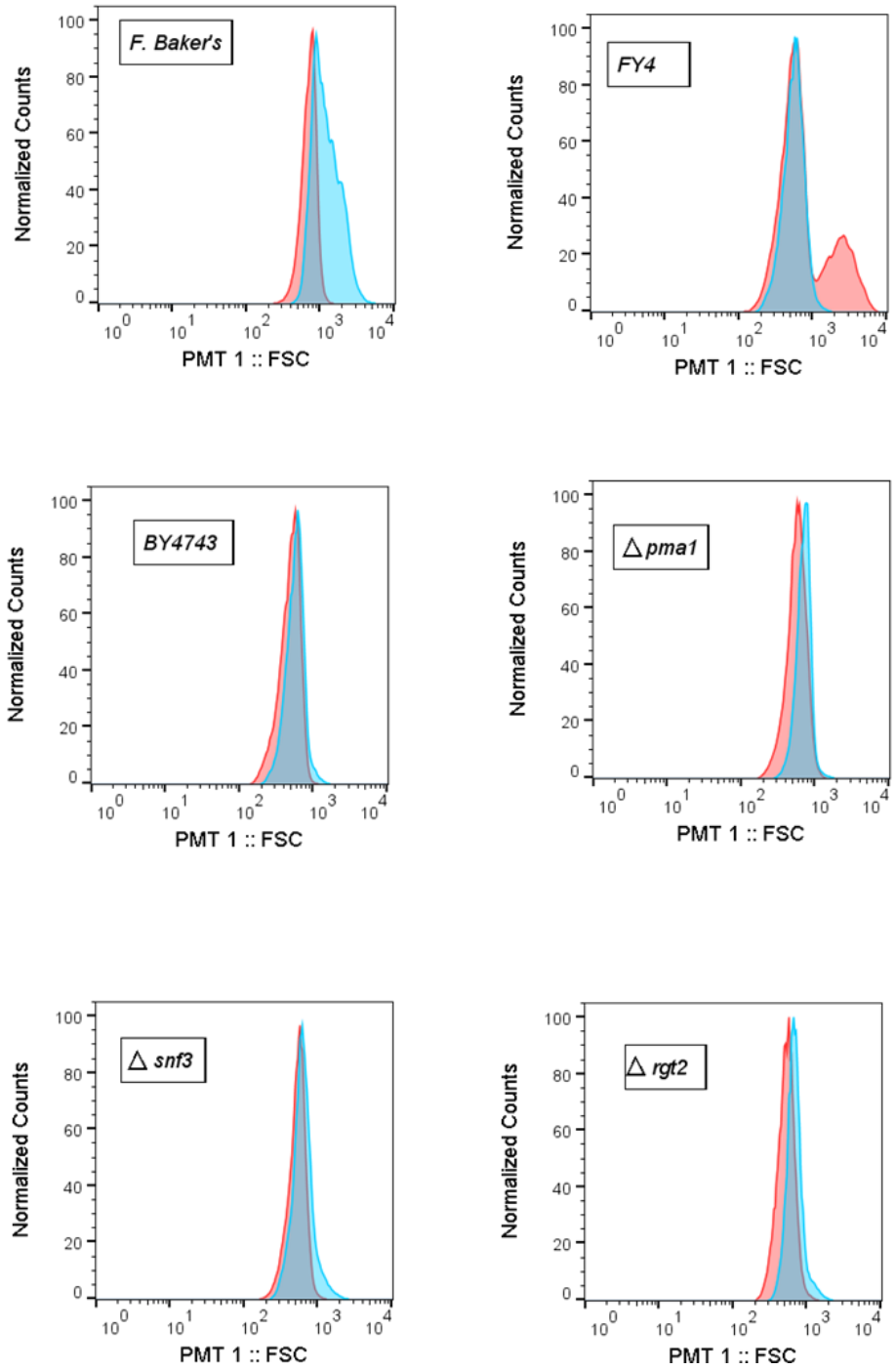

Figure. 4.8 Forward light scatter histograms of yeast cells of each strain grown in fermentation (blue) and respiration (red) conditions (0.75% and 0.1% *m:v* glucose, respectively). The histogram are made up of over 10,000 counts.

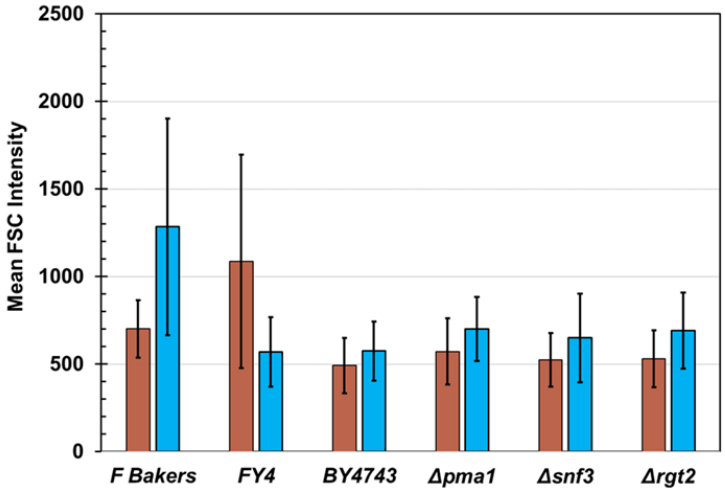

Figure 4.9 Forward light scatter intensity (FSC) of yeast cells of each strain grown in fermentation (blue) and respiration (red) conditions (0.75% and 0.1% *m:v* glucose, respectively). Error bars indicate one standard deviation above and below the mean.

Table 4.4 Average cell size estimates for the cultures grown in 0.75% glucose.

Yeast strain	Diameter (μm)	Volume (μm^3)	Surface Area (μm^2)	SA/V	k_{io} (s^{-1})
BY4743	2.62	9.41	21.56	2.29	2.71
Δrgt2	3.15	16.41	31.22	1.90	2.55
Δpma1	3.19	16.98	31.95	1.88	1.87
Δsnf3	2.96	13.53	27.46	2.03	2.16

Table 4.5 Average cell size estimates for the cultures grown in 0.1% glucose

Yeast strain	Diameter (μm)	Volume (μm^3)	Surface Area (μm^2)	SA/V	k_{io} (s^{-1})
BY4743	2.25	5.93	15.86	2.67	3.28
Δrgt2	2.42	7.42	18.40	2.48	3.75
Δpma1	2.61	9.32	21.43	2.30	3.41
Δsnf3	2.40	7.21	18.05	2.50	3.66

Passive k_{io}

There is a moderate degree of positive correlation ($R^2 = 0.72$) between surface area to volume ratio and the observed k_{io} which suggests that changes in cell size contributes to the changes in k_{io} observed (Fig. 4.10).

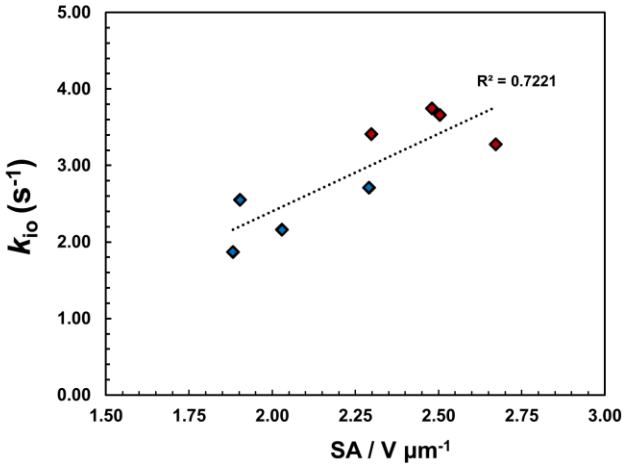

Figure 4.10 There is a degree of positive coorelation between the SA/V ratio and k_{io} observed in the strains featured in Table 4.3. The red diamonds are the respiring cultures and the blue diamonds are the fermenting cultures

Quantifying the changes to active k_{io}

The percent difference (ΔR/F) between respiring (R) and fermenting (F) conditions was calculated using Eqns. 4.4 and 4.5.

$$\Delta R/F = \frac{|(R)k_{io} - (F)k_{io}|}{0.5[(R)k_{io} + (F)k_{io}]} \quad \textbf{(4.4)}$$

$$\Delta R/F = \frac{|(R)\frac{SA}{V} - (F)\frac{SA}{V}|}{0.5\left[(R)\frac{SA}{V} + (F)\frac{SA}{V}\right]} \quad \textbf{(4.5)}$$

The percent difference between SA/V and k_{io} observed when comparing the cultures grown in 0.1% glucose (R) to the cultures grown in 0.75% glucose (F) reveals that the change in k_{io} between the two metabolic conditions cannot be adequately explained by a change in cell morphology. The *Δsnf3* and *Δpma1* strains are clear examples where active k_{io} is affected. (Fig. 4.11)

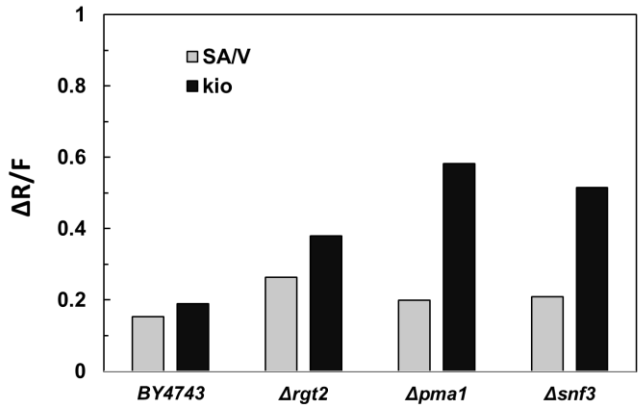

Figure 4.11 The percent difference between the respiration and fermentation condition (ΔR/F) of k_{io} and the surface area to volume ratio calculated between the respiration and fermentation conditions of each strain.

The effects of 2,4, Dinitrophenol exposure

Three wildtype strains were grown to the steady state and then exposed to increasing levels of the protonophore 2,4-dinitrophenol (2,4-DNP, Fig 4.12) The addition of 2,4-DNP to the cell medium was found to decrease k_{io} for cultures grown in 0.1% glucose. 2,4-DNP did not appear to substantially affect k_{io} for cultures grown in 0.75% glucose, although a slight decrease to k_{io} may be discerned with increasing 2,4-DNP with the FY4 strain.

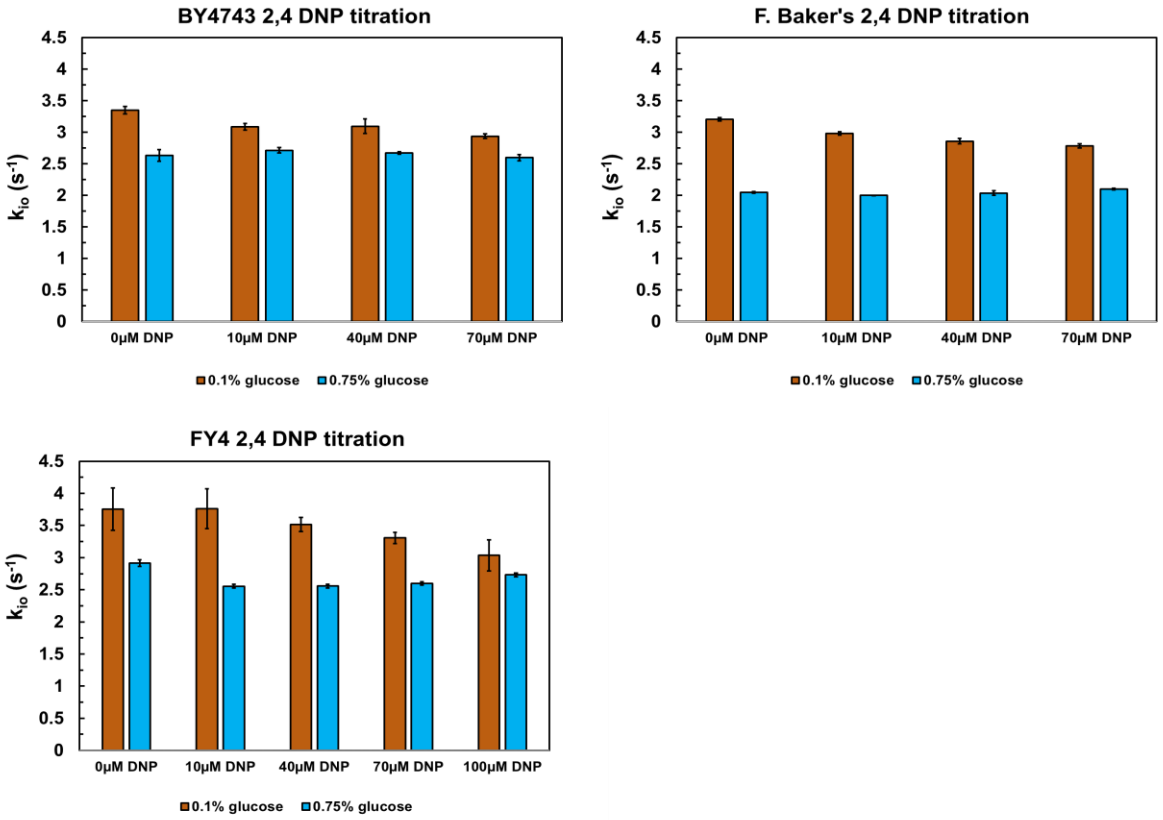

Fig 4.12 The effect of the titration of the protonophore 2,4-dinitrophenol (2,4-DNP) on k_{io} in three wild type yeast strains grown in 0.1% glucose (red) or 0.75% glucose (blue).

4.4 Discussion

H^+ATPase mediated water transport

Along with the role of producing the membrane gradient which drives many aspects of membrane transport, the H^+ATP*ase* is also tasked with the role of maintaining the pH of the cytosol. The concentration of glucose in the media fed into a chemostat greatly affects

quantity of protons produced. The extracellular pH of cultures grown in 0.75% glucose, was found to be consistently lower (pH 3.2-3.6) than that of cultures grown in 0.1% glucose (pH 4.6-6.0). This comes as no surprise, as protons are produced and expelled at a greater rate when cells are undergoing fermentation than when undergoing exclusively oxidative phosphorylation. This suggests that H^+ATP*ases* in the cells grown in 0.75% glucose operate at a higher capacity than those within cells grown in 0.1% glucose.

The values for k_{io} observed do not reflect the difference in proton production and efflux between the two conditions. In all strains, k_{io} was observed to be greater when grown in 0.1% glucose than in 0.75% glucose. The activity of the H^+ATP*ase* in yeast is proposed to be the driving force of active water exchange, however, in all strains, k_{io} was observed to be greater in conditions where the extrusion of protons was slower. This conflicts with the hypothesis that water exchange is driven by the rate of proton efflux through the H^+ATP*ase*.

To further understand the relationship between metabolic pathway and H^+ATP*ase* driven water exchange, the heterozygous knockout for *pma1* was revisited. The heterozygous knockout was grown to the steady state in both 0.1% glucose and 0.75% glucose. Consistent with the previous reports in the literature as well as our observations from Chapter 2 of this manuscript, chemostat cultures which are heterozygous for *pma1* exhibit statistically significant decreases to values of k_{io} compared to the wild type when grown in 0.75% glucose (Fig. 4.13).[3]

Remarkably, heterozygous knockouts of *pma1* grown in 0.1% glucose, exchange water at the same rate as wild type strain grown in 0.1% glucose (Fig. 4.13). This suggests that H^+ATP*ase* mediated water transport is not a significant contributor to k_{io} for cells undergoing primarily oxidative phosphorylation. This is particularly notable because water exchange occurs more rapidly in cells grown in 0.1% glucose than in cells grown in 0.75% glucose. For cells grown in 0.75% glucose, water transport is driven by the H^+ATP*ase*, however, this does not appear to be the case for cells grown in 0.1% glucose.

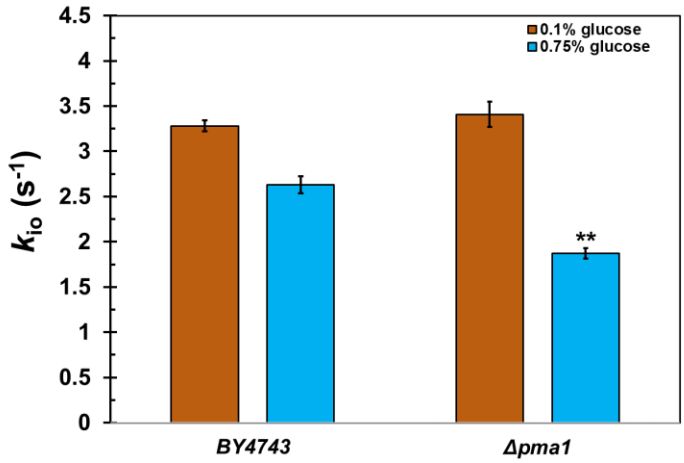

Figure 4.13. The rate constant for water efflux, k_{io}, of wild type BY4743 and knockout Δ*pma1* grown in fermentation (blue) and respiration (red) conditions (0.75% and 0.1% *m:v* glucose, respectively). Each data point represents the average of three measurements and error bars indicate one standard deviation above and below the mean. Asterisks indicate statistically significant differences between the the knockout and the wild type. (P (T<=t) two-tail, **P ≤ 0.01)

Cell size and passive k_{io}

As discussed in the introductory chapter, k_{io} is made up of both active and passive k_{io} components. Passive k_{io} is the product of the surface area to volume ratio multiplied by the passive permeability of the membrane to water (P_w). The value P_w is assumed to be constant between the metabolic regimes, and thus, passive k_{io} is assumed to be driven solely by morphology, which is represented by the SA/V ratio.

Although the general dimensions of a typical *Saccharomyces cerevisiae* cell are that of a prolate spheroid, the surface area and volume of a yeast cell are often geometrically approximated as a sphere.[25] One of the benefits of chemostat cultivation is that the cell size distribution of cells in most conditions appears to be considerably more uniform than previously observed in batch cultures. The two exceptions to this observation are the FY4 strain grown in 0.1% glucose and the F. Baker's strain grown in 0.75% glucose. The FY4 strain grown in 0.1% glucose has two populations present, while the F. Baker's strain grown in 0.75% glucose has a wide distribution. These characteristics makes the quantification of an average cell size within these cultures less accurate. The distribution of FSC in the BY4743 wild type strain and subsequent knockouts appears to be quite uniform in all conditions. From the histograms in Fig. 4.8, it is clear that the glucose concentration in the media has a slight effect on the size of an average cell within these cultures. Cells grown in 0.1% glucose are slightly smaller than cells grown in 0.75% glucose.

For the wild type BY4743 and subsequent knockout strains, using a spherical approximation of cell size results in a moderate degree of correlation between the SA/V ratio and overall k_{io} (Fig. 4.10). This implies that the passive component of k_{io} changes between the two metabolic conditions, which contributes to the changes observed in total k_{io}. Passive k_{io} is lower when cells are grown in 0.75% glucose than when they are grown in 0.1% glucose because, on average, cells grown in 0.75% glucose are slightly larger than those grown in 0.1% glucose. This change in passive exchange accounts for some of the difference observed between the overall values of k_{io} between the two metabolic conditions, however, it does not appear to account for all changes in k_{io} observed. Fig. 4.12 demonstrates two instances (*snf3* and *pma1*) where the change in SA/V ratio between cells grown in 0.1% glucose and 0.75% glucose not great enough to account for the observed differences in k_{io} observed between the two conditions.

Glucose uptake mechanisms and k_{io}

To further understand the relationship between glucose metabolism and k_{io}, knockouts for glucose sensors, *snf3* and *rgt2,* were grown in 0.1% and 0.75% glucose. Values for k_{io} appeared to be similar in the 0.1% glucose fed cultures of *rgt2* and *snf3*. The knockout of *snf3*, however, caused substantial changes to the culture grown in 0.75% glucose. When grown in 0.75% glucose, strains with *snf3* knocked out exhibit slower rates of water exchange than the *rgt2* knockout grown in 0.75% glucose. This values for k_{io} are nearly as slow as those observed upon the heterozygous knockout of *pma1* for cultures grown in 0.75% glucose. This is quite significant, because *snf3* is not directly responsible for any

membrane transport. The downstream effects of these signaling proteins likely ties the glucose sensors to k_{io}, however, this connection only appears to be present when the cell is undergoing fermentation. These signalling proteins affect the expression of HXT transporters, and also have an effect on the cells metabolic state, which is clearly seen in the low production of ethanol observed in the *snf3* knockout mutant grown in 0.75% glucose. These results demonstrate indirect effects on water exchange and another instance where the internal pathway of glucose metabolism appears to alter the effects of a knockout on k_{io}.

Possible role of the mitochondria

The measurements of the *snf3* and *pma1* knockout indicate that the pathway of glucose metabolism appears to affect the mechanism by which water is exchanged across the membrane. These results beg the question, what drives active component of k_{io} for cells grown in 0.1% glucose, if not for the H^+ATP*ase*? Although most of the attention paid to water exchange has been rightly focused on transport proteins located in the cell membrane, the activity of the intracellular organelles, such as the mitochondria may contribute indirectly to active k_{io}. 2,4 dinitrophenol (2,4-DNP) is a protonophore that is known to disrupt the proton gradient between the mitochondrial matrix and the inner membrane space.[26,27] For cultures grown in 0.1% glucose, k_{io} was observed to decrease as the concentration of 2,4 DNP increased. Cultures grown in 0.75% glucose, with the exception of FY4, k_{io} appeared to be unaffected by exposure to 2,4-DNP (Fig. 4.11).

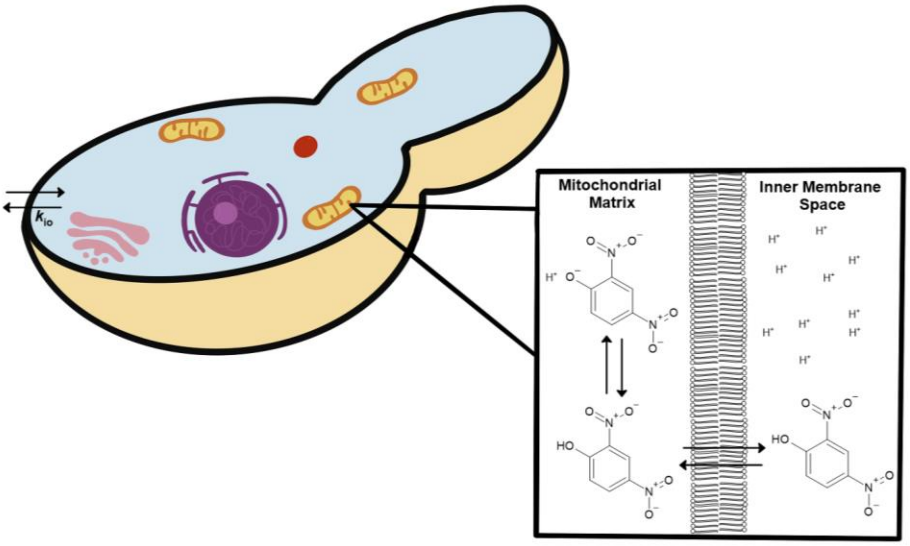

Figure 4.14 The protonophore 2,4 dinitrophenol (2,4-DNP) can affect the mitochondrial proton gradient by ferrying protons from the inner membrane space into the mitochondrial matrix. This disrupts the cells ability to produce ATP.

Once again, the titration of 2,4-DNP presents another example where water exchange mechanisms of cultures grown in 0.1% glucose appear to operate in a different way than cultures grown in 0.75% glucose. The exact relationship between 2,4-DNP exposure and water exchange across the cell membrane remains unclear. Water exchange rates of cells grown in 0.1% glucose may be altered after exposure to 2,4-DNP as a consequence of the change in ATP availability, or perhaps as a result of the disruption of the mitochondrial proton gradient itself. It should be noted that although the yeast ferment over half of the glucose taken up, there is still a considerable amount of glucose available leftover to undergo respiration within cultures grown in 0.75% glucose. In fact, there is likely more glucose available after fermentation in the 0.75% cultures than the 0.1% cultures began

with originally. This suggests that the response to 2,4-DNP may not be simply due to differences in the amount of glucose processed by the mitochondria for cultures grown in 0.75% glucose and 0.1% glucose. There may be an advantage to elevated k_{io} values conferred to the cell when undergoing exclusively oxidative phosphorylation that may be of less importance when the cell is undergoing fermentation.

H_2O production in the mitochondria

It is also worth considering the possible contribution from the water produced by glucose metabolism as a possible contributor to k_{io}. O_2 is the final electron acceptor in the electron transport chain, which results in the formation of water. Although the exact stoichiometry is the subject of some debate, the complete oxidation of one molecule glucose is thought to produce somewhere between 40 and 60 molecules of water within the cell.[28] Assuming that all non-fermented glucose is turned into 60 water molecules water, the BY4743 wild type cells produce water at a rate of 1.65 fL cell^{-1} s^{-1} when grown in 0.75% glucose and 1.01 fL cell^{-1} s^{-1} when grown in 0.1% glucose. The total water efflux of these cells can be found by the product of k_{io} (which represents the number of times the internal volume changes with external volume per second) and the cell volume. This calculation results in an efflux of 25.5 fL cell^{-1} s^{-1} for cultures grown in 0.75% glucose and 19.5 fL cell^{-1} s^{-1} for cultures grown in 0.1% glucose. An upper-level estimate of the water generated from the complete oxidation of glucose can account for up to 6.5% of the total water exchanging across the membrane. Interestingly, although the rate constant for water efflux is greater in the respiration cells, the total sum of water efflux per second per cell is greater in the

fermenting wild type cell because it is larger on average than a respiring cell. At this moment, it unclear if the total water efflux calculation offers any additional insight into the cell, however it may prove to be an important distinction moving forward.

4.5 Conclusions

The relationship between active k_{io} and metabolism appears to be significantly more nuanced than a direct relationship to H^+ATP*ase* turnover. The contribution of the H^+ATP*ase* to k_{io} is dependent on the concentration of extracellular glucose. The internal metabolic pathway utilized by cells appears to alter the mechanism of water efflux. When glucose is plentiful and the cells are fermenting glucose into ethanol, the H^+ATP*ase* contributes to water exchange, however, when extracellular glucose levels are low, the cell undergoes exclusively oxidative phosphorylation and water exchange is unaffected by the heterozygous mutation of the gene encoding for the H^+ATP*ase*, *pma1*.

The mitochondrial gradient appears to affect k_{io} to a greater extent for cells grown in 0.1% glucose in comparison to cells grown in 0.75% glucose. It is unclear what advantage, if any, an increase in k_{io} may confer the cells grown in 0.1% glucose. When considering the potential role of k_{io} as a diagnostic biomarker, the metabolic differences between cells may affect the mechanism of water exchange. Although these findings represent an increase in the complexity of the interpretation of k_{io}, they also demonstrate that k_{io} is potentially capable of reporting changes to metabolic pathway.

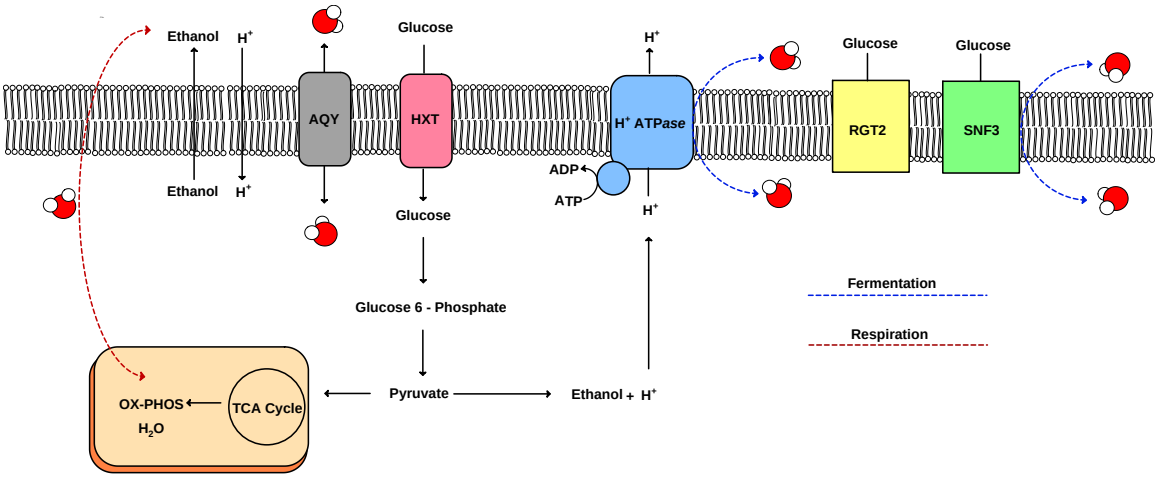

Figure 4.15 There are a number of mechanisms that contribute to active k_{io}. These mechanisms appear to change depending on the metabolic condition. The heterozygous deletion of *pma1* leads to a decrease in k_{io} when the cell is fermenting, but when the cell is undergoing exclusively oxidative phosphorylation, no change is observed. The deletion of the *snf3* gene appears to affect water transport through the H^+ATP*ase* indirectly, potentially by altering glucose uptake and ethanol production rates. Disruption of the proton gradient across the mitochondrial inner membrane appears to affect k_{io} independently from the H^+ATP*ase*, however, the disruption of the membrane does not appear to affect k_{io} when the cell is undergoing fermentation.

4.6 References

1. Bisson, L. F., Fan, Q. & Walker, G. A. Sugar and Glycerol Transport in Saccharomyces cerevisiae. Adv. Exp. Med. Biol. 892, 125–168 (2016).

2. Serrano, R., Kielland-Brandt, M. C. & Fink, G. R. Yeast plasma membrane ATPase is essential for growth and has homology with (Na + + K +), K + - and Ca 2+ - ATPases. Nature 319, 689–693 (1986).

3. Zhang, Y., Poirier-Quinot, M., Springer, C. S. & Balschi, J. A. Active Trans-Plasma Membrane Water Cycling in Yeast Is Revealed by NMR. Biophys. J. 101, 2833–2842 (2011).

4. Springer, C. S. Using 1H2O MR to measure and map sodium pump activity in vivo. J. Magn. Reson. San Diego Calif 1997 291, 110–126 (2018).

5. Novick, A. & Szilard, L. Description of the Chemostat. Science 112, 715–716 (1950).

6. Monod, J. Technique, Theory and Applications of Continuous Culture. Ann Inst Pasteur 79, 390–410 (1950).

7. Kjeldgaard, N. O., Maaloe, O. & Schaechter, M. The transition between different physiological states during balanced growth of Salmonella typhimurium. J. Gen. Microbiol. 19, 607–616 (1958).

8. Control of macromolecular synthesis - CERN Document Server. https://cds.cern.ch/record/263420.

9. Miller, A. W., Befort, C., Kerr, E. O. & Dunham, M. J. Design and Use of Multiplexed Chemostat Arrays. J. Vis. Exp. JoVE (2013) doi:10.3791/50262.

10. Weusthuis, R. A., Pronk, J. T., van den Broek, P. J. & van Dijken, J. P. Chemostat cultivation as a tool for studies on sugar transport in yeasts. Microbiol. Rev. 58, 616–630 (1994).

11. Postma, E., Verduyn, C., Scheffers, W. A. & Van Dijken, J. P. Enzymic analysis of the Crabtree effect in glucose-limited chemostat cultures of Saccharomyces cerevisiae. Appl. Environ. Microbiol. 55, 468–477 (1989).

12. Bell, G. I. et al. Molecular Biology of Mammalian Glucose Transporters. Diabetes Care 13, 198–208 (1990).

13. Maier, A., Völker, B., Boles, E. & Fuhrmann, G. F. Characterisation of glucose transport in Saccharomyces cerevisiae with plasma membrane vesicles (countertransport) and intact cells (initial uptake) with single Hxt1, Hxt2, Hxt3, Hxt4, Hxt6, Hxt7 or Gal2 transporters. FEMS Yeast Res. 2, 539–550 (2002).

14. Choi, K.-M., Kwon, Y.-Y. & Lee, C.-K. Disruption of Snf3/Rgt2 glucose sensors decreases lifespan and caloric restriction effectiveness through Mth1/Std1 by adjusting mitochondrial efficiency in yeast. FEBS Lett. 589, 349–357 (2015).

15. Ng, T. S. et al. SNF3 as High Affinity Glucose Sensor and Its Function in Supporting the Viability of Candida glabrata under Glucose-Limited Environment. Front. Microbiol. 6, (2015).

16. Ozcan, S., Dover, J. & Johnston, M. Glucose sensing and signaling by two glucose receptors in the yeast Saccharomyces cerevisiae. EMBO J. 17, 2566–2573 (1998).

17. Ozcan, S. & Johnston, M. Three different regulatory mechanisms enable yeast hexose transporter (HXT) genes to be induced by different levels of glucose. Mol. Cell. Biol. 15, 1564–1572 (1995).

18. Lafuente, M. J., Gancedo, C., Jauniaux, J.-C. & Gancedo, J. M. Mth1 receives the signal given by the glucose sensors Snf3 and Rgt2 in Saccharomyces cerevisiae‡. Mol. Microbiol. 35, 161–172 (2000).

19. Std1 and Mth1 Proteins Interact with the Glucose Sensors To Control Glucose-Regulated Gene Expression in Saccharomyces cerevisiae. https://www.ncbi.nlm.nih.gov/pmc/articles/PMC84254/.

20. Jordan, P., Choe, J.-Y., Boles, E. & Oreb, M. Hxt13, Hxt15, Hxt16 and Hxt17 from Saccharomyces cerevisiae represent a novel type of polyol transporters. Sci. Rep. 6, 23502 (2016).

21. Rao, R., Drummond-Barbosa, D. & Slayman, C. W. Transcriptional regulation by glucose of the yeast PMA1 gene encoding the plasma membrane H+-ATPase. Yeast 9, 1075–1084 (1993).

22. Serrano, R. In vivo glucose activation of the yeast plasma membrane ATPase. FEBS Lett. 156, 11–14 (1983).

23. Isom, D. G. et al. Coordinated regulation of intracellular pH by two glucose-sensing pathways in yeast. J. Biol. Chem. 293, 2318–2329 (2018).

24. Saccharomyces Genome Database | SGD. https://www.yeastgenome.org/.

25. Zakhartsev, M. & Reuss, M. Cell size and morphological properties of yeast Saccharomyces cerevisiae in relation to growth temperature. FEMS Yeast Res. 18, (2018).

26. Uncoupling reagents and metabolism. 2. Effects of 2:4-dinitrophenol and salicylate on glucose metabolism in baker's yeast. https://www.ncbi.nlm.nih.gov/pmc/articles/PMC1204837/.

27. Field, J., Martin, A. W. & Field, S. M. The effect of 2-4 dinitrophenol on the oxygen consumption of yeast. J. Cell. Comp. Physiol. 4, 405–420 (1934).

28. Horiike, K., Ishida, T. & Miura, R. How many water molecules produce during the complete oxidation of glucose? Reply to Robert A Mitchell. Biochem. Educ. 24, 208–209 (1996).

CHAPTER 5. CONCLUSION

This thesis serves primarily as an investigation into how the dynamics of growth and metabolism can affect steady-state transmembrane water exchange rate constants in the model organism, *S. cerevisiae*. The goal of this thesis is to understand how biological processes may affect membrane water exchange and consequently, how membrane water exchange may affect how we perceive MRI contrast agents. There are a number of advantages to carrying out these experiments in yeast cells, including the ease of growth, the reproducibility of metabolic states, the homogeneity of chemostat cultures and the availability of gene knockouts. These experimental advantages however, come at a significant price. Translational studies from single cells to humans should always be met with a healthy level of skepticism. Perhaps the main finding of this work shows that even in a simple, single celled model organism, there appears to be a great deal of nuance into how the cell regulates water exchange. It is an appreciation of this nuance that we hope is considered moving forward. In this concluding chapter, we will highlight a number of results from the experiments of this work and attempt to contextualize them within the greater framework of diagnostic imaging.

Active and passive k_{io}

As discussed in the introduction, the measurement k_{io} is an intrinsic cellular property made up of both passive and energetically driven components. Imaging k_{io} presents an unusual opportunity as a biomarker because rate constants are so rarely quantifiable *in vivo*. Active

k_{io}, has been proposed as a probe for "metabolic imaging" because it describes the kinetics of a cellular function.

One of the difficulties of interpreting changes to k_{io} in a multicellular organism is the dissection of active and passive k_{io}. Does a change in k_{io} arise due to a change in cell size, or due to a change in the active exchange processes? In this work, forward light scatter (FSC) was measured with flow cytometry to serve as a proxy for average cell diameter. A spherical approximation was used to estimate cell surface area and volume of a cell. Despite the potential shortcomings of this methodology, the same level of dimensional analysis is rarely afforded in a diagnostic setting, as even a biopsy would likely be far less representative of a region of interest than the cells sampled from culture. *In vivo*, it is undoubtedly far more difficult to break down changes to k_{io} in terms of active and passive processes.

Cellular morphology can be an important consideration in diagnostics. Given the relationship between k_{io} and SA/V, one could imagine that k_{io} maps for a region of interest which might supplement procedures such as a biopsy. It is clear, however, that the k_{io} is not consistently a reflection of cell size. In the batch culture experiments presented in Chapter 2, we saw little correlation between SA/V and $k_{io,}$ however, the chemostat culture experiments presented in Chapter 4, we saw a moderate degree of positive correlation between SA/V and k_{io}. This indicates that k_{io} better reflects cell size in chemostat cultures than in batch cultures, but perhaps more importantly, it also indicates that the relationship between SA/V and k_{io} can be unpredictable.

On the mechanisms of steady-state water exchange

Our initial hypothesis proposed that, since water is co-transported with many membrane processes, k_{io} values may reflect the amount of material crossing the membrane. It is clear from the experiments of Chapters 2 and 4 that this hypothesis is inadequate. In batch cultures of the laboratory yeast strain BY4742 and BY4743, we observed that water exchange was similar for the exponential phase and for the stationary phase despite a significant difference in the amount of nutrients taken up. Similarly, chemostat cultures grown in 0.75% glucose exhibit far more rapid glucose uptake than cells grown in 0.1% glucose despite taking up more glucose and ejecting more H^+ and ethanol.

The Active Water Cycling (AWC) hypothesis proposes that water exchange can be used as a proxy for membrane ATP*ase* activity. In yeast, H^+ATP*ase* operates as the primary contributor to the membrane gradient and thus, it is hypothesized to be the primary contributor to active k_{io}. In Chapter 2, a knockout of *pma1* exhibited the largest depression to k_{io} was sole instance where k_{io} was decreased across the entire growth curve. This observation appears to support the AWC hypothesis. The experiments of Chapter 4 serve to complicate matters. In Chapter 4, we identified a metabolic scenario in low glucose chemostat cultures where the H^+ATP*ase* does not appear to be the primary driver of water exchange. The heterozygous expression of *pma1* does not alter the observed values of k_{io} for cultures undergoing primarily oxidative phosphorylation. This suggests that the H^+ATP*ase* may only drive water exchange in specific metabolic scenarios.

The experiments of Chapters 2 and 4 suggest that there are multiple mechanisms driving active k_{io} and that these mechanisms may alter their contribution to k_{io} depending on the

state of the cell. Water exchange increases due the activity of membrane bound pumps, like H^+ATP*ase* activity; however, in addition to (or some cases in the absence of) ATP*ase* activity, there are other independent processes that can affect active k_{io}.

Moving forward with k_{io} imaging :

As a potential biomarker for imaging, k_{io} occupies a space of its own. We know now that k_{io} is sensitive to changes within internal metabolic pathways, but values of k_{io} do not reflect the rate of substrate exchange. This is an important distinction, because it differentiates k_{io} from typical biomarkers which measure metabolic flux.

The mechanisms which contribute to water exchange should not be assumed to be shared among all cell types nor should they be considered to be consistent among a given cell type exhibiting different metabolic states. We demonstrated in this work that there are a number of potential contributors to water exchange, and that these contributors can dynamically change. This makes predicting how a particular pathology may affect the values k_{io} of tissue to be quite difficult. Values for k_{io} should therefore not be assumed to be a reporter of any particular process unless that process can be clearly shown to drive water exchange in that specific scenario. These potential pitfalls do not stop k_{io} from being informative, but they do imply that careful interpretation of k_{io} is needed to understand the diagnostic implications of a change in k_{io}.

Instead of focusing on k_{io} reporting a particular process, it may be much more valuable to consider k_{io} as an independent metric. In this sense, normal tissue has a normal k_{io} which can be compared to regions of interest that are of concern to the diagnostician. Since there are a wide number of processes which may alter k_{io} a change in these processes may be

unique to a particular pathology. It should also be considered that changes may occur to both active and passive water exchange that may effectively negate each other leading to no change to observed k_{io}. This was suspected to be the case in the BY4742 wild type strain grown in batch culture.

Accounting for k_{io} in R_1

As a final thought, in Chapter 3 we demonstrated the potentially misleading effects that a change in water exchange may have on the quantification of relaxivity of MRI contrast agents. These findings may be the most immediately relevant to diagnostic imaging because they imply that the water exchange rate should be accounted for when quantifying MRI contrast agent relaxivity. The quantification of relaxivity in cell systems with fast exchange more closely matches the inherent relaxivity of the chelate, while the quantification of relaxivity cell systems with slow membrane exchange can appear significantly lower than the inherent relaxivity of the chelate. Without an understanding of the membrane water exchange rate, these changes in observed relaxivity may be falsely attributed to the response of a contrast agents.